Cryo-electron tomography on FIB-lamellae for the structural characterization of bacterial secretion systems

Cryo–electron tomography on FIB-lamellae for the structural characterization of bacterial secretion systems

Casper Berger

Cover design: Casper Berger

Layout: Nynke van Polanen

Printing: Ridderprint | www.ridderprint.nl

ISBN: 978-94-6458-639-8

Cryo-electron tomography on FIB-lamellae for the structural characterization of bacterial secretion systems

DISSERTATION

to obtain the degree of doctor at Maastricht University,
on the authority of the Rector Magnificus,
Prof. dr. Pamela Habibović
in accordance with the decision of the Board of Deans,
to be defended in public on
Tuesday 1st of November, 2022 at 10:00 hours

by

Casper Berger

Born in Utrecht, the Netherlands, on 8th February 1987

Promotors

Prof. dr. P. J. Peters

Prof. dr. R. B. G. Ravelli

Co-promotor

dr. C. López-Iglesias

Assessment committee

Prof. dr. C.P.M. Reutelingsperger (chairman)

dr. M. Bárcena, Leiden University Medical Centre

Prof. dr. L. Moroni

Prof. dr. C. Sachse, Ernst-Ruska-Centre, Jülich, Germany

This research was part of the M4i research program received financial support from the Dutch Province of Limburg under the LINK program, the Netherlands Organisation for Scientific Research (NWO) in the framework of the National Roadmap NEMI project number 184.034.014 and by the PPP Allowance made available by Health~Holland, Top Sector Life Sciences & Health, to stimulate public-private partnerships, under project number LHSM18067.

Table of contents

Chapter 1

General introduction

1. The bacterial type III and VII secretion system

Secretion systems are macromolecular protein complexes that transport bacterial virulence factors across bacterial membranes to manipulate host cells or other bacteria (Costa *et al.*, 2015). Nine main secretion systems have been identified thus far. To transport proteins across bacterial membranes, secretion systems span across the inner or outer membrane (e.g. type V and VIII secretion systems), where substrates are transported over the inner and outer membrane in two separate steps, or they span both the inner and outer membrane (e.g. Type III, IV and VI secretion systems), allowing for transport across both membranes in a single step (Costa *et al.*, 2015; Bhoite *et al.*, 2019; Gorasia *et al.*, 2020). Secretion systems are indispensable for the pathogenesis of many bacteria, such as *Salmonella*, *Yersinia* and *Chlamydia*, which require the Type III secretion system (T3SS) (Deng *et al.*, 2017).

The T3SS is a syringe-like protein complex that spans the bacterial inner and outer membrane. It shares considerable sequence- and structural homology with the bacterial flagellum and the complexes likely have a common evolutionary ancestor (Diepold and Armitage, 2015; Rossmann and Beeby, 2018). The complex consists of a basal body spanning the inner and outer membrane, a cytosolic sorting platform involved in loading substrates for secretion, and an extracellular hollow needle. It secretes virulence factors in an unfolded state from the bacterial cytosol via the needle structure across a host membrane into the host cell (Engelenburg and Palmer, 2010; Radics *et al.*, 2014). These different effector proteins manipulate host cells in different ways including manipulation of the host cytoskeleton, modulation of the host immune system and allow escape from the phagosomal host membrane (Bliska *et al.*, 2013; Du *et al.*, 2016).

A less well characterized secretion system is the type VII secretion system (T7SS), expressed by many mycobacteria and some gram-positive bacteria (Bunduc *et al.*, 2020). It is essential for the pathogenesis of *Mycobacterium tuberculosis*, the causative agent of tuberculosis, which caused 1.4 million deaths in 2019 (World Health Organisation, 2020). There are five different known T7SSs termed ESX-1 to ESX-5. These are involved in diverse processes including transport of iron across the mycobacterial envelope (ESX-3) (Serafini *et al.*, 2013; Siegrist *et al.*, 2014), conjugation between mycobacteria (ESX-4) (Gray *et al.*, 2016) and nutrient uptake and host immune modulation (ESX-5) (Ates *et al.*, 2015; Ates, 2020). ESX-2 is poorly characterized and no clear function has been determined yet. The genes encoding for ESX-2 are located adjacent to ESX-1 in *M. tuberculosis*, but are absent in *Mycobacterium marinum* (Gröschel *et al.*, 2016; Bunduc *et al.*, 2020). ESX-1 is essential for mycobacterial pathogenesis and is required for translocation from the phagosome and mycobacterial pathogenesis (van der Wel *et al.*, 2007; Houben *et al.*, 2012) by lysing the phagosomal membrane (de Jonge *et al.*, 2007; Smith *et al.*, 2008; Conrad *et al.*, 2017). Substrates of the T7SS include ESX, Esp, PE and PPE proteins, which are secreted as heterodimers and 10% of the genome of *M. tuberculosis* encodes for PE and PPE proteins (Ates, 2020). The function of the Type

VII secretion systems is co-dependent on a large number of substrates, through an unknown mechanism (Fortune *et al.*, 2005; DiGiuseppe Champion *et al.*, 2009; Chen *et al.*, 2013).

Because secretion systems are essential for the pathogenesis of many bacteria, understanding how secretion systems secrete effector proteins is pivotal to understand bacterial pathogenesis. Characterizing the different structural states of bacterial secretion systems can also give mechanistic insight into how they perform their function (Basler *et al.*, 2012; Kooger *et al.*, 2018; Hu *et al.*, 2020). Understanding the protein structure of bacterial secretion systems may also contribute to the development of effective vaccines and drugs that specifically recognize or interfere with secretion systems, or help characterize protective antibodies (McShan and De Guzman, 2015; Dong *et al.*, 2020; Huo *et al.*, 2020). Because secretion systems are large transmembrane protein complexes, it can be difficult, or even impossible, to isolate them from their native environment for structural studies while remaining intact (Kudryashev *et al.*, 2013; Kooger *et al.*, 2018).

The *in situ* structure of the T3SS has been determined in different species including *Salmonella enterica*, *Shigella flexneri*, *Yersinia enterocolitica*, and *Chlamydia trachomatis* (Kawamoto *et al.*, 2013; Kudryashev *et al.*, 2013; Hu *et al.*, 2015, 2017; Nans *et al.*, 2015). However, most of these studies have been performed in minicells and without host contact. For *Yersinia*, the structure of the sorting platform has not previously been determined and not in contact to host cells (Kudryashev *et al.*, 2013).

For the T7SS, structures of the isolated inner membrane core complexes of ESX-3 and ESX-5 have recently been determined (Beckham *et al.*, 2017; Famelis *et al.*, 2019; Poweleit *et al.*, 2019; Bunduc *et al.*, 2021), which gives insight into how it may function. However, it is currently unknown how T7SS substrates are transported across the bacterial outer membrane. This could occur in a one-step process, as is the case for all known secretion systems that span both the inner and outer membrane, or may possibly occur in two separate transport steps, like the type V secretion system that only spans the bacterial outer membrane (Costa *et al.*, 2015). It has also been hypothesized that PE-PPE protein heterodimers may act as autotransporters to cross the outer membrane (Ates, 2020) or that multimers of substrates form a conduit through the outer membrane (Bunduc *et al.*, 2020). Structural characterization of the entire T7SS in its native cellular environment may give insight in how the T7SS transports effector proteins across the outer membrane and whether it spans both the inner- and outer membrane. Identification and structural characterization of the protein complex responsible for transporting T7SS substrates across the bacterial outer membrane can benefit the development of effective vaccines and drugs against *M. tuberculosis*.

2. Cryo-electron microscopy for *in situ* structural biology

While X-ray crystallography remains the most commonly used structural technique to date (Protein Data Bank, 2021), transmission electron microscopy (TEM) has developed into a potent tool for studying protein structure. Electron microscopes allow image formation at a high resolution by shooting a coherent beam of electrons at a sample in a vacuum. The electrons interact with the sample before reaching an electron detector, allowing image formation. Two challenges posed by electron microscopy (EM) imaging of biological samples are that aqueous biological samples are destroyed by dehydrated in the vacuum in the column of electron microscopes at room temperature, and the low contrast of most biological samples, due to the low atomic number of elements predominantly present in cells. These were initially overcome by developing chemical cross-linking by chemical fixation and resin embedding, to replace the water from cells while retaining the cellular volume, and heavy metal staining techniques to add contrast to biological structures. The downsides of these techniques are that cellular and molecular details are deformed and an outline of biological structures is observed rather than the object itself, limiting the resolution that can be obtained. Cryogenic sample preparation techniques, where a biological sample is rapidly cooled to prevent the formation of crystalline ice allow for these fine molecular details to be preserved in a near-native state (Dubochet *et al.*, 1988). While structural studies using cryo-TEM were initially limited in resolution (Böttcher *et al.*, 1997; Matadeen *et al.*, 1999), several technological improvements in cryo-electron microscopy hardware, in particular direct electron detectors, and data processing enabled cryo-electron microscopy to develop into a potent structural technique (Kuhlbrandt, 2014; Koning *et al.*, 2018).

Two main cryo-EM structural applications have been developed to date: single particle analysis and cryo-electron tomography (CET). These processing techniques aim to align and average images of identical copies of a macromolecule to increase the signal-to-noise ratio and the final resolution. With single particle analysis, thousands or more images of macromolecules are extracted from cryo-EM micrographs, iteratively aligned and classified based on the orientation of the macromolecule, and projected into a volume to determine the 3D structure. In recent years, this technique allows for routine near-atomic structures to be determined of isolated macromolecules without the need to crystalize them (Cheng *et al.*, 2015) and more recently, even atomic-resolution structures (Nakane *et al.*, 2020; Yip *et al.*, 2020). Applying single particle to cellular samples is challenging, because cellular samples are typically thicker and more crowded, resulting in multiple macromolecules overlapping in the 2D micrograph.

CET overcomes this problem by recording a sequence of micrographs of the same area of a sample tilted at different angles termed a tilt-series. After alignment of the tilt-images, the tilt-series is reconstructed into a 3-dimensional volume of the sample termed a tomogram. Tomograms allow for 3D visualization of large macromolecules and complexes within

their native cellular environment. to produce a higher resolution average structure of a macromolecule, subvolumes (or sub-tilt-series) containing copies of a macromolecule are selected from (multiple) tomograms, and iteratively aligned in a process termed subtomogram averaging.

Where structural techniques such as X-ray crystallography and single-particle cryo-electron microscopy are limited to obtaining structures of isolated macromolecules (Shi, 2014; Cheng, 2015), cryo-electron tomography (CET) allows macromolecular structures to be determined within their native cellular environment (Turk and Baumeister, 2020). However, electrons have an increased probability of inelastic scattering events with increased sample thickness, which limits the resolution and signal with increased sample thickness. CET with a 200-300 kV electron microscope is therefore practically limited to below ±500 nm biological samples such as bacteria and the periphery of mammalian cells. To enable visualization of the cell interior with CET, different thinning strategies have been developed (Pierson *et al.*, 2011), including focused-ion-beam lamella preparation (Marko *et al.*, 2006, 2007). With this method, a focused-ion-beam is scanned over the sample, to locally ablate material. By removing material above and below a thin section of the cell at a shallow angle relative to the EM grid, a 50-300 nm thin slice of vitreous cellular material termed a lamella can be created, which that can be visualized with cryo-EM (Mahamid *et al.*, 2016; Schaffer *et al.*, 2017; Wagner *et al.*, 2020).Further development of CET on FIB lamellae does not only impact structural studies on bacterial secretion studies, but also enables the structural study of many other macromolecules and complexes in their native cellular environment.

3. Thesis outline

During this PhD project, we aimed to establish a CET on FIB-lamellae workflow that enables *in situ* structure determination of proteins with subtomogram averaging, in order to determine the *in situ* structure of the mycobacterial T7SS. Additionally, to help find ESX-1, we explored the potential of cryo-CLEM in this context. Based this experience, we review the newest developments in CET on FIB-lamellae for *in situ* structural biology, cryo-CLEM, recent applications of these techniques in biological studies, and their future potential in **Chapter 2**. We discovered a method to enable fiducial-based alignment of tilt-series recorded on FIB lamellae via endocytosis of bovine serum albumin coated nanogold particles. These findings are described in **Chapter 3**.

Next we used this newly established workflow to study the structure of T3SS to gain insight into how it functions during intracellular pathogenesis, and to validate that the newly established workflow is capable of determining the structure of a bacterial secretion system during intracellular infection. We collected a large dataset of over a 150 tilt-series of the intestinal pathogen *Yersinia enterocolitica* during intracellular infection of immune cells and

determined the structure of the entire T3SS (including the cytosolic sorting platform) with subtomogram averaging (**Chapter 4**). Next, we collected a large dataset of over 200 tilt-series of *Mycobacterium marinum* with the aim of determining the *in situ* structure of the T7SS ESX-1. We were unable to visually identify the T7SS or determine its structure, but we did identify many other protein complexes and ultrastructural features including proteinaceous storage compartments termed encapsulins. We determined the *in situ* structure of encapsulins and complemented this data with high-resolution single-particle structures of isolated encapsulins in partially and fully assembled states (**Chapter 5**). A discussion and conclusion of the other chapters is provided in **Chapter 6**.

References

Ates, L.S., 2020. New insights into the mycobacterial PE and PPE proteins provide a framework for future research. Mol. Microbiol. 113, 4–21. https://doi.org/10.1111/mmi.14409

Ates, L.S., Ummels, R., Commandeur, S., van der Weerd, R., Sparrius, M., Weerdenburg, E., Alber, M., Kalscheuer, R., Piersma, S.R., Abdallah, A.M., Abd El Ghany, M., Abdel-Haleem, A.M., Pain, A., Jiménez, C.R., Bitter, W., Houben, E.N.G., 2015. Essential Role of the ESX-5 Secretion System in Outer Membrane Permeability of Pathogenic Mycobacteria. PLOS Genet. 11, e1005190. https://doi.org/10.1371/journal.pgen.1005190

Basler, M., Pilhofer, M., Henderson, G.P., Jensen, G.J., Mekalanos, J.J., 2012. Type VI secretion requires a dynamic contractile phage tail-like structure. Nature 483, 182–186. https://doi.org/10.1038/nature10846

Beckham, K.S.H., Ciccarelli, L., Bunduc, C.M., Mertens, H.D.T., Ummels, R., Lugmayr, W., Mayr, J., Rettel, M., Savitski, M.M., Svergun, D.I., Bitter, W., Wilmanns, M., Marlovits, T.C., Parret, A.H.A., Houben, E.N.G., 2017. Structure of the mycobacterial ESX-5 type VII secretion system membrane complex by single-particle analysis. Nat. Microbiol. 2, 17047. https://doi.org/10.1038/nmicrobiol.2017.47

Bhoite, S., van Gerven, N., Chapman, M.R., Remaut, H., 2019. Curli Biogenesis: Bacterial Amyloid Assembly by the Type VIII Secretion Pathway. EcoSal Plus 8, 139–148. https://doi.org/10.1128/ecosalplus.ESP-0037-2018

Bliska, J.B., Wang, X., Viboud, G.I., Brodsky, I.E., 2013. Modulation of innate immune responses by *Yersinia* type III secretion system translocators and effectors. Cell. Microbiol. 15, 1622–31. https://doi.org/10.1111/cmi.12164

Böttcher, B., Wynne, S.A., Crowther, R.A., 1997. Determination of the fold of the core protein of hepatitis B virus by electron cryomicroscopy. Nature 386, 88–91. https://doi.org/10.1038/386088a0

Bunduc, C.M., Bitter, W., Houben, E.N.G., 2020. Structure and Function of the Mycobacterial Type VII Secretion Systems. Annu. Rev. Microbiol. 74, 315–335. https://doi.org/10.1146/annurev-micro-012420-081657

Bunduc, C.M., Fahrenkamp, D., Wald, J., Ummels, R., Bitter, W., Houben, E.N.G., Marlovits, T.C., 2021. Structure and dynamics of a mycobacterial type VII secretion system. Nature 593, 445–448. https://doi.org/10.1038/s41586-021-03517-z

Chen, J.M., Zhang, M., Rybniker, J., Boy-Röttger, S., Dhar, N., Pojer, F., Cole, S.T., 2013. *Mycobacterium tuberculosis* EspB binds phospholipids and mediates EsxA-independent virulence. Mol. Microbiol. 89, 1154–1166. https://doi.org/10.1111/mmi.12336

Cheng, Y., 2015. Single-Particle Cryo-EM at Crystallographic Resolution. Cell 161, 450–457. https://doi.org/10.1016/j.cell.2015.03.049

Cheng, Y., Grigorieff, N., Penczek, P.A., Walz, T., 2015. A Primer to Single-Particle Cryo-Electron Microscopy. Cell 161, 438–449. https://doi.org/10.1016/j.cell.2015.03.050

Conrad, W.H., Osman, M.M., Shanahan, J.K., Chu, F., Takaki, K.K., Cameron, J., Hopkinson-Woolley, D., Brosch, R., Ramakrishnan, L., 2017. Mycobacterial ESX-1 secretion system mediates host cell lysis through bacterium contact-dependent gross membrane disruptions. Proc. Natl. Acad. Sci. 114, 1371–1376. https://doi.org/10.1073/pnas.1620133114

Costa, T.R.D., Felisberto-Rodrigues, C., Meir, A., Prevost, M.S., Redzej, A., Trokter, M., Waksman, G., 2015. Secretion systems in Gram-negative bacteria: structural and mechanistic insights. Nat. Rev. Microbiol. 13, 343–359. https://doi.org/10.1038/nrmicro3456

de Jonge, M.I., Pehau-Arnaudet, G., Fretz, M.M., Romain, F., Bottai, D., Brodin, P., Honoré, N.,

Marchal, G., Jiskoot, W., England, P., Cole, S.T., Brosch, R., 2007. ESAT-6 from *Mycobacterium tuberculosis* Dissociates from Its Putative Chaperone CFP-10 under Acidic Conditions and Exhibits Membrane-Lysing Activity. J. Bacteriol. 189, 6028–6034. https://doi.org/10.1128/JB.00469-07

Deng, W., Marshall, N.C., Rowland, J.L., McCoy, J.M., Worrall, L.J., Santos, A.S., Strynadka, N.C.J., Finlay, B.B., 2017. Assembly, structure, function and regulation of type III secretion systems. Nat. Rev. Microbiol. 15, 323–337. https://doi.org/10.1038/nrmicro.2017.20

Diepold, A., Armitage, J.P., 2015. Type III secretion systems: the bacterial flagellum and the injectisome. Philos. Trans. R. Soc. B 370, 20150020. https://doi.org/10.1098/rstb.2015.0020

DiGiuseppe Champion, P. a., Champion, M.M., Manzanillo, P., Cox, J.S., 2009. ESX-1 secreted virulence factors are recognized by multiple cytosolic AAA ATPases in pathogenic mycobacteria. Mol. Microbiol. 73, 950–962. https://doi.org/10.1111/j.1365-2958.2009.06821.x

Dong, Y., Dai, T., Wei, Y., Zhang, L., Zheng, M., Zhou, F., 2020. A systematic review of SARS-CoV-2 vaccine candidates. Signal Transduct. Target. Ther. 5, 237. https://doi.org/10.1038/s41392-020-00352-y

Du, J., Reeves, A.Z., Klein, J.A., Twedt, D.J., Knodler, L.A., Lesser, C.F., 2016. The type III secretion system apparatus determines the intracellular niche of bacterial pathogens. Proc. Natl. Acad. Sci. 113, 4794–4799. https://doi.org/10.1073/pnas.1520699113

Dubochet, J., Adrian, M., Chang, J.-J., Homo, J.-C., Lepault, J., McDowall, A.W., Schultz, P., 1988. Cryo-electron microscopy of vitrified specimens. Q. Rev. Biophys. 21, 129–228. https://doi.org/10.1017/S0033583500004297

Engelenburg, S.B. Van, Palmer, A.E., 2010. Imaging type-III secretion reveals dynamics and spatial segregation of *Salmonella* effectors. Nat. Publ. Gr. 7, 325–330. https://doi.org/10.1038/nmeth.1437

Famelis, N., Rivera-Calzada, A., Degliesposti, G., Wingender, M., Mietrach, N., Skehel, J.M., Fernandez-Leiro, R., Böttcher, B., Schlosser, A., Llorca, O., Geibel, S., 2019. Architecture of the mycobacterial type VII secretion system. Nature 576, 321–325. https://doi.org/10.1038/s41586-019-1633-1

Fortune, S.M., Jaeger, A., Sarracino, D.A., Chase, M.R., Sassetti, C.M., Sherman, D.R., Bloom, B.R., Rubin, E.J., 2005. Mutually dependent secretion of proteins required for mycobacterial virulence. Proc. Natl. Acad. Sci. U. S. A. 102, 10676–10681. https://doi.org/10.1073/pnas.0504922102

Gorasia, D.G., Veith, P.D., Reynolds, E.C., 2020. The Type IX Secretion System: Advances in Structure, Function and Organisation. Microorganisms 8, 1173. https://doi.org/10.3390/microorganisms8081173

Gray, T.A., Clark, R.R., Boucher, N., Lapierre, P., Smith, C., Derbyshire, K.M., 2016. Intercellular communication and conjugation are mediated by ESX secretion systems in mycobacteria. Science 354, 347–350. https://doi.org/10.1126/science.aag0828

Gröschel, M.I., Sayes, F., Simeone, R., Majlessi, L., Brosch, R., 2016. ESX secretion systems: mycobacterial evolution to counter host immunity. Nat. Rev. Microbiol. https://doi.org/10.1038/nrmicro.2016.131

Houben, E.N.G., Bestebroer, J., Ummels, R., Wilson, L., Piersma, S.R., Jiménez, C.R., Ottenhoff, T.H.M., Luirink, J., Bitter, W., 2012. Composition of the type VII secretion system membrane complex. Mol. Microbiol. 86, 472–484. https://doi.org/10.1111/j.1365-2958.2012.08206.x

Hu, B., Lara-Tejero, M., Kong, Q., Galán, J.E., Liu, J., 2017. *In Situ* Molecular Architecture of the *Salmonella* Type III Secretion Machine. Cell 168, 1065–1074. https://doi.org/10.1016/j.cell.2017.02.022

Hu, B., Morado, D.R., Margolin, W., Rohde, J.R., Arizmendi, O., Picking, W.L., Picking, W.D., Liu, J., 2015. Visualization of the type III secretion sorting platform of *Shigella flexneri*. Proc. Natl. Acad. Sci. 112, 1047–1052. https://doi.org/10.1073/pnas.1411610112

Hu, J., Worrall, L.J., Strynadka, N.C., 2020. Towards capture of dynamic assembly and action of the T3SS at near atomic resolution. Curr. Opin. Struct. Biol. 61, 71–78. https://doi.org/10.1016/j.sbi.2019.10.005

Huo, J., Le Bas, A., Ruza, R.R., Duyvesteyn, H.M.E., Mikolajek, H., Malinauskas, T., Tan, T.K., Rijal, P., Dumoux, M., Ward, P.N., Ren, J., Zhou, D., Harrison, P.J., Weckener, M., Clare, D.K., Vogirala, V.K., Radecke, J., Moynié, L., Zhao, Y., Gilbert-Jaramillo, J., Knight, M.L., Tree, J.A., Buttigieg, K.R., Coombes, N., Elmore, M.J., Carroll, M.W., Carrique, L., Shah, P.N.M., James, W., Townsend, A.R., Stuart, D.I., Owens, R.J., Naismith, J.H., 2020. Neutralizing nanobodies bind SARS-CoV-2 spike RBD and block interaction with ACE2. Nat. Struct. Mol. Biol. 27, 846–854. https://doi.org/10.1038/s41594-020-0469-6

Kawamoto, A., Morimoto, Y. V, Miyata, T., Minamino, T., Hughes, K.T., Kato, T., Namba, K., 2013. Common and distinct structural features of *Salmonella* injectisome and flagellar basal body. Sci. Rep. 3, 3369. https://doi.org/10.1038/srep03369

Koning, R.I., Koster, A.J., Sharp, T.H., 2018. Advances in cryo-electron tomography for biology and medicine. Ann. Anat. - Anat. Anzeiger 217, 82–96. https://doi.org/10.1016/j.aanat.2018.02.004

Kooger, R., Szwedziak, P., Böck, D., Pilhofer, M., 2018. CryoEM of bacterial secretion systems. Curr. Opin. Struct. Biol. 52, 64–70. https://doi.org/10.1016/j.sbi.2018.08.007

Kudryashev, M., Stenta, M., Schmelz, S., Amstutz, M., Wiesand, U., Castaño-Díez, D., Degiacomi, M.T., Münnich, S., Bleck, C.K., Kowal, J., Diepold, A., Heinz, D.W., Dal Peraro, M., Cornelis, G.R., Stahlberg, H., 2013. *In situ* structural analysis of the *Yersinia enterocolitica* injectisome. Elife 2, e00792. https://doi.org/10.7554/eLife.00792

Kuhlbrandt, W., 2014. The Resolution Revolution. Science 343, 1443–1444. https://doi.org/10.1126/science.1251652

Mahamid, J., Pfeffer, S., Schaffer, M., Villa, E., Danev, R., Kuhn Cuellar, L., Forster, F., Hyman, A.A., Plitzko, J.M., Baumeister, W., 2016. Visualizing the molecular sociology at the HeLa cell nuclear periphery. Science 351, 969–972. https://doi.org/10.1126/science.aad8857

Marko, M., Hsieh, C., Moberlychan, W., Mannella, C.A., Frank, J., 2006. Focused ion beam milling of vitreous water: prospects for an alternative to cryo-ultramicrotomy of frozen-hydrated biological samples. J. Microsc. 222, 42–47. https://doi.org/10.1111/j.1365-2818.2006.01567.x

Marko, M., Hsieh, C., Schalek, R., Frank, J., Mannella, C., 2007. Focused-ion-beam thinning of frozen-hydrated biological specimens for cryo-electron microscopy. Nat. Methods 4, 215–217. https://doi.org/10.1038/nmeth1014

Matadeen, R., Patwardhan, A., Gowen, B., Orlova, E. V., Pape, T., Cuff, M., Mueller, F., Brimacombe, R., van Heel, M., 1999. The *Escherichia coli* large ribosomal subunit at 7.5 Å resolution. Structure 7, 1575–1583. https://doi.org/10.1016/S0969-2126(00)88348-3

McShan, A.C., De Guzman, R.N., 2015. The Bacterial Type III Secretion System as a Target for Developing New Antibiotics. Chem. Biol. Drug Des. 85, 30–42. https://doi.org/10.1111/cbdd.12422

Nakane, T., Kotecha, A., Sente, A., McMullan, G., Masiulis, S., Brown, P.M.G.E., Grigoras, I.T., Malinauskaite, L., Malinauskas, T., Miehling, J., Uchański, T., Yu, L., Karia, D., Pechnikova, E. V, de Jong, E., Keizer, J., Bischoff, M., McCormack, J., Tiemeijer, P., Hardwick, S.W., Chirgadze, D.Y., Murshudov, G., Aricescu, A.R., Scheres, S.H.W., 2020. Single-particle cryo-EM at atomic resolution. Nature 587, 152–156. https://doi.org/10.1038/s41586-020-2829-0

Nans, A., Kudryashev, M., Saibil, H.R., Hayward, R.D., 2015. Structure of a bacterial type III secretion system in contact with a host membrane *in situ*. Nat. Commun. 6, 10114. https://doi.org/10.1038/ncomms10114

Pierson, J., Ziese, U., Sani, M., Peters, P.J., 2011. Exploring vitreous cryo-section-induced compression at the macromolecular level using electron cryo-tomography; 80S yeast ribosomes appear unaffected. J. Struct. Biol. 173, 345–349. https://doi.org/10.1016/j.jsb.2010.09.017

Poweleit, N., Czudnochowski, N., Nakagawa, R., Trinidad, D.D., Murphy, K.C., Sassetti, C.M., Rosenberg, O.S., 2019. The structure of the endogenous ESX-3 secretion system. Elife 8, 1–20. https://doi.org/10.7554/eLife.52983

Protein Data Bank, 2021. https://doi.org/https://www.rcsb.org/stats/summary

Radics, J., Königsmaier, L., Marlovits, T.C., 2014. Structure of a pathogenic type 3 secretion system in action. Nat. Struct. Mol. Biol. 21, 82–87. https://doi.org/10.1038/nsmb.2722

Rossmann, F.M., Beeby, M., 2018. Insights into the evolution of bacterial flagellar motors from high-throughput *in situ* electron cryotomography and subtomogram averaging. Acta Crystallogr. Sect. D Struct. Biol. 74, 585–594. https://doi.org/10.1107/S2059798318007945

Schaffer, M., Mahamid, J., Engel, B.D., Laugks, T., Baumeister, W., Plitzko, J.M., 2017. Optimized cryo-focused ion beam sample preparation aimed at *in situ* structural studies of membrane proteins. J. Struct. Biol. 197, 73–82. https://doi.org/10.1016/j.jsb.2016.07.010

Serafini, A., Pisu, D., Palù, G., Rodriguez, G.M., Manganelli, R., 2013. The ESX-3 Secretion System Is Necessary for Iron and Zinc Homeostasis in *Mycobacterium tuberculosis*. PLoS One 8, e78351. https://doi.org/10.1371/journal.pone.0078351

Shi, Y., 2014. A Glimpse of Structural Biology through X-Ray Crystallography. Cell 159, 995–1014. https://doi.org/10.1016/j.cell.2014.10.051

Siegrist, M., Steigedal, M., Ahmad, R., 2014. Mycobacterial Esx-3 Requires Multiple Components for Iron Acquisition. MBio 5, 1–10. https://doi.org/10.1128/mBio.01073-14.Editor

Smith, J., Manoranjan, J., Pan, M., Bohsali, A., Xu, J., Liu, J., McDonald, K.L., Szyk, A., LaRonde-LeBlanc, N., Gao, L.-Y., 2008. Evidence for Pore Formation in Host Cell Membranes by ESX-1-Secreted ESAT-6 and Its Role in *Mycobacterium marinum* Escape from the Vacuole. Infect. Immun. 76, 5478–5487. https://doi.org/10.1128/IAI.00614-08

Turk, M., Baumeister, W., 2020. The promise and the challenges of cryo-electron tomography. FEBS Lett. 594, 3243–3261. https://doi.org/10.1002/1873-3468.13948

van der Wel, N., Hava, D., Houben, D., Fluitsma, D., van Zon, M., Pierson, J., Brenner, M., Peters, P.J., 2007. *M. tuberculosis* and *M. leprae* Translocate from the Phagolysosome to the Cytosol in Myeloid Cells. Cell 129, 1287–1298. https://doi.org/10.1016/j.cell.2007.05.059

Wagner, F.R., Watanabe, R., Schampers, R., Singh, D., Persoon, H., Schaffer, M., Fruhstorfer, P., Plitzko, J., Villa, E., 2020. Preparing samples from whole cells using focused-ion-beam milling for cryo-electron tomography. Nat. Protoc. 15, 2041–2070. https://doi.org/10.1038/s41596-020-0320-x

World Health Organisation, 2020. Global Tuberculosis Report.

Yip, K.M., Fischer, N., Paknia, E., Chari, A., Stark, H., 2020. Atomic-resolution protein structure determination by cryo-EM. Nature 6. https://doi.org/10.1038/s41586-020-2833-4

Chapter 2

Cryo–electron tomography on FIB lamellae transforms structural cell biology

Casper Berger, Navya Premarai, Raimond B. G. Ravelli, Kèvin Knoops, Carmen López-Iglesias, Peter J. Peters

Submitted

Chapter 3

Endocytosed nanogold fiducials for improved *in situ* cryo–electron tomography tilt-series alignment

Casper Berger, Raimond B. G. Ravelli, Carmen López-Iglesias, Peter J. Peters

Journal of Structural Biology (2021)

Abstract

Cryo–electron tomography (CET) on cryo–focused ion beam (FIB)–milled lamellae is becoming a powerful technique for determining the structure of macromolecular complexes in their native cellular environment. Prior to tomogram reconstruction, CET tilt-series recorded on FIB lamellae need to be aligned. Traditionally, CET tilt-series alignment is performed with 5–20 nm gold fiducials, but it has thus far proven difficult to apply this to FIB lamellae of eukaryotic cells. In here, we describe a simple method to allow uptake of bovine serum albumin (BSA)-gold fiducials into mammalian cells via endocytosis, which can subsequently be used as fiducials for tilt-series alignment of cryo-FIB lamellae. We compare the alignment of tilt-series with BSA-gold fiducials to fiducial-less patch-tracking, and find better alignment results with BSA-gold. This technique can contribute to understand cells at a structural and ultrastructural level with both cryo- and room-temperature electron tomography. Furthermore, fluorescently labeled BSA-gold has the potential to be used as fiducials for correlative light and electron microscopy studies.

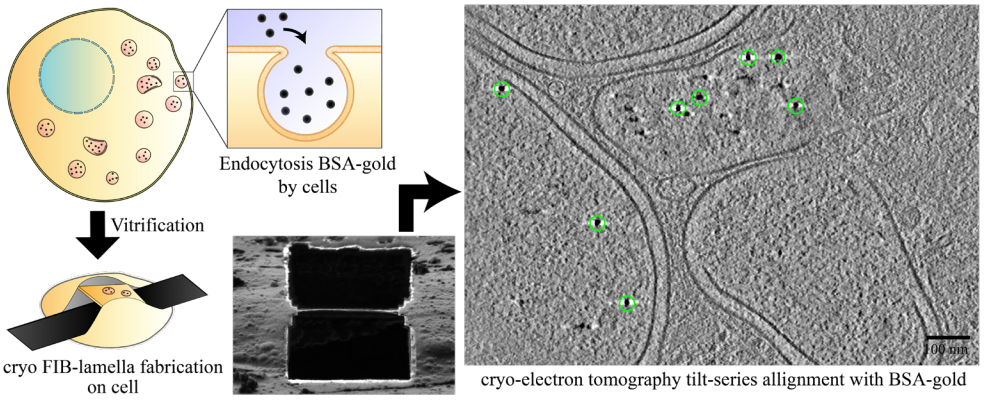

1. Introduction

Recent advances in cryo–electron microscopy have established single-particle analysis and cryo–electron tomography (CET) combined with subtomogram averaging as powerful methods for determining the structure of proteins (Kuhlbrandt, 2014; Turoňová *et al.*, 2017; O'Reilly *et al.*, 2020). Where single particle relies on the biochemical isolation of proteins, CET allows proteins to be studied in the native context of the cell. However, the increased probability of inelastic scattering events of electrons with increased sample thickness makes it impossible to use CET to image most areas of mammalian cells. Where sample thinning with vitreous cryo-sectioning causes artifacts such as compression and crevasses (Pierson *et al.*, 2011), it has recently become possible to overcome these limitations by using a cryo-focused ion-beam (FIB) to prepare ~200 nm–thick lamellae of cells (Marko *et al.*, 2007; Mahamid *et al.*, 2016a; Schaffer *et al.*, 2017). This allows for the structural study of protein complexes in their native cellular environment (Weiss *et al.*, 2019; Albert *et al.*, 2020; Wolff *et al.*, 2020).

In order to accurately reconstruct a 3-dimensional tomographic volume from a CET tilt-series, the individual tilted images need be aligned to correct for sample and stage movements, after alignment of different frames recorded at the same tilt angle (Zheng *et al.*, 2017). The generally preferred method is to add 5–20 nm gold nanoparticles to the sample prior to vitrification to act as fiducials during tilt-series alignment (Gruska *et al.*, 2008; Dobro *et al.*, 2017). The use of fiducials allows for accurate tilt-series alignment by correcting for non-rigid registration due to beam and stage-induced shifts as well as sample alterations (Karimi Nejadasl *et al.*, 2013; Mastronarde and Held, 2017; Fernandez *et al.*, 2018, 2019). However, adding fiducials to FIB-milled lamellae of eukaryotic cells has so far proven to be difficult. Nanogold particles in 2-methylpentane can be used to deposit fiducials to the lamella surface post-milling (Harapin *et al.*, 2015), but so far successful cases employing this method are limited. Fiducials can also be deposited on the grid before vitrification and used in FIB-wedges, because the grid foil is still present below the thinned cellular material (Jasnin *et al.*, 2019). However, they will not be visible in FIB-lamellae, where also the material below the lamella is removed, which causes the grid foil (with the gold fiducials) to only intersect with a small section of the tilted lamella.

Many fiducial-less alignment methods that use cross-correlations or feature tracking to create virtual fiducials have been developed (Owen and Landis, 1996; Lowe, 2004; Bay *et al.*, 2008; Han *et al.*, 2014; Noble and Stagg, 2015; Chen *et al.*, 2019), which are generally used in CET studies on FIB-lamellae (Mahamid *et al.*, 2016b; Bäuerlein *et al.*, 2017; Albert *et al.*, 2020). However, fiducial-less alignment can be challenging with the low signal-to-noise ratio typically present in CET tilt-series, in particular at high tilt angles. *In situ* structural research with CET on FIB-lamellae would benefit from a simple method to add nanogold fiducials to FIB-lamellae.

In this technical note, we describe how endocytosed, 10 nm bovine serum albumin (BSA)-coated gold nanoparticles can be used as fiducial for tilt-series alignment of cryo-tomograms recorded on FIB-lamellae of mammalian cells and show that the use of BSA-gold for tilt-series alignment results in higher quality tomographic reconstructions compared to fiducial-less alignment. This method may be used to better study the structural states of protein complexes in the native context of the cell with CET on FIB-lamellae and offers the potential to be used as fiducials for correlative light and electron microscopy as well.

2. Sample preparation

2.1 Cell culture & uptake of BSA-gold

Primary blood monocytes were isolated from a human blood buffy coat (Sanquin) with RosetteSep (Stemcell Technologies) as described by the manufacturer. Isolated monocytes were kept at 37 °C and 5% CO_2 in AIM V medium (Thermo Fisher Scientific, cat. 12055083) in non-tissue culture–treated petri dishes (Greiner, ref 633179) and differentiated into dendritic cells with 25 ng/ml interleukin-4 (IL-4) (PeproTech, cat 200-04) and 200 ng/ml granulocyte-macrophage colony-stimulating factor (GM-CSF) (PeproTech, cat 300-03) for 6 days. J774 cells were grown in RPMI (Thermo Fisher Scientific. Cat. 11875093) supplemented with 10% fetal bovine serum.

For vitrification, 400.000 cells were transferred to a 35 mm petri dish (Greiner,ref 627160) containing 8 UltrAufoil 200-mesh R2/2 grids (Russo and Passmore, 2014). Cells were infected with either *Yersinia enterocolitica* AD4334 (E40 ΔblaA Δasd ΔyopH ΔyopO ΔyopP ΔyopE ΔyopM ΔyopT) SctV-mCherry or *Escherichia coli* Rosetta 2(DE3) expressing the plasmid pQLinkN:EccB1-EccCa-EccCb1-mNG-His6-EccD1-EccE1 for 1 h before vitrification or infected with *Mycobacterium marinum* M^{USA} 16 h before vitrification. At 1 h before vitrification, 5 µl of 10 nm BSA-gold fiducials with an optical density (OD_{600}) of 235 (Cell Microscopy Core, University Medical Center Utrecht) were added to the cells in a total volume of 1 ml of medium with a final OD_{600} of 1.2 and allowed to be taken up via endocytosis.

For visualizing the distribution of BSA-gold with fluorescence microscopy, J774 mouse macrophages in RPMI medium were allowed to take up 5 nm BSA-gold fluorescently labeled with Alexa Fluor 488 dye (Cell Microscopy Core, University Medical Center Utrecht) with a final OD_{600} of 2.5 for 90 min. For visualizing the distribution of BSA-gold with EM on epon sections, J774 mouse macrophages in RPMI medium were allowed to take up 10 nm BSA-gold with a final OD_{600} of 1.2 for 60 min.

2.2 Fluorescence microscopy

Live J774 cells were imaged at 37 °C by recording Z-stacks with a CorrSight spinning disk confocal fluorescence microscope (Thermo Fisher Scientific) with a 40 × air objective

(Zeiss, 420363-9901-000) with 488 nm excitation in spinning disk mode. For visualization in figure 1A and B, maximum intensity projections of the Z-stacks were overlaid with in-focus transmitted light images of the cells. For Supplementary Movie 1, individual optical slices are shown as a movie.

2.3 Epon sectioning, EM overview acquisition and gold quantification

After uptake of 10 nm BSA gold, J774 cells were chemically fixed with 2.5% glutaraldehyde in 0.1 M phosphate buffer for 60 min at room temperature. Fixed cells were washed twice in 0.1 M phosphate buffer, followed by washing twice in 0.1 M cacodylate buffer. Postfixation was performed for 1 hour at 4 °C in 0.1 M cacodylate buffer with 1% osmium tetroxide and 1.5% $K_3Fe(CN)_8$, followed by washing 5 times in milli-Q. Dehydration was performed in ethanol at room temperature and cells were embedded in Epon. 130-140 nm thin sections were prepared using a microtome.

EM overviews were acquired with a Tecnai Arctica (Thermo Fisher Scientific) equipped with a Falcon III direct electron detector (Thermo Fisher Scientific), operating at 200 kV. Tilescan overviews were acquired with MAPS 3.7 (Thermo Fisher Scientific) with a pixelsize of 9.8 Å and 1.5 µm underfocus. Tilescan overviews were stitched with the FIJI grid/collection stitching plugin (Schindelin *et al.*, 2012). Distribution of 10 nm BSA-gold within the cell was determined on the stitched overviews by picking BSA-gold particles with the IMOD function imodfindbeads (Mastronarde and Held, 2017), followed by manual evaluation and correction of the model where required. Distribution of BSA-gold was visualized using IMOD.

2.4 Vitrification & lamellae preparation

Electron microscopy (EM) grids were vitrified with a modified vitrobot (Frederik and Hubert, 2005) (Thermo Fisher Scientific) with a custom-built jet vitrification device (Ravelli *et al.*, 2020) and a force sensor feedback loop to accurately apply a specific blot force. On the sample side of the blotting pads, a sheet of Teflon was used and on the backside, Whatman filter paper (Sigma-Aldrich, cat. no. 1001-055). EM grids were blotted for 5 s with a 2 s wait time before plunging, a chamber humidity of 80% at 37 °C and a blot force of 2.45 N.

Cryo-FIB lamellae were fabricated with a SCIOS FIB/SEM dual-beam (Thermo Fisher Scientific) which was upgraded to similar specifications as an Aquilos (Thermo Fisher Scientific). A thin (~5–10 nm, estimated based on the sputter-coating parameters) platinum layer was sputter-coated on the grid (6 s, 10 W, 600 V, 30 mA) and an overview of the grid was acquired with the SEM in MAPS software 3.1 (Thermo Fisher Scientific). Sites for lamellae fabrication were chosen and the eucentric positions were determined prior to applying an organometallic platinum layer with the gas injection system at three different areas of the grid for 3 s, resulting in an even layer thickness of approximately 1 µm as observed with the TEM during FIB-lamella fabrication. Cryo-FIB lamellae were prepared with rectangular pattern milling or wedge pre-milling with a current between 0.05 and 1 nA at an angle of 11°

relative to the grid with an initial width between 8 and 20 µm. A thin (~5 nm, as measured in the reconstructed tomograms) platinum layer was applied to the finished lamella (3 s, 10 W, 600 V, 30 mA).

2.5 CET and tilt-series alignment

CET was performed with a Tecnai Arctica (Thermo Fisher Scientific) equipped with a Falcon III direct electron detector (Thermo Fisher Scientific), with a pixel size of 2.73 Å and operating at 200 kV or a Titan Krios equipped with a K2 direct electron detector (Gatan), with a pixel size of 4.24 Å, operating at 300 kV and equipped with a Gatan Imaging Filter operating with a slit width of 20 eV. On both electron microscopes, cameras were operated in electron counting mode. Low-dose overviews of the lamellae were acquired to record tilt-series of biological targets of interest. For the Tecnai Arctica, low-dose tilescan overviews were acquired with MAPS 3.7 (Thermo Fisher Scientific) with a pixelsize of 12.9 Å, and 200 µm underfocus. For the Titan Krios, single image low-dose overviews were acquired at 1200 x magnification to capture the entire lamella in one image with 500 µm underfocus. Tilt-series were acquired with a bidirectional tilt scheme with 3° increments and an angular range of 51° to -51° with correction for the pre-tilt of the lamella for the data acquired with a Tecnai Arctica or 2° increments with an angular range of 50° to -50° corrected for the pre-tilt of the lamella for the data acquired with a Titan Krios. Tilt-series were recorded with Tomography 4 software (Thermo Fisher Scientific), a total fluence of 100 e-/Å^2 and 4-6 µm underfocus.

Dose fractions were aligned with MotionCor2 version 1.1 (Zheng *et al.*, 2017) and tilt-series were aligned with Etomo in IMOD version 4.10.28 (Mastronarde and Held, 2017). For fiducial-based alignment, unbinned tilt-series were used to automatically create the initial seed model with up to 250 points, followed by automatic tracking. The resulting fiducial model was manually corrected for errors, missing points and more gold particles were added. For points with a high displacement compared to the fit determined on all the points (high residual error), the centering of the points on the fiducials was manually iteratively improved. For fiducial-less alignment, patch-tracking in Etomo was used on 4 × binned tilt-series with a patch size of 200 × 200 pixels, a fractional overlap of 0.4 and 48 pixels away from the edges, resulting in 7 × 7 patches. Patches that were not tracking correctly were manually removed and tilt-images where most or all patches were not tracking correctly were excluded from being used to reconstruct the tomogram.

For comparing the alignment between fiducial-based and fiducial-less alignment, tilt-series were independently reconstructed by weighted back projection for both methods, and alignment parameters were extracted from the project folders with a bash script. Values for the residual error were converted to unbinned pixels. For visual comparison between fiducial-based and fiducial-less alignment, 2D slices in XY, YZ and XZ direction of the same BSA-gold or biological structures were extracted from both tomograms with a bash script. For visualization, reconstructed tomograms were filtered with TomDeconv (https://github.

com/dtegunov/tom_deconv/) with a signal-to-noise ratio falloff of 0.9 and the deconvolution strength set to 0.7. Movies of tomograms were recorded in IMOD.

3. Nanogold in mammalian cells

BSA-gold is generally not toxic to the cells and has been extensively used to study endocytosis and as therapeutic agents (Bolaños *et al.*, 2019). BSA-gold is known to be endocytosed by mammalian cells within minutes into early endosomes, reaching late endosomal organelles within 1 h (Kleijmeer *et al.*, 1997). We used fluorescently labeled, 5 nm BSA-gold to visualize its cellular distribution after endocytosis (Fig. 1A, B, Movie S1).

In order to get 5–20 nm nanogold fiducials into eukaryotic cells, we incubated the cells with BSA-gold for 1 h before vitrification. Some cytotoxicity has been observed after longer incubation times depending on cell type concentration, incubation time, and gold particle size (Khlebtsov and Dykman, 2011; Leopold *et al.*, 2017; Lillo *et al.*, 2020). We successfully used this method to get BSA-gold fiducials into FIB-lamellae of different cell types, including dendritic cells (Fig. 1C, Movie S2), primary human blood monocytes and dendritic cells infected with *Yersinia enterocolitica* (Fig. 1D, Movie S3), and the mouse macrophage cell line J774 infected with *Escherichia coli* (Fig. 1E, Movie S4); we observed BSA-gold in different endosomal organelles including endosomes, lysosomes, phagosomes as well as autophagosomal organelles after fusion with endosomal organelles. We therefore recommend to use incubation times up to 2 h, which is sufficient for a good distribution of BSA-gold into endosomal organelles.

To quantify the distribution of BSA-gold within the cell, we recorded EM tilescan overviews of epon section (Faas *et al.*, 2012) of J774 cells after 1 hour of BSA gold endocytosis, with a similar thickness to FIB lamellae (Sup. Fig. 1). We found a good distribution of BSA gold in endocytotic organelles throughout the cytosol with at least several thousand 10 nm BSA-gold particles in sections of different cells. The expected number of BSA-gold particles present in tilt-series depends on many factors, including the cell type, the size of the field of view and the subcellular localization of the biological target of interest. Based on the distribution in Sup. Fig. 1 and our experience in applying these techniques to different biological targets, we estimate the chance of having sufficient gold for alignment of a CET tilt-series recorded on a FIB-lamellae to be between 50-100% for a target that is not localized in the nucleus. The strategy of endocytosis of BSA-gold was particularly successful for a dataset with over 150 CET tilt-series recorded on FIB-lamellae of intracellular *Y. enterocolitica*, where each tilt-series could be aligned with a large number of BSA-gold particles. A wide range of cell types are known to endocytose BSA-gold (Geoffroy and Becker, 1984; Peters *et al.*, 1995; Bright *et al.*, 1997; De Heidi *et al.*, 1999; Lopes da Silva *et al.*, 2012; Galmes *et al.*, 2015), making this method widely applicable to many different samples for biological targets in or near organelles of endosomal origin.

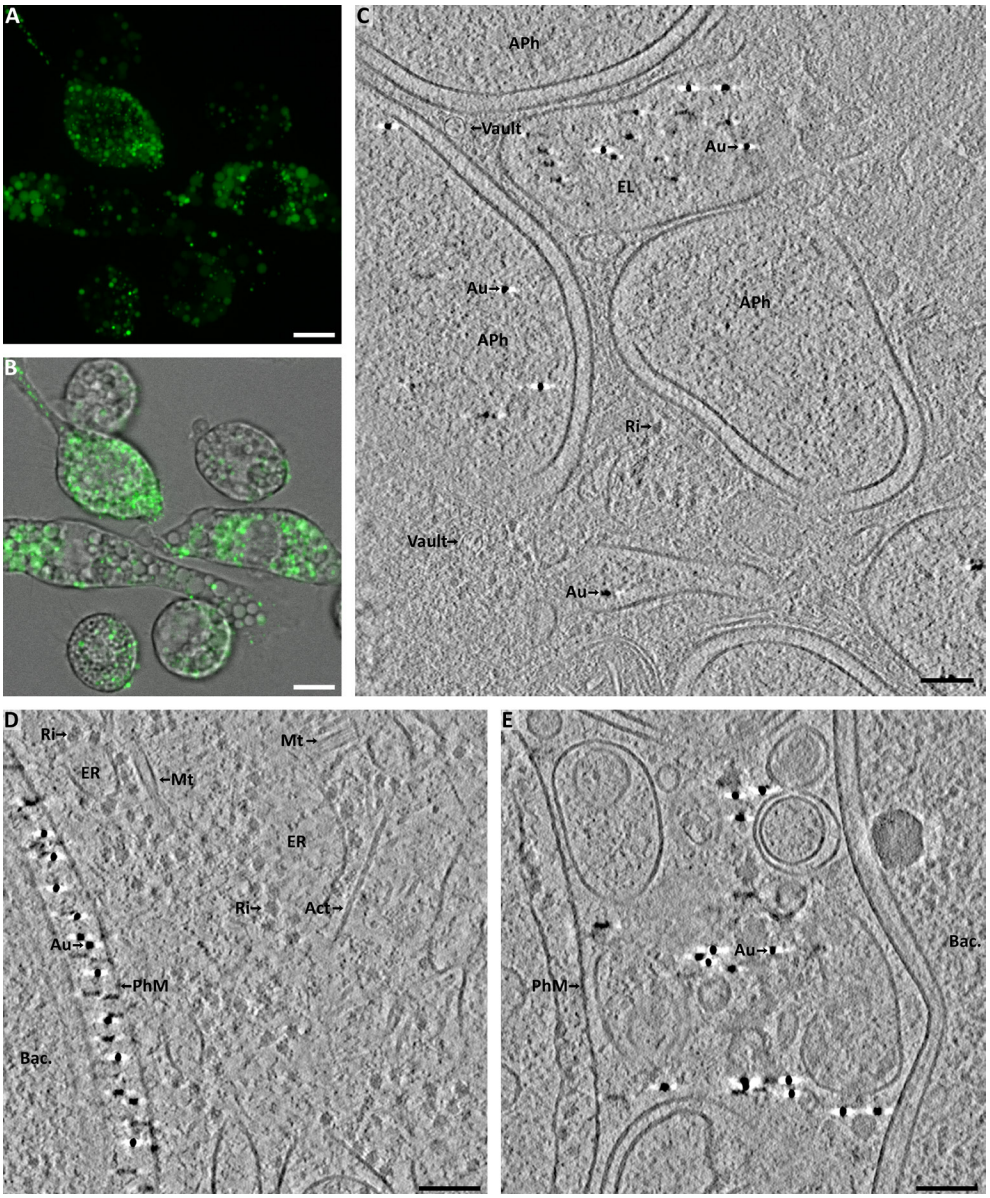

Figure 1. The use of BSA-gold fiducials to align CET tilt-series recorded on FIB-lamellae. (A) Distribution of 5 nm BSA-gold labeled with Alexa 488 in J774 mouse macrophages after 90 min of incubation. Scale bar: 10 µm. (B) Fluorescence image of A overlaid with transmitted light imaging of the cells. (C) Tomographic slice of a dendritic cells differentiated from primary human blood monocytes infected with *M. marinum* and incubated for 60 min prior to vitrification with 10 nm BSA-gold. The tomogram was recorded on an area where no intracellular bacteria are present. BSA-gold is present in different endo-lysosomal organelles (EL), including double membrane-enclosed organelles of autophagosomal origin (APh), which may contain BSA-gold because they have fused with endosomal organelles. A total of 70 BSA-gold particles (Au) are present in this tomogram. Many cytosolic ribosomes (Ri) and two vault complexes (Vault) (Woodward *et al.*, 2015) can be observed in this slice as well. Scale bar: 100 nm. (D) Tomographic slice of primary human blood monocytes differentiated into dendritic cells and infected with *Y. enterocolitica*. A large number of

10 nm BSA-gold particles (Au) are surrounding the bacterium in the tomographic volume because *Y. enterocolitica* is covered in a dense coat of the bacterial adhesin YadA (Hoiczyk, 2000), which binds to the BSA-gold. A total of 109 BSA-gold particles are present in this tomogram. The bacterium (Bac.) is enclosed by the phagosomal membrane (PhM). In the cytosol, the endoplasmic reticulum (ER) can be observed surrounded by ribosomes (Ri), actin (Act), and microtubules (Mt). Scale bar: 100 nm. (E) Tomographic slice of the mouse macrophage cell line J774 with intracellular *E. coli*. bacteria (Bac.) after phagocytosis. The bacteria are surrounded by a phagosomal membrane (PhM). The cellular material present in the organelle is likely from phagocytosis of cellular debris from apoptotic cell. A total of 127 BSA-gold particles (Au) are present in this tomogram. Scale bar: 100 nm.

4. Assessment of fiducial-based tilt-series alignment

The use of this method allows for BSA-gold to be used as fiducials to align tilt-series recorded on cryo-FIB lamellae of eukaryotic cells, which has several advantages over cross-correlation and feature-based, fiducial-less alignment. BSA-gold fiducials are very electron dense compared to the surrounding cellular material, which results in a high contrast and accurate tracking of the center of the BSA-gold particles, even at high tilt-angles where the electrons have a longer path through the biological sample. Because the BSA-gold particles are mostly spherical, they look nearly the same from all tilt angles, which makes it more accurate to determine the center. Accurate tracking of a large number of fiducials distributed throughout the sample in all dimensions allows a more precise determination of the tilt angles, rotations, and magnification as well as local correction of tilt-series and correction for motion of the sample during acquisition of the tilt-series (Mastronarde and Held, 2017; Fernandez *et al.*, 2018, 2019).

To compare the alignment quality of CET tilt-series recorded on FIB-lamellae aligned with BSA-gold or fiducial-less patch-tracking, we independently aligned sixteen tilt-series with both methods (Fig. 2, Table 1). Alignment with BSA-gold results in fewer reconstruction artifacts in both BSA-gold fiducials (Fig. 2B, C) and biological structures (Fig. 2D, E). When comparing the alignment parameters, we see that alignment with BSA-gold resulted in lower residual errors and that more contours could be tracked at all tilt-images (Table 1). These results indicate that alignment of tilt-series recorded on FIB-lamella with BSA-gold as fiducials gives higher quality tomographic reconstructions compared to fiducial-less patch tracking. Improvements in tilt-series alignment are known to be able to improve the resolution obtained with subtomogram averaging (Fernandez *et al.*, 2018, 2019; Himes and Zhang, 2018; Chen *et al.*, 2019). We therefore expect that the improved tilt-series alignment observed with BSA-gold may improve the resolution obtained with subtomogram averaging.

Alignment parameters of different tilt-series recorded on five different FIB-lamellae aligned with 10 nm BSA-gold fiducials, or fiducial-less patch tracking in Etomo (Mastronarde and Held, 2017). The sample type indicates whether the tilt-series was recorded on lamellae from dendritic cells (DC) infected with *Y. enterocolitica*, dendritic cells infected with *M. marinum*, or J774 macrophages infected with *E. coli*. The local lamella thickness was measured in the center of the reconstructed tomograms in nanometers. Tilt-series were either recorded

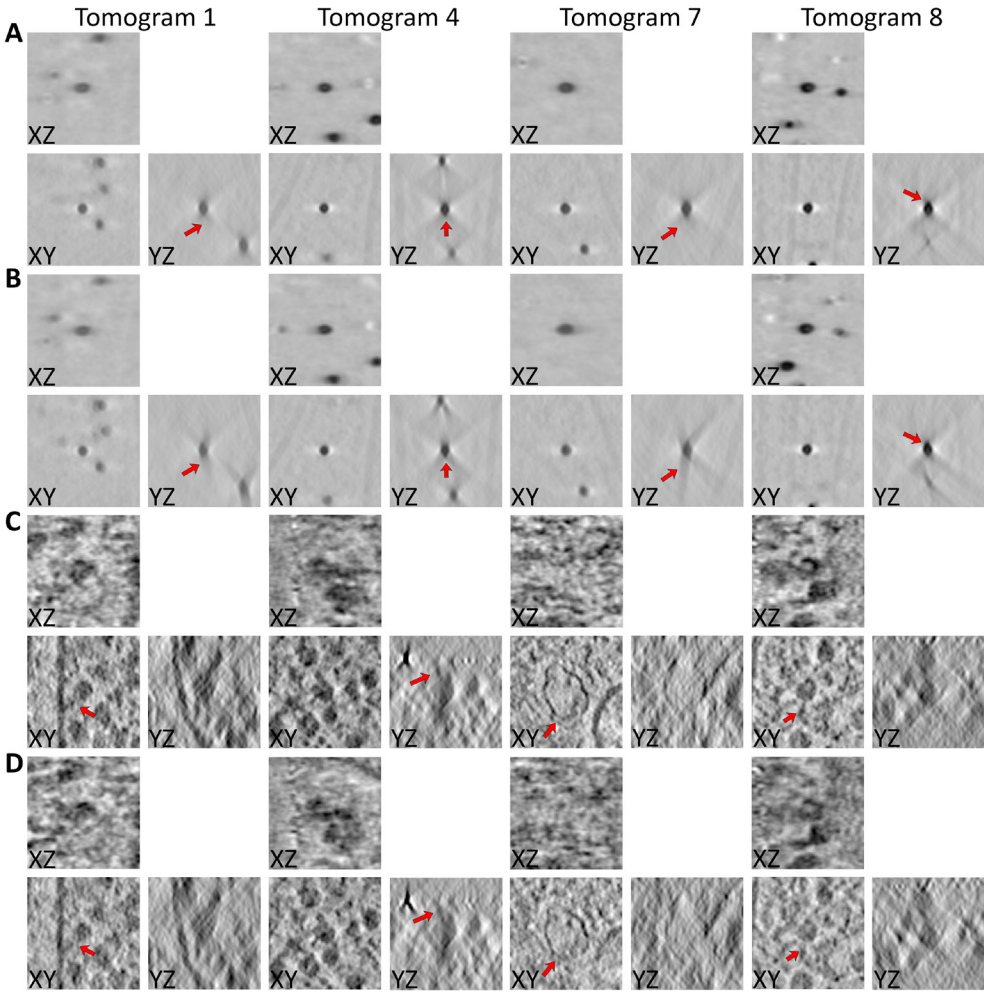

Figure 2. Comparison of tilt-series alignment quality with fiducials compared to fiducial-less alignment. Tilt-series from several different lamellae were independently aligned with 10 nm BSA-gold as fiducials and fiducial-less patch-tracking. (A, B) XY, YZ and XZ slices of 4 different BSA-gold particles from different tomograms aligned with the fiducials (A) or aligned with fiducial-less patch-tracking (B). Red arrows indicate areas of particular difference. (C, D) XY, YZ and XZ slices of biological features from tomograms aligned with BSA-gold fiducials (C) or fiducial-less patch-tracking (D). Tomogram 1, 4, and 8 show bacterial ribosomes of *Y. enterocolitica* and tomogram 7 a vault complex of the infected host cell. Red arrows indicate areas of particular difference

Table 1. Tilt-series alignment accuracy with or without BSA-gold fiducials

Tomo-gram	Sample type	Pixel size	Local lamella thickness (nm)	Average local mean residual error		Number of tracked contours		Points/contours ratio	
				Gold fiducial	Fiducial-less	Gold fiducial	Fiducial-less	Gold fiducial	Fiducial-less
#1	*DC - Y. ent.*	2.73	201	0.70	1.50	172	44	35.0	33.9
#2	*DC - Y. ent.*	2.73	232	0.70	3.22	99	45	31.0	31.0
#3	*DC - Y. ent.*	2.73	148	1.06	0.98	91	45	35.0	33.2
#4	*DC - Y. ent.*	2.73	94	0.92	0.86	116	47	34.9	35.0
#5	*DC - Y. ent.*	2.73	172	0.59	1.33	172	48	35.0	34.7
#6	*DC - Y. ent.*	2.73	134	0.73	1.04	226	48	35.0	34.7
#7	*DC - Y. ent.*	2.73	161	0.86	2.18	170	49	35.0	34.5
#8	*DC - Y. ent.*	2.73	81	1.18	1.01	52	49	35.0	34.8
#9*	*DC - Y. ent.*	2.73	185	0.71	1.97	109	49	35.0	34.0
#10*	J774 - *E. coli*	2.73	167	0.73	2.40	75	43	35.0	32.6
#11	*DC - M. mar.*	4.24	198	0.70	2.82	89	40	48.9	43.7
#12	*DC - M. mar.*	4.24	142	0.86	2.02	77	42	50.0	50.0
#13*	*DC - M. mar.*	4.24	165	0.92	3.06	68	35	47.3	48.3
#14	*DC - M. mar.*	4.24	117	0.77	1.73	151	40	49.6	49.1
#15	*DC - M. mar.*	4.24	331	0.89	3.99	24	32	51.0	39.4
#16	*DC - M. mar.*	4.24	353	1.09	4.50	51	33	48.1	43.8

with a Tecnai Arctica with a pixel size of 2.73 Å, or a Titan Krios with a pixel size of 4.24 Å. Tomogram #9, #10, and #13 (denoted with asterisks) are shown in Figure 1 D, E, and C, respectively. The average local mean residual error gives the mean displacement of all the individual points in pixels compared to the fit determined based on all the points and is a measure of how accurate the tilt-series are aligned. The number of contours are the total number of features tracked over all the different tilt images. The points/contours ratio, the total number of points in the whole tilt-series divided by the number of contours, indicates how well features could be tracked at all tilt angles. Thirty-five tilt-images were recorded for tomograms #1 to #10, but 4 tilt images were not used to reconstruct the final tomogram for tomogram #2. For tomograms #11 to #16, 50 tilt images were recorded, except for #15, for which 51 tilt images were recorded.

5. Conclusion

In this technical note, we provide a simple method to get BSA-gold fiducials into eukaryotic cells via endocytosis, which enables the accurate alignment of CET tilt-series recorded on FIB-lamellae with gold fiducials. Furthermore, we demonstrate its successful application for different cell types and show its subcellular distribution. Whether sufficient BSA-gold is consistently present around a biological target of interest for tilt-series alignment depends on different factors. Thus, the suitability of this technique will need to be assessed for different use cases.

We show better tilt-series alignment with BSA-gold compared to fiducial-less alignment methods that are commonly employed. The strong contrast of the BSA-gold also benefits fiducial-less alignment, so larger benefits are expected when comparing FIB-lamellae with and without BSA-gold. This method supports the use of CET on FIB-lamellae to study the structure of protein complexes in their native cellular environment. One of the downsides of the use of gold fiducials is that they may cause streak artifacts near the gold particles caused by the missing wedge. This can be mostly negated by the computational removal of the gold particle in the tilt-series during the reconstruction process.

Recently, the use of per-particle refinement of tilt parameters has shown great promise of improving the resolution of the final subtomogram averages, even on *in situ* samples (Himes and Zhang, 2018; Chen *et al.*, 2019; O'Reilly *et al.*, 2020). BSA-gold fiducials can be used in conjunction with this technique for high-quality, (semi-) automated alignment of the tilt-series prior to per-particle refinement. Other uses include research questions that do not require subtomogram averaging as well as for traditional electron tomography at room temperature. Additionally, the use of BSA-gold also helps in identifying organelles, since they are only present in organelles of endosomal origin. Finally, endocytosis of fluorescently labeled BSA-gold (Fokkema *et al.*, 2018) may potentially be used as fiducials to accurately correlate

cryo-fluorescence microscopy data with CET on FIB lamellae (Wolff *et al.*, 2016; Bharat *et al.*, 2018; Kuba *et al.*, 2021).

Appendices and supplementary information

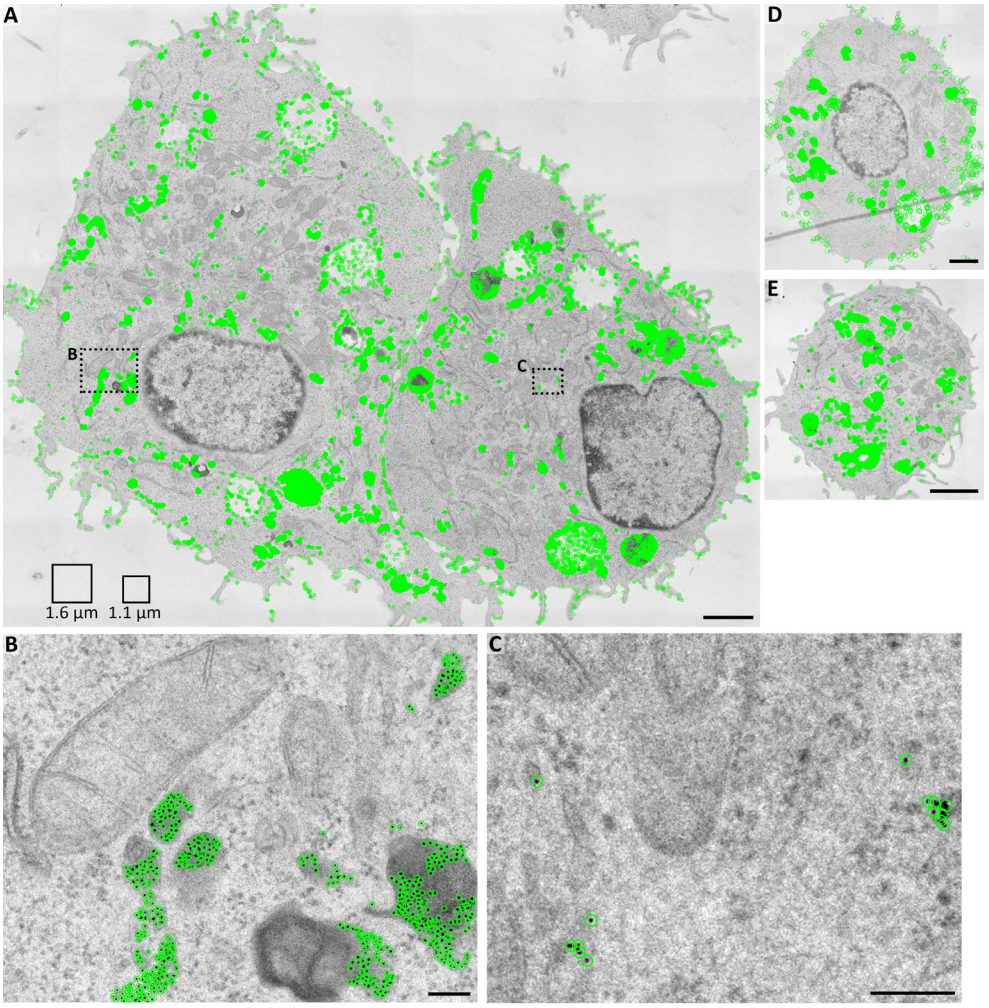

Supplementary Figure 1. Distribution of BSA gold within epon sections of J774 cells after 1 h of endocytosis of BSA gold. Sections have a thickness of 130-140 nm as determined with tomography (data not shown), which equates to an approximately 160-170 nm thick lamella when accounting for sample shrinkage during dehydration. (A) Stitched tilescan showing the distribution of BSA-gold in endocytotic organelles throughout the cell (except in the nucleus). 10 nm BSA-gold fiducials are marked with green circles. In the section of the cell on the left, a total of 35634 10nm BSA-gold fiducials were found and in the cell on the right 23579. The size of field of view for tilt-series acquired in this studies on FIB-lamellae with the Titan Krios (1.6 µm x 1.6 µm) and Tecnai Arctica (1.1 µm) are indicated in the bottom left (rectangles with black lines). Areas shown in panel B and C are indicated (rectangles with black dashed lines). Scalebars: 2 µm. (B,C) enlarged areas of panel A on the left and right cell respectively. Scalebar: 200 nm. (D,E) stitched tilescan overviews of other cells. A total of 19648 10 nm BSA-gold fiducials were found in the section of the cell in panel D and 3296 in the section of the cell shown in panel E. Scalebar: 2.5 µm.

Supplementary Movie 1. Movie of of the Z-stack that is shown as a maximum intensity projection in Figure 1A. Scale bar: 10 µm.

Supplementary Movie 2. Movie of the tomogram shown in Figure 1C. The 10 nm BSA-gold fiducials are marked in green in the second half of the movie. Scale bar: 100 nm.

Supplementary Movie 3. Movie of the tomogram shown in Figure 1D. The 10 nm BSA-gold fiducials are marked in green in the second half of the movie. Scale bar: 100 nm.

Supplementary Movie 4. Movie of the tomogram shown in Figure 1E. The 10 nm BSA-gold fiducials are marked in green in the second half of the movie. Scale bar: 100 nm.

Author contribution

Casper Berger: conceptualization, investigation, Writing - Original Draft. Raimond Ravelli: writing – review & editing. Carmen López-Iglesias: writing – review & editing. Peter Peters: conceptualization, writing – review & editing.

Acknowledgments

The UM acknowledge co-funding by the PPP Allowance made available by Health~Holland, Top Sector Life Sciences & Health, to stimulate public-private partnerships, under project number LHSM18067, as well as from the Netherlands Organisation for Scientific Research (NWO) in the framework of the National Roadmap NEMI project number 184.034.014.

We thank the Microscopy CORE Lab of M4i-FHML at Maastricht University for their technical and scientific support. We thank Hang Nguyen for editing the manuscript. We thank the Cell Microscopy Core (Department of Cell Biology, University Medical Center Utrecht) for their kind gift of the 5 nm BSA-gold labeled with Alexa 488. We thank Christof Diebolder and Rebecca Dillard for their assistance with data acquisition with a Titan Krios at the Netherlands Centre for Electron Nanoscopy (NeCEN).

References

Albert, S., Wietrzynski, W., Lee, C.-W., Schaffer, M., Beck, F., Schuller, J.M., Salomé, P.A., Plitzko, J.M., Baumeister, W., Engel, B.D., 2020. Direct visualization of degradation microcompartments at the ER membrane. Proc. Natl. Acad. Sci. 117, 1069–1080. https://doi.org/10.1073/pnas.1905641117

Bäuerlein, F.J.B., Saha, I., Mishra, A., Kalemanov, M., Martínez-Sánchez, A., Klein, R., Dudanova, I., Hipp, M.S., Hartl, F.U., Baumeister, W., Fernández-Busnadiego, R., 2017. *In Situ* Architecture and Cellular Interactions of PolyQ Inclusions. Cell 171, 179-187.e10. https://doi.org/10.1016/j.cell.2017.08.009

Bay, H., Ess, A., Tuytelaars, T., Van Gool, L., 2008. Speeded-Up Robust Features (SURF). Comput. Vis. Image Underst. 110, 346–359. https://doi.org/10.1016/j.cviu.2007.09.014

Bharat, T.A.M., Hoffmann, P.C., Kukulski, W., 2018. Correlative Microscopy of Vitreous Sections Provides Insights into BAR-Domain Organization *In Situ*. Structure 26, 879-886.e3. https://doi.org/10.1016/j.str.2018.03.015

Bolaños, K., Kogan, M.J., Araya, E., 2019. Capping gold nanoparticles with albumin to improve their biomedical properties. Int. J. Nanomedicine Volume 14, 6387–6406. https://doi.org/10.2147/IJN.S210992

Bright, N.A., Reaves, B.J., Mullock, B.M., Luzio, J.P., 1997. Dense core lysosomes can fuse with late endosomes and are re-formed from the resultant hybrid organelles. J. Cell Sci. 110, 2027–2040.

Chen, M., Bell, J.M., Shi, X., Sun, S.Y., Wang, Z., Ludtke, S.J., 2019. A complete data processing workflow for cryo-ET and subtomogram averaging. Nat. Methods 16, 1161–1168. https://doi.org/10.1038/s41592-019-0591-8

De Heidi, W., Lichtenstein, Y., Geuze, H.J., Kelly, R.B., Van Der Sluijs, P., Klumperman, J., 1999. Synaptic vesicles form by budding from tubular extensions of sorting endosomes in PC12 cells. Mol. Biol. Cell 10, 4163–4176. https://doi.org/10.1091/mbc.10.12.4163

Dobro, M.J., Oikonomou, C.M., Piper, A., Cohen, J., Guo, K., Jensen, T., Tadayon, J., Donermeyer, J., Park, Y., Solis, B.A., Kjær, A., Jewett, A.I., McDowall, A.W., Chen, S., Chang, Y.-W., Shi, J., Subramanian, P., Iancu, C. V., Li, Z., Briegel, A., Tocheva, E.I., Pilhofer, M., Jensen, G.J., 2017. Uncharacterized Bacterial Structures Revealed by Electron Cryotomography. J. Bacteriol. 199, 1–14. https://doi.org/10.1128/JB.00100-17

Faas, F.G.A., Avramut, M.C., M. van den Berg, B., Mommaas, A.M., Koster, A.J., Ravelli, R.B.G., 2012. Virtual nanoscopy: Generation of ultra-large high resolution electron microscopy maps. J. Cell Biol. 198, 457–469. https://doi.org/10.1083/jcb.201201140

Fernandez, J.-J., Li, S., Agard, D.A., 2019. Consideration of sample motion in cryo-tomography based on alignment residual interpolation. J. Struct. Biol. 205, 1–6. https://doi.org/10.1016/j.jsb.2019.01.005

Fernandez, J.-J., Li, S., Bharat, T.A.M., Agard, D.A., 2018. Cryo-tomography tilt-series alignment with consideration of the beam-induced sample motion. J. Struct. Biol. 202, 200–209. https://doi.org/10.1016/j.jsb.2018.02.001

Fokkema, J., Fermie, J., Liv, N., van den Heuvel, D.J., Konings, T.O.M., Blab, G.A., Meijerink, A., Klumperman, J., Gerritsen, H.C., 2018. Fluorescently Labelled Silica Coated Gold Nanoparticles as Fiducial Markers for Correlative Light and Electron Microscopy. Sci. Rep. 8, 13625. https://doi.org/10.1038/s41598-018-31836-1

Frederik, P.M., Hubert, D.H.W., 2005. Cryoelectron Microscopy of Liposomes, in: Methods in Enzymology. pp. 431–448. https://doi.org/10.1016/S0076-6879(05)91024-0

Galmes, R., ten Brink, C., Oorschot, V., Veenendaal, T., Jonker, C., van der Sluijs, P., Klumperman,

J., 2015. Vps33B is required for delivery of endocytosed cargo to lysosomes. Traffic 16, 1288–1305. https://doi.org/10.1111/tra.12334

Geoffroy, J.S., Becker, R.P., 1984. Endocytosis by endothelial phagocytes: uptake of bovine serum albumin-gold conjugates in bone marrow. J. Ultrasructure Res. 89, 223–239. https://doi.org/10.1016/S0022-5320(84)80039-8

Gruska, M., Medalia, O., Baumeister, W., Leis, A., 2008. Electron tomography of vitreous sections from cultured mammalian cells. J. Struct. Biol. 161, 384–392. https://doi.org/10.1016/j.jsb.2007.10.008

Han, R., Zhang, F., Wan, X., Fernández, J.J., Sun, F., Liu, Z., 2014. A marker-free automatic alignment method based on scale-invariant features. J. Struct. Biol. 186, 167–180. https://doi.org/10.1016/j.jsb.2014.02.011

Harapin, J., Börmel, M., Sapra, K.T., Brunner, D., Kaech, A., Medalia, O., 2015. Structural analysis of multicellular organisms with cryo-electron tomography. Nat. Methods 12, 634–636. https://doi.org/10.1038/nmeth.3401

Himes, B.A., Zhang, P., 2018. emClarity: software for high-resolution cryo-electron tomography and subtomogram averaging. Nat. Methods 15, 955–961. https://doi.org/10.1038/s41592-018-0167-z

Hoiczyk, E., 2000. Structure and sequence analysis of *Yersinia* YadA and Moraxella UspAs reveal a novel class of adhesins. EMBO J. 19, 5989–5999. https://doi.org/10.1093/emboj/19.22.5989

Jasnin, M., Beck, F., Ecke, M., Fukuda, Y., Martinez-Sanchez, A., Baumeister, W., Gerisch, G., 2019. The Architecture of Traveling Actin Waves Revealed by Cryo-Electron Tomography. Structure 27, 1211-1223.e5. https://doi.org/10.1016/j.str.2019.05.009

Karimi Nejadasl, F., Karuppasamy, M., Newman, E.R., McGeehan, J.E., Ravelli, R.B.G., 2013. Non-rigid image registration to reduce beam-induced blurring of cryo-electron microscopy images. J. Synchrotron Radiat. 20, 58–66. https://doi.org/10.1107/S0909049512044408

Khlebtsov, N., Dykman, L., 2011. Biodistribution and toxicity of engineered gold nanoparticles: a review of *in vitro* and *in vivo* studies. Chem. Soc. Rev. 40, 1647–1671. https://doi.org/10.1039/C0CS00018C

Kleijmeer, M.J., Morkowski, S., Griffith, J.M., Rudensky, A.Y., Geuze, H.J., 1997. Major histocompatibility complex class II compartments in human and mouse B lymphoblasts represent conventional endocytic compartments. J. Cell Biol. 139, 639–649. https://doi.org/10.1083/jcb.139.3.639

Kuba, J., Mithchels, J., Hovorka, M., Erdmann, P., Berka, L., Kirmse, R., König, J., De bock, J., Goetze, B., Rigort, A., 2021. Advanced cryo-tomography workflow developments – correlative microscopy, milling automation and cryo-lift-out. J. Microsc. 281, 112–124. https://doi.org/10.1111/jmi.12939

Kuhlbrandt, W., 2014. The Resolution Revolution. Science 343, 1443–1444. https://doi.org/10.1126/science.1251652

Leopold, L.F., Tódor, I.S., Diaconeasa, Z., Rugină, D., Ştefancu, A., Leopold, N., Coman, C., 2017. Assessment of PEG and BSA-PEG gold nanoparticles cellular interaction. Colloids Surfaces A Physicochem. Eng. Asp. 532, 70–76. https://doi.org/10.1016/j.colsurfa.2017.06.061

Lillo, C.R., Calienni, M.N., Rivas Aiello, B., Prieto, M.J., Rodriguez Sartori, D., Tuninetti, J., Toledo, P., Alonso, S. del V., Moya, S., Gonzalez, M.C., Montanari, J., Soler-Illia, G.J.A.A., 2020. BSA-capped gold nanoclusters as potential theragnostic for skin diseases: Photoactivation, skin penetration, *in vitro*, and *in vivo* toxicity. Mater. Sci. Eng. C 112, 110891. https://doi.org/10.1016/j.msec.2020.110891

Lopes da Silva, M., Thieleke-Matos, C., Cabrita-Santos, L., Ramalho, J.S., Wavre-Shapton, S.T., Futter,

C.E., Barral, D.C., Seabra, M.C., 2012. The Host Endocytic Pathway is Essential for Plasmodium berghei Late Liver Stage Development. Traffic 13, 1351–1363. https://doi.org/10.1111/j.1600-0854.2012.01398.x

Lowe, D.G., 2004. Distinctive Image Features from Scale-Invariant Keypoints. Int. J. Comput. Vis. 60, 91–110. https://doi.org/10.1023/B:VISI.0000029664.99615.94

Mahamid, J., Pfeffer, S., Schaffer, M., Villa, E., Danev, R., Kuhn Cuellar, L., Forster, F., Hyman, A.A., Plitzko, J.M., Baumeister, W., 2016a. Visualizing the molecular sociology at the HeLa cell nuclear periphery. Science 351, 969–972. https://doi.org/10.1126/science.aad8857

Mahamid, J., Pfeffer, S., Schaffer, M., Villa, E., Danev, R., Kuhn Cuellar, L., Forster, F., Hyman, A.A., Plitzko, J.M., Baumeister, W., 2016b. Visualizing the molecular sociology at the HeLa cell nuclear periphery. Science 351, 969–972. https://doi.org/10.1126/science.aad8857

Marko, M., Hsieh, C., Schalek, R., Frank, J., Mannella, C., 2007. Focused-ion-beam thinning of frozen-hydrated biological specimens for cryo-electron microscopy. Nat. Methods 4, 215–217. https://doi.org/10.1038/nmeth1014

Mastronarde, D.N., Held, S.R., 2017. Automated tilt series alignment and tomographic reconstruction in IMOD. J. Struct. Biol. 197, 102–113. https://doi.org/10.1016/j.jsb.2016.07.011

Noble, A.J., Stagg, S.M., 2015. Automated batch fiducial-less tilt-series alignment in Appion using Protomo. J. Struct. Biol. 192, 270–278. https://doi.org/10.1016/j.jsb.2015.10.003

O'Reilly, F.J., Xue, L., Graziadei, A., Sinn, L., Lenz, S., Tegunov, D., Blötz, C., Singh, N., Hagen, W.J.H., Cramer, P., Stülke, J., Mahamid, J., Rappsilber, J., 2020. In-cell architecture of an actively transcribing-translating expressome. Science 369, 554–557. https://doi.org/10.1126/science.abb3758

Owen, C.H., Landis, W.J., 1996. Alignment of electron tomographic series by correlation without the use of gold particles. Ultramicroscopy 63, 27–38. https://doi.org/10.1016/0304-3991(95)00154-9

Peters, P.J., Raposo, G., Neefjes, J.J., Oorschot, V., Leijendekker, R.L., Geuze, H.J., Ploegh, H.L., 1995. Major histocompatibility complex class II compartments in human B lymphoblastoid cells are distinct from early endosomes. J. Exp. Med. 182, 325–334. https://doi.org/10.1084/jem.182.2.325

Pierson, J., Ziese, U., Sani, M., Peters, P.J., 2011. Exploring vitreous cryo-section-induced compression at the macromolecular level using electron cryo-tomography; 80S yeast ribosomes appear unaffected. J. Struct. Biol. 173, 345–349. https://doi.org/10.1016/j.jsb.2010.09.017

Ravelli, R.B.G., Nijpels, F.J.T., Henderikx, R.J.M., Weissenberger, G., Thewessem, S., Gijsbers, A., Beulen, B.W.A.M.M., López-Iglesias, C., Peters, P.J., 2020. Cryo-EM structures from sub-nl volumes using pin-printing and jet vitrification. Nat. Commun. 11, 2563. https://doi.org/10.1038/s41467-020-16392-5

Russo, C.J., Passmore, L.A., 2014. Ultrastable gold substrates for electron cryomicroscopy. Science 346, 1377–1380. https://doi.org/10.1126/science.1259530

Schaffer, M., Mahamid, J., Engel, B.D., Laugks, T., Baumeister, W., Plitzko, J.M., 2017. Optimized cryo-focused ion beam sample preparation aimed at *in situ* structural studies of membrane proteins. J. Struct. Biol. 197, 73–82. https://doi.org/10.1016/j.jsb.2016.07.010

Schindelin, J., Arganda-Carreras, I., Frise, E., Kaynig, V., Longair, M., Pietzsch, T., Preibisch, S., Rueden, C., Saalfeld, S., Schmid, B., Tinevez, J.-Y., White, D.J., Hartenstein, V., Eliceiri, K., Tomancak, P., Cardona, A., 2012. Fiji: an open-source platform for biological-image analysis. Nat. Methods 9, 676–682. https://doi.org/10.1038/nmeth.2019

Turoňová, B., Schur, F.K.M., Wan, W., Briggs, J.A.G., 2017. Efficient 3D-CTF correction for cryo-electron tomography using NovaCTF improves subtomogram averaging resolution to 3.4 Å. J.

Struct. Biol. 199, 187–195. https://doi.org/10.1016/j.jsb.2017.07.007

Weiss, G.L., Kieninger, A.-K., Maldener, I., Forchhammer, K., Pilhofer, M., 2019. Structure and Function of a Bacterial Gap Junction Analog. Cell 178, 374-384.e15. https://doi.org/10.1016/j.cell.2019.05.055

Wolff, G., Hagen, C., Grünewald, K., Kaufmann, R., 2016. Towards correlative super-resolution fluorescence and electron cryo-microscopy. Biol. Cell 108, 245–258. https://doi.org/10.1111/boc.201600008

Wolff, G., Limpens, R.W.A.L., Zevenhoven-Dobbe, J.C., Laugks, U., Zheng, S., de Jong, A.W.M., Koning, R.I., Agard, D.A., Grünewald, K., Koster, A.J., Snijder, E.J., Bárcena, M., 2020. A molecular pore spans the double membrane of the coronavirus replication organelle. Science 369, 1395–1398. https://doi.org/10.1126/science.abd3629

Woodward, C.L., Mendonça, L.M., Jensen, G.J., 2015. Direct visualization of vaults within intact cells by electron cryo-tomography. Cell. Mol. Life Sci. 72, 3401–3409. https://doi.org/10.1007/s00018-015-1898-y

Zheng, S.Q., Palovcak, E., Armache, J.-P., Verba, K.A., Cheng, Y., Agard, D.A., 2017. MotionCor2: anisotropic correction of beam-induced motion for improved cryo-electron microscopy. Nat. Methods 14, 331–332. https://doi.org/10.1038/nmeth.4193

Chapter 4

Structure of the *Yersinia* injectisome in intracellular host cell phagosomes revealed by cryo FIB electron tomography

Casper Berger, Raimond B. G. Ravelli, Carmen López-Iglesias, Mikhail Kudryashev,

Andreas Diepold, Peter J. Peters

Journal of Structural Biology (2021)

Abstract

Many pathogenic bacteria use the type III secretion system (T3SS), or injectisome, to secrete toxins into host cells. These protruding systems are primary targets for drug and vaccine development. Upon contact between injectisomes and host membranes, toxin secretion is triggered. How this works structurally and functionally is yet unknown. Using cryo-focused ion beam milling and cryo-electron tomography, we visualized injectisomes of *Yersinia enterocolitica* inside the phagosomes of infected human myeloid cells in a close-to-native state. We observed that a minimum needle length is required for injectisomes to contact the host membrane and bending of host membranes by some injectisomes that contact the host. Through subtomogram averaging, the structure of the entire injectisome was determined, which revealed structural differences in the cytosolic sorting platform compared to other bacteria. These findings contribute to understanding how injectisomes secrete toxins into host cells and provides the indispensable native context. The application of these cryo-electron microscopy techniques paves the way for the study of the 3D structure of infection-relevant protein complexes in host-pathogen interactions.

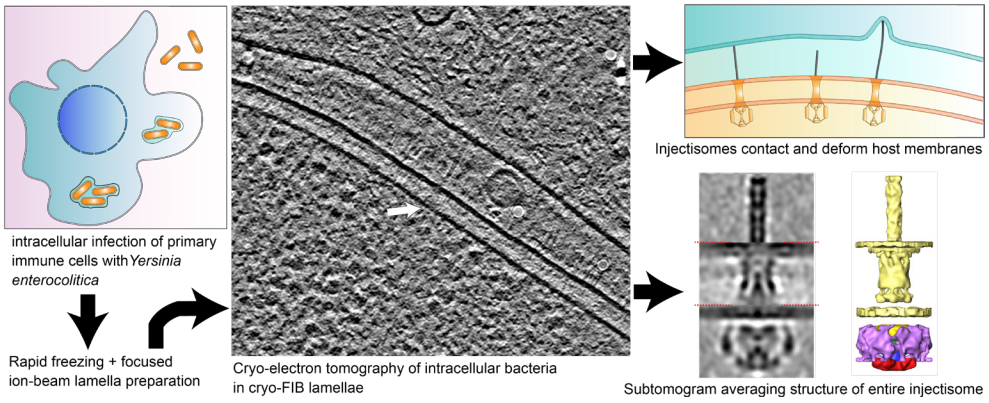

1. Introduction

The type III secretion system (T3SS), or injectisome, is a large bacterial transmembrane protein complex that transports effector proteins across both the bacterial and host membranes. These effector proteins manipulate host cells to promote favorable conditions for pathogenic bacteria. This makes the T3SS essential for virulence for many different human pathogens including *Salmonella*, *Shigella*, *Chlamydia* and *Yersinia* (Deng *et al.*, 2017). To design drugs and vaccines against these pathogens, it is important to understand their structure in the most native setting (*in situ*).

The injectisome consists of a cytosolic sorting platform in the cytoplasm, a basal body spanning the inner and outer membrane, and a needle that protrudes from the bacterium. Assembly of the injectisome (Diepold and Wagner, 2014; Deng *et al.*, 2017; Hu *et al.*, 2020) is initiated by the formation of the export apparatus and the basal body (Kimbrough and Miller, 2000; Wagner *et al.*, 2010; Kowal *et al.*, 2013). Next, the cytosolic sorting platform is formed, attached to the export apparatus and the base of the basal body (Diepold *et al.*, 2010). Subsequently, the helical needle structure is formed and elongated. When reaching the final needle length (Journet *et al.*, 2003), the sorting platform and other key proteins switch the injectisome to secreting a protein that forms the needle tip. This fully assembled T3SS will become activated upon contact with a host membrane, after which the translocon proteins are secreted to form a pore into the host cell (VanEngelenburg and Palmer, 2008; Radics *et al.*, 2014; Nauth *et al.*, 2018). Finally, several effector proteins are secreted through the needle and the pore into the host cell. The sorting platform thus needs to sequentially switch between secreting needle, needle tip, translocon and effector proteins and this process needs to be strictly regulated. The mechanisms for this regulation as well as how contact of injectisome needles with host membranes triggers the secretion of substrates are largely unknown. Determining the structural states of injectisomes in contact with host membranes (likely secreting) and not in contact to host membranes (likely non-secreting) may help to reveal these mechanisms.

The structure of the injectisome has been extensively studied by using biochemical purification followed by cryo-electron microscopy (cryo-EM) and single-particle analysis. This has been essential to determine the structure of the injectisome at resolutions allowing atomic model building (Marlovits *et al.*, 2004; Worrall *et al.*, 2016; Hu *et al.*, 2018; Lunelli *et al.*, 2020). However, purification of protein complexes from their native environment may cause parts of the complex to dissociate or change their structure. Indeed, single-particle structures of purified injectisomes lack several structural components, including the cytosolic sorting platform, the surrounding membranes and the peptidoglycan layer. Cryo-electron tomography (CET), however, can visualize protein complexes in their native environment. Structures of the injectisome of several species have been determined with CET including *Salmonella enterica*, *Shigella flexneri* and *Chlamydia trachomatis* (Kawamoto *et al.*, 2013; Hu *et al.*,

2015, 2017; Nans *et al.*, 2015; Butan *et al.*, 2019). This revealed the structure of the cytosolic sorting platform to consist of six pod-like densities, which contrast with the ring structure found in the cytosolic C-ring of the closely related bacterial flagellar motor (Thomas *et al.*, 2006; Chen *et al.*, 2011; Hu *et al.*, 2015, 2017; Makino *et al.*, 2016). The structure of the sorting platform of *Y. enterocolitica* has not yet been determined (Kudryashev *et al.*, 2013).

Because of the pivotal role of the T3SS during infection, determining different structural states of the injectisome during infection is critical to understand the mechanisms of substrate secretion. Indeed, contact with host cells has already been shown to result in structural differences in *C. trachomatis* minicells compared to a host-free state including a contraction of the basal body and stabilization of the sorting platform (Nans *et al.*, 2015). In contrast, the injectisome of *S. enterica* minicells in contact with host cells did not show any structural rearrangements (Park *et al.*, 2018). The injectisome, and in particular the sorting platform, is a highly dynamic complex, and secreting conditions have been shown to increase the exchange rate of the dynamic cytosolic injectisome subunits that form the sorting platform in *Y. enterocolitica* (Diepold *et al.*, 2015, 2017). The structural changes in the injectisome triggered by host contact in *C. trachomatis* and the altered exchange rate of sorting platform proteins observed in *Y. enterocolitica* make it likely that structural changes occur upon contact of the needle with a host membrane.

Although *Y. enterocolitica* is considered primarily an extracellular pathogen (Devenish and Schiemann, 1981; Du *et al.*, 2016), there is substantial evidence for intracellular survival and replication inside infected phagocytic myeloid cells, and *Y. enterocolitica* is known to gain entry through M cells of the gastrointestinal tract, where it can infect Peyer's patches (Tabrizi and Robins-Browne, 1992; Autenrieth and Firsching, 1996; Pujol and Bliska, 2005; VanCleave *et al.*, 2017; Bohn *et al.*, 2019). This makes myeloid cells excellent models to study injectisome structure in a biologically relevant infection context. We therefore used primary human monocytes and monocyte-derived dendritic cells to investigate with CET the injectisome structure of *Y. enterocolitica* during intracellular infection.

Whereas conventional EM sample preparation generally only allows for ultrastructural studies of host-pathogen interactions (van der Wel *et al.*, 2007), rapid freezing and cryo-microscopy preserves the molecular structure of the cell. Only the edges of mammalian cells are thin enough for electrons to penetrate to allow imaging with CET. In order to access the areas inside the cells, we used cryo–focused ion beam (cryo-FIB) to make ~200-nm-thick lamellae of the infected cells (Marko *et al.*, 2007; Schaffer *et al.*, 2017). These techniques allow protein complexes to be studied in their native environment at nanometer resolution (Bykov *et al.*, 2017; Medeiros *et al.*, 2018; Weiss *et al.*, 2019; Albert *et al.*, 2020), and enabled us to study the injectisome within infected host cells.

In this work, we visualized *Y. enterocolitica* during intracellular infection of primary myeloid cells using CET on FIB-lamellae and showed that injectisome needles directly contact, and in some cases deform, host membranes. Furthermore, we observed large variability between the contact angles of individual needles with host membranes, the lengths of the needles and lengths of the basal body. A minimal injectisome needle length seems to be required to make contact with host membranes. Finally, subtomogram averaging revealed the entire structure of the injectisome of *Y. enterocolitica* during intracellular infection, including the basal body, cytosolic sorting platform and the needle tip complex. This showed structural differences in the sorting platform compared to other species. These structural data on the injectisome structure during intracellular infection pave the way towards providing the fine molecular details of how injectisomes interact with host cells under native conditions.

2. Materials and methods

2.1 Bacterial strains and culture conditions

A starter culture of *Y. enterocolitica* AD4334 (E40 ΔblaA Δasd ΔyopH ΔyopO ΔyopP ΔyopE ΔyopM ΔyopT) SctV-mCherry was grown overnight at 28 °C in 37 g/L brain heart infusion medium (BHI) containing 35 µg/ml nalidixic acid (NAL) and 80 µg/ml diaminopimelic acid (DAP). The starter culture was used to inoculate a culture at an OD_{600} of 0.12 in 37 g/L BHI containing 35 µg/ml NAL, 80 µg/ml DAP, 0.4% glycerol (v/v) and 20 mM $MgCl_2$. Bacteria were grown for 1.5 h at 28 °C to recover exponential growth, and 3 h at 37 °C to induce the expression of the T3SS.

For confirming the identity of the extracellular protein coat as YadA, we used the strain *Yersinia enterocolitica* E40 AD4053 (E40 ΔblaA Δasd ΔyopH ΔyopO ΔyopP ΔyopE ΔyopM ΔyopT ΔyadA) where expression of YadA was prevented by the integration of the mutator plasmid pJLM4031 in the the YadA gene. These bacteria were grown as described above except with 100 µg/ml of streptomycin in the culture medium.

2.2 Monocyte isolation and differentiation

Human blood buffy coat was acquired from Sanquin, and monocytes were isolated by negative selection with RosetteSep (Stemcell Technologies) as per the manufacturer's instructions. Isolated monocytes were cultured at 37 °C and 5% CO_2 in AIM V medium (Thermo Fisher Scientific, cat. 12055083) in non-tissue culture–treated petri dishes (Greiner, ref 633179) for 1 day. The medium was replaced with AIM V medium containing 25 ng/ml interleukin-4 (IL-4) (PeproTech, cat 200-04) and 200 ng/ml granulocyte-macrophage colony-stimulating factor (GM-CSF) (PeproTech, cat 300-03), and the cells were allowed to differentiate into dendritic cells for 6 days (Hiasa *et al.*, 2009). For cryo-fluorescence microscopy, J774 macrophages were grown in RPMI 1640 medium (Thermo Fisher Scientific. Cat. 11875093) supplemented with 10% fetal bovine serum.

2.3 Infection and adhering cells to grid

Isolated monocytes or differentiated dendritic cells or J774 macrophages were washed with RPMI 1640 medium and detached by incubating for 10 min with 2 ml TripleE (Thermo Fisher Scientific cat. 12604013) followed by scraping. Then 400 000 cells were seeded in a petri dish (Greiner,ref 627160) containing 8 UltrAufoil 200-mesh R2/2 grids (Russo and Passmore, 2014), and the cells were allowed to adhere for 1 h. The cells were infected with *Y. enterocolitica* at a multiplicity of infection (MOI) of 100 for 1 h, then 10-nm gold fiducials were added. For cryo-fluorescence microscopy, an MOI of 40 was used and the nucleus was stained for 20 min with NucBlu Live ReadyProbe Reagent (Thermo Fisher, cat. R37605).

2.4 Cryo-fluorescence microscopy

Z-stacks of intra- and extracellular bacteria were imaged under cryogenic conditions with a Corrsight spinning disk confocal fluorescence microscope (Thermo Fisher Scientific) with a 40 × air objective (Zeiss, 420363-9901-000) with 405 and 561 nm excitation in spinning disk mode. Z-stacks were deconvoluted (Sage *et al.*, 2017) and max-intensity projections were made for visualization.

2.5 Jet vitrification

EM grids were vitrified with a modified Vitrobot (Thermo Fisher Scientific), where the liquid ethane–plunging container was replaced with a custom-built jet vitrification device (Ravelli *et al.*, 2020) and a force sensor on the blotting pads provides live feedback on the force that the blotting pads apply for more consistent blotting results. On the blotting pads, a sheet of Teflon was used on the sample side and Whatmann filter paper (Sigma-Aldrich, cat. no. 1001-055) on the backside of the grid. A blotting force of 2.45 N was used with a blotting time of 5 s, waiting time of 2 s, chamber humidity of 80% and temperature of 37 °C. Vitrified grids were clipped with autogrids (Thermo Fisher Scientific, cat. no. 1036173). Autogrids were modified with a laser mark pattern to orient the grid when loading it in the FIB/SEM and TEM microscopes.

2.6 Cryo-FIB lamella fabrication

For FIB lamella fabrication, a SCIOS FIB/SEM dual-beam (Thermo Fisher Scientific) was used that was upgraded to the functional equivalent of an Aquilos (Thermo Fisher Scientific). A thin layer of platinum was sputtered on the grid with the build-in sputter coater (6 s, 10 W, 600 V, 30 mA). MAPS software 3.1 (Thermo fisher Scientific) was used to acquire an overview of the grid, and sites of interest were selected and eucentric height for each position was determined. Organometallic platinum was deposed on three different sides on the edge of the grid for 3 s, and rectangular pattern milling was used to make FIB lamellae at 30 kV and a current between 0.05 and 1 nA at a milling angle of 11° relative to the grid. The initial width of the lamella was chosen between 8 and 20 µm with lower width of the milling box in consecutive milling steps. A thin layer of platinum was sputtered over the final lamellae (3 s, 10 W, 600 V, 30 mA).

2.7 Cryo-electron tomography

Most CET was done with a Tecnai Arctica (Thermo Fisher Scientific) operating at 200 kV. Data were acquired with a Falcon III direct electron detector operating in electron counting mode with a pixel size of 2.73 Å. TEM grids with lamella were oriented 90° counterclockwise in the autoloader relative to their orientation in the FIB/SEM using the laser marks. Low-dose stitched overviews of the lamellae were acquired to determine sites of interest with the MAPS software 3.6 (Thermo Fisher Scientific). Tilt series were acquired with the Tomography software 4.9 (Thermo Fisher Scientific) with a bidirectional tilt scheme between -51° and 51° with 3° increments or -34° and 34° with 2° increments with a total dose of 100 e-/Å^2. The tilt angles were corrected for the pre-tilt of the lamella. Over 150 tilt series were collected.

For the control of the YadA mutant, tilt series were recorded with a Titan Krios operating at 300 kV and equipped with a K2 operating in electron counting mode with a pixel size of 2.72 Å and a bidirectional tilt scheme between -60° and 60° with 2° increments correcting for the pre-tilt of the lamella.

2.8 Data processing and tomogram reconstruction

Dose fractions were aligned with MotionCor2 version 1.1 (Zheng *et al.*, 2017). Tilt series were aligned and reconstructed with Etomo version 4.9.5 (Mastronarde and Held, 2017) with fiducial-based local alignment, subtraction of gold fiducial markers and CTF correction by phase-flipping and reconstructed with weighted back projection. For selecting subtomograms, 4 × binned tomograms were flipped in XY and filtered with TomDeconv (https://github.com/dtegunov/tom_deconv/) (Tegunov and Cramer, 2019). For visualization and the movies, 2 × or 4 x binned weighted back projection tomograms were reconstructed from tilt series where the gold fiducials were computationally removed, and the platinum layer was computationally subtracted with Masktomrec (Fernandez *et al.*, 2016). Tomograms were flipped in XY and filtered with TomDeconv EM. Segmentation and isosurface renderings was done with Amira 4.7 (Thermo Fisher Scientific).

2.9 Subtomogram averaging

A total of 202 injectisomes were manually picked in 3DMOD (IMOD 4.9.5) (Mastronarde and Held, 2017) and Dynamo version 1.1401 (Castaño-Díez *et al.*, 2017). Particles were extracted from 2 × binned tomograms with Dynamo with a box size of 256 pixels, manually aligned with Dynamo gallery, in-plane axis rotations were randomized to reduce missing wedge artifacts, and shifts and euler angles were iteratively refined with restricted freedom. The initial reference was created by averaging the manually aligned particles. Separate masks were used to focus the alignment on the base of the needle and the basal body, or the cytosolic sorting platform and the basal body. For creating the averages during the subtomogram averaging procedure for the basal body and the cytosolic sorting platform, 141 and 101 of the particles with the highest cross-correlation score were used, respectively. C6, C3 and

C5 symmetry were applied during the last steps of the refinement procedure for the sorting platform, basal body and needle tip, respectively. These symmetry values were derived from literature (Broz *et al.*, 2007; Worrall *et al.*, 2016; Hu *et al.*, 2017) and by applying different rotational symmetries to the subtomogram average structures followed by visual inspection of orthogonal slices and visual inspection of the averages without applied symmetry.

To compare the structures of injectisomes contacting the host membranes (contact) to those that don't (non-contact), injectisomes were manually sorted into two different sets of particles and independently iteratively aligned with a mask covering the basal body. For the sorting platform, particles were averaged based on the computed alignments determined with all the particles. As a control, random sets of injectisomes with the same number of particles were used.

For the needle tip complex, 75 needle tip complexes of non-contact injectisomes were manually picked in Dynamo, extracted from 4 × binned tomograms and manually aligned with Dynamo gallery. Subtomograms from manually refined particle coordinates were extracted from 2 × binned tomograms, and in-plane axis rotations were randomized, and iterative refinement was performed in Dynamo. The initial reference was created by averaging the manually aligned particles. Forty-five particles with the highest cross-correlation score were used to create the averages during the subtomogram averaging procedure.

To determine the resolution, a Fourier-shell correlation was performed by separating the even and odd particles and independently aligning them at increasingly higher low-pass filter values. Final resolution was determined with the 0.143 criterion without symmetry and with C6, C3 and C5 symmetry for the sorting platform, basal body and needle tip, respectively.

2.10 Quantifications and statistics

For determining the basal body length, 2D slices of the aligned subtomograms were loaded into 3DMOD (IMOD version 4.9.5), and basal body length was measured with the measuring tool between the center of inner membrane to the center of the outer membrane. For measuring the length of the needles, anchor points were added to the base and the tip of the needle in dtmslice (Dynamo version 1.1401) in the tomograms, and the distance between the points was measured in 3D. An independent two-tailed, student-T test was used to compare basal body and needle lengths of injectisomes contacting the host (contact) compared to the remaining injectisomes (non-contact). The contact angle between the needle and the host membrane was measured in Fiji with the angle tool (Schindelin *et al.*, 2012; Rueden *et al.*, 2017). Local thickness of the lamella was measured with the measuring tool in 3DMOD (IMOD 4.9.5) on the reconstructed tomograms in the center of the volume (Mastronarde and Held, 2017).

3. Results

3.1 Cryo-FIB and CET workflow

To study the T3SS of *Y. enterocolitica* in an intracellular host environment, we used monocytes and dendritic cells infected with *Y. enterocolitica* AD4334. This strain is no longer pathogenic to host cells, but the injectisome can still actively secrete effector proteins (Kudryashev *et al.*, 2013; Diepold *et al.*, 2015). We established a workflow for CET on FIB-fabricated lamellae where the cryo-FIB was used to thin down the infected cells into ~200-nm slices to enable CET of the interior of cells.

We optimized grid type, blotting, freezing and FIB-milling procedures for these samples, resulting in reproducible grid and lamellae preparation (Fig. 1). Typically, several tilt-series of intracellular bacteria were acquired on a single lamella (Fig. 1B, C). To obtain sufficient contrast at high tilt angles with a cryo-TEM, it is important to have thin lamellae. We measured the local thickness in tomograms used for subtomogram averaging in this study and found an average thickness of 186 ± 58 nm (n = 63) (Fig. 1D).

Using this workflow, we acquired over 150 tomographic tilt-series of *Y. enterocolitica* inside infected monocytes and dendritic cells using a 200-kV cryo-electron microscope. Successfully establishing a reproducible cryo-FIB and CET workflow allowed us to study the *Y. enterocolitica* injectisome in an intracellular host environment at high resolution.

3.2 Y. enterocolitica in intracellular host phagosomes

In the reconstructed tomograms, *Y. enterocolitica* was present in phagosomes of host cells. The large number of bacterial ribosomes and absence of bacterial membrane deformations suggest that the bacteria are able to maintain homeostasis inside the host phagosomes (Fig. 2, Sup. Fig. 1). The surface of the bacteria was densely covered with protein stalks which extend 30 nm from the bacterial outer membrane with distal larger head groups (Fig. 2A and Sup. Movie 1). We identified this protein as the adhesion molecule YadA, which was confirmed by their absence in the YadA knockout mutant (Fig. 2B) (Hoiczyk, 2000; Koiwai *et al.*, 2016). The quality of the tomograms allows for individual trimeric ~200 kDa YadA protein complexes to be identified, which provides confidence for interpreting features of the injectisome in the tomograms.

We found injectisomes in many tomograms, characterized by the electron-dense basal body and the needle structure protruding from the outer membrane (Fig. 2C and Sup. Movie 2). The needle tip often interacts with membranes of the host. In some cases, the host membrane is deformed where the needle tip interacts with it (Fig. 2D, E). In some of the injectisomes that deform the host membrane, we also observed a small deformation of the bacterial cell envelope near the basal body (Suppl. Fig. 2). The injectisomes also appeared to cluster (Fig. 2E), as has been reported previously for *Y. enterocolitica* without host contact (Kudryashev *et al.*,

2015). We used cryo-fluorescence microscopy to visualize the distribution of the injectisome clusters during infection (Fig. 2F) and did not observe a clear preferred localization to the poles or other regions of the membrane. Additionally, we did not find any differences in the distribution of the injectisomes of intracellular compared to extracellular bacteria. This similar distribution suggests that no large changes in the localization of injectisomes clusters occur upon host cell entry.

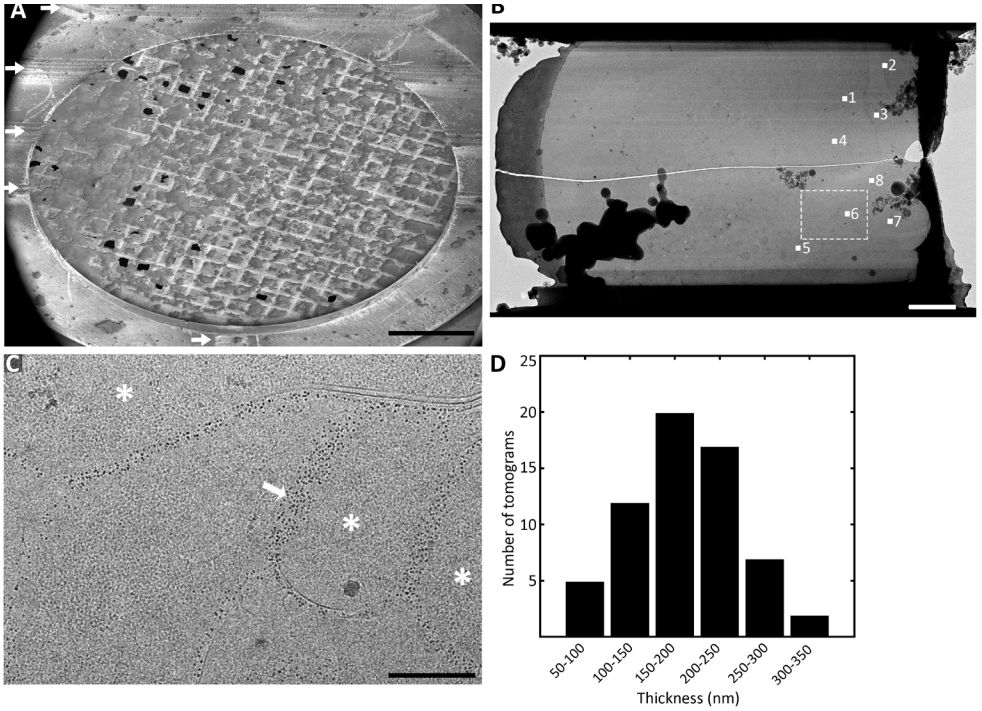

Figure 1. Overview of the cryo–electron tomography workflow on FIB-lamellae used in this study to investigate the intracellular infection of *Y. enterocolitica*. (A) Cryo-SEM overview of a sample EM-grid on which FIB-lamellae were produced followed by cryo–electron tomography. Laser marks on the autogrid are used to orient the grid in the TEM so that the lamellae are perpendicular to the tilt axis (white arrows). Scale bar: 500 µm. (B) Stitched cryo-TEM tile scan overview of FIB-lamella to determine where to record the tilt-series. Positions and order in which the tilt-series were acquired, indicated with solid white squares and numbers, respectively. The tomogram reconstructed from the tilt-series acquired at position 6 is shown in Figure 2D and E. Scale bar: 2 µm. Dashed white square shows the enlarged area in (C), in which several bacteria are visible inside the host cell (white star) surrounded by 10-nm gold beads (white arrow). Gold beads were used as fiducial markers for tilt-series alignment and were localized in the phagosomes since they were added during the infection. Scale bar: 500 nm. (D) Applying these steps resulted in reproducibly thin lamella with an average local thickness of 186 ± 58 nm (n = 63). Histogram shows the local thickness on lamella where all 63 tilt-series used for subtomogram averaging were acquired.

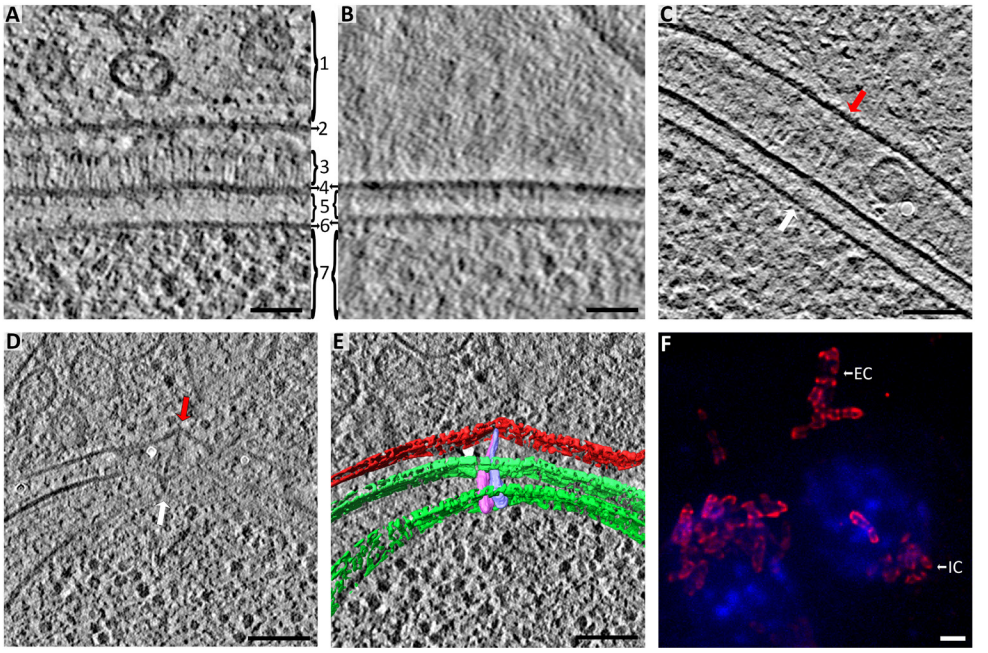

Figure 2. Injectisomes of *Y. enterocolitica* during intracellular infection deform host membranes. (A) We observed that *Y. enterocolitica* AD4334 is densely covered in the trimeric ~200 kD autotransporter YadA (3), which extends 30 nm from the outer membrane. The bacterial outer membrane was not observed to come into contact to the phagosomal membrane and a gap of around 30 nm or greater was observed between the two. From top to bottom: 1 – host cytosol, 2 – phagosomal membrane, 3 – YadA, 4 – bacterial outer membrane, 5 – periplasm, 6 – bacterial inner membrane, 7 – bacterial cytosol. Scale bar: 50 nm. (B) The identity of the YadA proteins was confirmed with the *Y. enterocolitica* AD4053 strain, which does not express YadA. YadA has been observed on the outside of *Y. enterocolitica* previously (Hoiczyk, 2000) and its size and appearance are consistent with its structure (Koretke *et al.*, 2006). Scale bar: 50 nm. (C) Intracellular injectisome needle of *Y. enterocolitica* interacting with the phagosomal membrane (red arrow) of the host. The injectisome is indicated by a white arrow. Scale bar: 100 nm. (D) Deformation of the host phagosomal membrane (red arrow), presumably by the injectisome needle. The injectisome is indicated by a white arrow. Scale bar: 100 nm. (E) Segmentation of the tomographic volume of panel D with the injectisome visible in panel D shown in pink and an injectisome from another tomographic slice in purple. The host phagosomal membrane (red) is deformed where the needles interact with it. Scale bar: 100 nm. (F) Cryo-fluorescence image of *Y. enterocolitica* during intracellular infection (nucleus in blue) with the injectisome export apparatus protein SctV labeled with the fluorescent protein mCherry (red). Scale bar: 3 µm.

3.3 Structural heterogeneity of injectisomes

Since contact to host cells is known to promote secretion of T3SS effector proteins (VanEngelenburg and Palmer, 2008; Radics *et al.*, 2014; Nauth *et al.*, 2018), injectisomes where the needle tip contacts the host membrane are likely to be actively secreting. We therefore in this study compared injectisomes contacting the host membrane, and likely to be actively secreting (referred to as contact injectisomes), to injectisomes where the needle does not contact the host membrane, which are likely to be in a non-secreting state (referred to as non-contact injectisomes) (Fig. 3A).

To characterize the injectisomes *in situ* in more detail, we measured their different components, including the contact angles of injectisome needles to the host membranes as well as the lengths of the needles and basal bodies. Most needles interacted with the host membrane at angles close to 90 degrees, but also many needles interacted at more shallow angles (Fig. 3B). We observed contact angles between 40°-90°, except for one injectisome that contacts a host vesicle (or tubular invagination) at a very shallow angle (Suppl. Fig. 3.) We did not observe any needle structures protruding across the membranes, indicating piercing. The length of injectisome needles was highly variable between 11 and 171 nm (Fig. 3C). To determine whether needle length was related to interaction with the host membrane, we compared the needle lengths between contact and non-contact injectisomes. A longer mean needle length of 69 ± 25 nm was found for contact injectisomes (n = 62) compared to a mean needle length of 61 ± 31 nm for non-contact injectisomes (n = 102) (P = 0.08) (Fig. 3C). Non-contact injectisomes showed greater frequency of short (<30 nm) needles, of 12% (12 of 102) needles compared to only 3% (2 of 62) of contact injectisomes with short needles. The minimal distance between the bacterium and the phagosomal membrane is observed to be around 30 nm, which likely explains why short needles are very unlikely to bridge this gap. A minimal needle length to make host contact thus seems to be required for intracellular injectisome attachment.

Next, we measured the basal body length of all injectisomes and compared them between contact and non-contact injectisomes (Fig. 3D, Sup. Fig. 4). We found slightly but significantly longer basal bodies for contact injectisomes (31.4 ± 2.3 nm; n = 56) compared to non-contact injectisomes (30.6 ± 2.3 nm; n = 125) injectisomes (two-tailed student T-test where P = 0.04). The basal body length of the injectisomes was variable, as has previously been reported for the length of the basal body of *Y. enterocolitica* without host contact in minicells (Kudryashev *et al.*, 2013).

In summary, we observed that not all needle complexes interact with the host membrane, contact angles of the needles with the host are variable and that injectisome needles can deform host membranes at their contact sites. Furthermore, we also found wide variation (11 to 171 nm) in the lengths of the injectisome needles and that a minimal needle length of ~30 nm is required to contact the host membranes. Together, these data show that the T3SS of *Y. enterocolitica* during intracellular infection is heterogeneous.

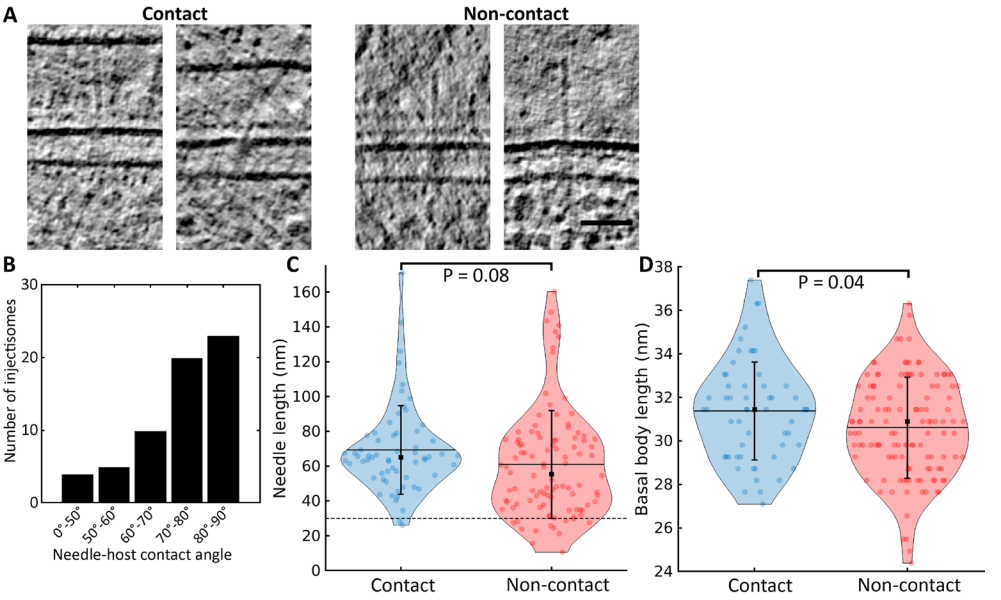

Figure 3. Comparison of contact and non-contact injectisomes. (A) Tomographic slices showing individual injectisomes with the needle interacting with host membranes (contact) and injectisomes where the needle does not interact with host membranes (non-contact). In total, we identified 202 injectisomes, of which 122 were facing host membranes and could therefore potentially interact with it. Of these, 62 needle tips were found to interact with the host membrane. We observed large and more moderate deformations of the host membrane at seven needle–host contact sites. The needles of non-contact injectisomes were either facing another bacterium, facing the host but not making contact with it, did not have a needle or the needle tip was outside of the tomographic volume. Scale bar: 50 nm. (B) Histogram depicting the contact angles of the injectisome needles (n = 62) with the phagosomal membrane. (C) Violin plot comparing the distribution of the needle length of contact injectisomes (blue; mean ± SD; 69 ± 25 nm; n = 62) compared to non-contact injectisomes (red; mean ± SD; 61 ± 31 nm; n = 102). We compared the difference in needle length with a two-tailed student T-test (P = 0.08). Black horizontal lines indicate the mean and black squares the median. Error bars indicate the standard deviation from the mean. Dashed black line indicates the 30 nm minimal needle length required for host membrane contact. Of the total 202 injectisomes, we found 35 where no needle could be observed and two injectisomes where we could see a needle but could not measure its total length because it was not fully contained in the tomographic volume. (D) Violin plot showing the distribution of basal body length of contact (blue) and non-contact (red) injectisomes. Black horizontal lines indicate the mean and black dots the median. Error bars indicate the standard deviation from the mean. The average basal body length of contact injectisomes (mean ± SD; 31.4 ± 2.3 nm; n = 56) is significantly longer than non-contact injectisomes (mean ± SD; 30.6 ± 2.3 nm; n = 125) (two-tailed student T-test where P = 0.04).

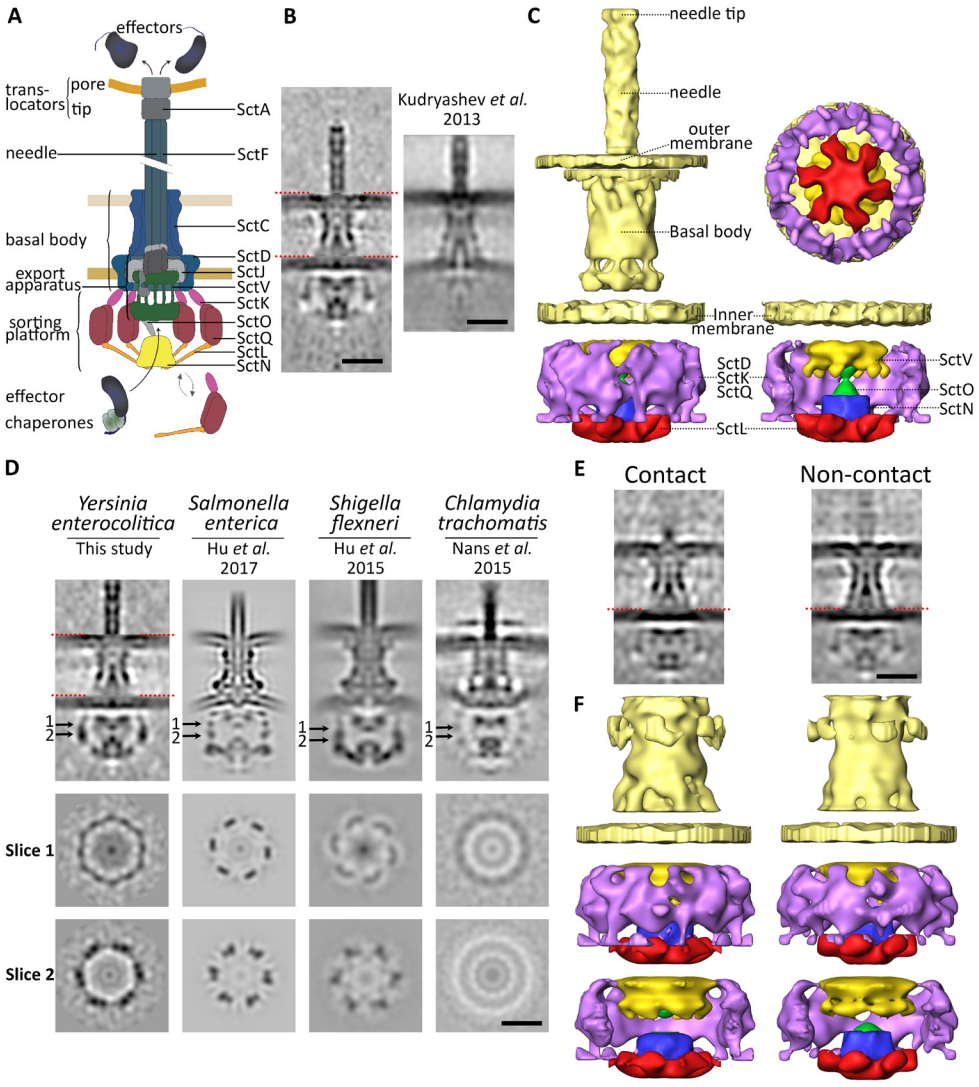

Figure 4. Subtomogram averaging structures of the injectisome of *Y. enterocolitica* during intracellular infection of host cells. (A) Schematic overview of the main components of the injectisome (left) and the proteins (right). The basal body consists of ring structures formed by SctD and SctJ close to the inner membrane and of the secretin SctC near the outer membrane. The export apparatus spans the inner membrane into the cytosol and consists of 5 proteins including SctV (Kuhlen *et al.*, 2018). The N-terminus of SctD extends through the inner membrane on the outside of the complex and connects via SctK to SctQ, which in turn is bound to SctL, which forms six "spokes" consisting of dimers. Directly above SctL on the inside of the sorting platform are the ATPase SctN and the stalk protein SctO. The helical needle consists of the needle protein SctF and is capped by the needle tip protein SctA. Unfolded effector proteins are secreted through the hollow needle via a pore complex formed by the translocon proteins into host cells (VanEngelenburg and Palmer, 2008; Radics *et al.*, 2014; Nauth *et al.*, 2018). Adapted from (Wimmi *et al.*, 2020 Preprint). (B) Longitudinal slice of the subtomogram averages of the injectisome of *Y. enterocolitica*. The sorting platform, basal body and needle tips were aligned separately (Sup. Fig. 5A–F) and the averages were joined (red dashed lines). Right panel: central slice of the subtomogram average previously determined in *Y. enterocolitica* (EMD 5694, (Kudryashev *et al.*, 2013)) scaled to the average determined in this study.

Scale bars: 20 nm. (C) Isosurface rendering of the average of the sorting platform with the different proteins indicated in different colors as a model for the *Y. enterocolitica* injectisome sorting platform. Right panel: bottom view of the sorting platform (top) and the sorting platform with a part of the SctQ-SctK-SctD complex removed. (D) Comparison of subtomogram average structures of different species. Density maps from The Electron Microscopy Databank were low-pass filtered to 4-nm resolution and scaled to the subtomogram average from this study. From left to right: *Y. enterocolitica* (composed of EMD-11905, EMD-11906, EMD-11907, this publication), enterica (EMD-8544, (Hu *et al.*, 2017)), *S. flexneri* (EMD-2667, (Hu *et al.*, 2015)) and *C. trachomatis* (EMD-3217, (Nans *et al.*, 2015)). Arrows indicate positions of different orthogonal slices shown in the bottom panels. Scale bar: 20 nm. For *Y. enterocolitica*, separate subtomogram averages of the sorting platform, basal body and needle were joined together (red dashed lines). (E) Comparison of the structure of contact and non-contact injectisomes by subtomogram averages of contact injectisomes (left) and non-contact injectisomes (right) low-pass filtered to a resolution of 5 nm. The averages focused on the basal body were independently aligned and the averages for the sorting platform were created from averaging the particles based on alignments from the global average. The two subtomogram averages were joined together (red dashed line). Scale bar: 20 nm. (F) Isosurface renderings of the contact (left) and non-contact (right) injectisome structure shown in E. bottom panel: the sorting platforms with part of the SctQ-SctK-SctD complex removed.

3.4 Structure of the injectisome during infection

To determine the structure of the injectisome in an intracellular infection context, we performed subtomogram averaging (Fig. 4B, Sup. Movie 3). Because of the high flexibility in the length of the basal body, the sorting platform and the upper part of the basal body were aligned independently with different masks (Sup. Fig. 5). A similar approach has been used previously for the type III and IV secretion systems (Kudryashev *et al.*, 2013; Nans *et al.*, 2015; Ghosal *et al.*, 2017). We also separately picked the needle tips of non-contact injectisomes because of their variable lengths and angles. (Mueller *et al.*, 2005; Broz *et al.*, 2007). Subtomogram averaging of the needle tips of contact injectisomes did not result in stable averages because of the variable needle-membrane contact angles combined with the low number of particles (data not shown).

We applied C3 and C6 rotational symmetry to the basal body and sorting platform respectively, based on the known structure of the T3SS in *Salmonella* and *Shigella* (Worrall *et al.*, 2016; Hu *et al.*, 2017). It is likely that the *Yersinia* injectisome share this rotational symmetry considering the conserved interactions of proteins within the sorting platform (Jackson, 2000; Johnson and Blocker, 2008) and the shared stoichiometry between these species (Diepold *et al.*, 2017; Zhang *et al.*, 2017). For the needle tip, we applied C5 rotational symmetry, which has previously been determined for *Y. enterocolitica* (Mueller *et al.*, 2005; Broz *et al.*, 2007). The final resolutions determined by Fourier shell correlation between independently processed half-sets was 3.3 nm for the basal body, 4.0 nm for the sorting platform and 3.9 nm for the needle tip with their respective symmetry values applied (Sup. Fig. 5).

Our structure of the basal body was similar to that determined from minicells without host contact (Kudryashev *et al.*, 2013) (Fig. 4B). Based on the homology of the sorting platform proteins between T3SS, we assigned the sorting platform proteins to the measured electron densities based on the work of Hu *et al.* in *S. enterica* where they used mutants to confirm the identity of the components of the sorting platform (Hu *et al.*, 2017) (Fig. 4A, C, D). In this

model, SctD, SctK and SctQ form a 6-fold rotationally symmetric interconnected structure on the outside of the sorting platform. SctQ connects to SctL, which forms a structure with six “spokes”. Just above the SctL on the inside of the sorting platform is the ATPase SctN, which connects to the stalk protein SctO that is connected to export apparatus protein SctV.

We compared our subtomogram average structure of the injectisome to those from other species and found them to be overall similar (Fig. 4D) (Hu *et al.*, 2015, 2017; Nans *et al.*, 2015), but also observed clear differences in the sorting platform. The diameter is conserved between all species (~29 nm), but the overall shape of the sorting platform is more rounded at the bottom for *Y. enterocolitica*, which appears to be caused by the bowl-shape formed by the SctL hexamer of dimers, whereas SctL forms a flatter structure in *S. enterica* and *S. flexneri*. Additionally, in our structure, the SctQ-SctK-SctD complex appears to form an interconnected, almost ring-like structure whereas for *S. enterica* and *S. flexneri* they form six distinct pods that are only connected by the cytosolic domains of SctD and to SctL distal from the inner membrane (Hu *et al.*, 2015, 2017).

To determine whether substrate switching triggered by host contact results in structural changes in the injectisome, we created separate averages for contact and non-contact injectisomes focused on the basal body and the sorting platform (Fig. 4E, F) and as a control also for random sets of particles (Sup. Fig. 6). Based on the variations observed in the random control, we conclude that no significant structural rearrangements could be observed in injectisomes in contact with the host membrane.

4. Discussion

Here we used CET on FIB-lamellae to visualize *Y. enterocolitica* during intracellular infection of myeloid cells (Fig. 1). We show that the injectisome needles can directly contact host membranes, which can result in a deformation of the host membrane (Fig. 2). We observed large heterogeneity in contact angles with the host, basal body and needle lengths of individual injectisomes, but found that needles of contact injectisomes to be elongated compared to non-contact injectisomes (Fig. 3). Finally, we determined the entire structure of the injectisomes of *Y. enterocolitica*, including the cytosolic sorting platform, inside infected monocytes and dendritic cells by using subtomogram averaging on tomograms recorded on thin cryo-FIB lamellae and found no clear structural differences in injectisomes in contact to host membranes compared to those that are not (Fig. 4).

Our observations of some *Y. enterocolitica* injectisomes deforming the host membrane and small deformations of the bacterial outer membrane (Fig. 2D, E, Sup. Fig. 2) have also been observed for *S. enterica* (Park *et al.*, 2018). This deformation of the bacterial envelope may suggest that a mechanical force is applied by the needle that results in a deformation of both host and bacterial membranes. Binding of adhesion proteins to host membranes has been hypothesized to provide this force by pulling closer the bacterium to enable the injectisome to contact the host (Park *et al.*, 2018; Bohn *et al.*, 2019). This hypothesis is supported by several studies that show a dependence of T3SS function on the bacterial adhesins YadA and Inv (Mota *et al.*, 2005; Keller *et al.*, 2015; Deuschle *et al.*, 2016). However, we did not see direct interactions between the adhesion YadA and the phagosomal host membranes during intracellular infection, which may suggest that the main role of YadA in relation to T3SS function is extracellular (Keller *et al.*, 2015). Whether deformation of host membranes is required for insertion of the translocon and/or effective secretion of effector proteins into the host cell remains to be determined. The membrane deformations may also be temporary, which could explain why they were only observed in 7 out of 62 contact injectisomes.

The contact angles of the injectisomes we measured for *Y. enterocolitica* during intracellular infection were more heterogeneous than those reported for *S. enterica*.

We observed heterogeneous contact angles between 0°–90° with over 60% of the injectisomes with contact angles of 80° or lower whereas most needle–host contact angles for *S. enterica* were reported to be close to perpendicular for wildtype bacteria, but not for mutants lacking the pore complex protein SctE or the needle tip protein SctA (Park *et al.*, 2018). What is currently unknown is whether the contact angles remain static or whether they may change over time. Prolonged needle–host contact in a dynamic environment may create more variable contact angles over time.

In addition to the varied contact angles, we also found large variability in the injectisome needle lengths during intracellular infection. In previous studies on isolated needles from bacteria without host contact, similar mean values for needle lengths were found, but the range and variability were smaller compared to this study (Journet *et al.*, 2003; Wagner *et al.*, 2009). Our observed increased range and variability in needle length compared to previous studies without an infection context host may suggest that SctP, which regulates the needle length (Journet *et al.*, 2003), may be less stringent during intracellular infection to optimize needle length locally to the variable distance of the bacterium to the phagosomal membrane. The observed minimal needle length of ~30 nm for injectisomes in contact to the host membrane is likely because shorter needles cannot bridge the >30 nm distance between the bacteria and the host. We measured a small, but statistically significant elongation of the basal body of contact injectisomes compared to non-contact. We did not observe this elongation when comparing the structure of contact and non-contact injectisomes with subtomogram averaging. The <1 nm increase in basal body length we found by measuring the heights of individual injectisomes is slightly larger than one pixel, which may explain the lack of visible differences in the averaged structures. A contraction of the basal body has previously been observed in *C. trachomatis* in contact injectisomes (Nans *et al.*, 2015).

We determined the structure of the entire injectisome, including the cytosolic sorting platform in the context of the host cell. The sorting platform has only recently been structurally characterized because biochemical isolation disrupts its structure, and has previously not been visualized for *Yersinia*. We compared our subtomogram average structure to other species (Fig. 4D) and found that in *Y. enterocolitica* the SctQ-SctK-SctD complex appears to form an interconnected ring-like structure, which contrasts with the six pods identified in *S. enterica* and *S. flexneri*, which are only connected by the cytosolic domains of SctD and to SctL distal from the inner membrane (Hu *et al.*, 2015, 2017). A higher resolution structure in future studies may further confirm these structural differences in the SctQ-SctK-SctD complex between *Y. enterocolitica* and other species and may also allow for molecular docking to determine which proteins and in which copy numbers form this ring-like density. Since SctQ-SctK-SctD and their orthologues in *S. enterica* have a similar molecular weight compared to *Y. enterocolitica*, this is unlikely to cause the formation of a ring-like structure rather than pod-like densities. The presence of additional proteins could better explain this difference. Studies using fluorescence light microscopy show ~22–24 copies of SctQ per injectisome in *Y. enterocolitica* and *S. enterica* (Diepold *et al.*, 2015; Zhang *et al.*, 2017) whereas 12 copies of SctQ per sorting platform best fit the models based on a SAXS-structure of reconstituted sorting platforms and subtomogram averaging in *S. enterica* minicells (Hu *et al.*, 2017; Bernal *et al.*, 2019). One explanation for the extra densities could be that there are 24 SctQ proteins per sorting platform in *Y. enterocolitica* during the conditions present in this study, with 4 SctQ proteins per "spoke" of the ring. Another possibility could be the presence of SctQc, the C-terminus of SctQ expressed as a distinct protein (Yu *et al.*, 2011; Bzymek *et*

al., 2012). SctQc binds in dimers to full-length SctQ (Bzymek *et al.*, 2012; McDowell *et al.*, 2016) and SctQc dimers bind to SctQ, SctL and SctN in a reconstituted system from isolated and overexpressed protein in solution (Bernal *et al.*, 2019). Moreover, SctQc has been shown to be in close proximity of injectisomes of *Y. enterocolitica* with a similar turnover as full-length SctQ (Diepold *et al.*, 2015). A recent study reported that the C-terminal fragment of SctQ is not a structural protein of the T3SS of *S. enterica* in minicells without host contact (Lara-Tejero *et al.*, 2019), which may reflect differences between species and/or host contact.

Whether the structural difference we observed are caused by the presence of the host or due to the differences of T3SSs between these species also remains to be determined, but the absence of structural differences observed in *S. enterica* in host contact compared to without host contact suggest a difference between the species (Hu *et al.*, 2017; Park *et al.*, 2018). Functionally, this structural difference may reflect differences in regulation of substrate secretion required for infecting different hosts and cell types.

When comparing the C-ring of the injectisome to the C-ring of the flagellar motor complex, the diameter of the injectisome C-ring appears to be conserved between species (~29 nm) whereas large variability in the diameter of the C-ring (34–57 nm) has been observed between different species (Rossmann and Beeby, 2018). This difference in variability in the C-ring structure is likely a reflection of its function; the flagellar C-ring's acts as a rotor to transmit torque to the central axial drive shaft for bacteria that live in surroundings with a different viscosity whereas the C-ring of the injectisome is involved in regulating substrate export into host cells. More subtle structural variations may be sufficient for optimal injectisome function in bacteria with different host and tissue tropisms.

It is striking that the inner membrane of previously published subtomogram averaging structures of *S. enterica*, *S. flexneri* and *Y. enterocolitica* have a strong inward curvature (Kudryashev *et al.*, 2013; Hu *et al.*, 2015, 2017), whereas the subtomogram averages in this study show an inner membrane that is nearly flat. We believe that this difference is the result of the use of minicells, which are primarily used in the previously reported T3SS structures. In contrast, in this study we used regular-sized bacteria, which are larger and have a lower membrane curvature on most of their surface.

Our finding that the structures of contact and non-contact injectisomes by subtomogram averaging did not harbor major differences is interesting. This suggests that no large structural rearrangements are triggered upon contacting the host membrane. However, it is still likely that assembled injectisomes can exist in multiple structural states, with small structural differences, considering that when the needle contacts host membranes, a signal needs to be transmitted to the export apparatus and sorting platform to initiate substrate switching. Structural rearrangements in the sorting platform could help regulate this process by allowing different chaperone-bound substrates to bind to initiate secretion (Deng *et al.*, 2017). Also the

dynamic turnover of proteins of the injectisomes and structural differences observed during host contact with CET support the existence of multiple structural states (Diepold *et al.*, 2015, 2017; Nans *et al.*, 2015). Classification of injectisomes into multiple conformational intermediates at a higher resolution could reveal these small structural differences in the context of the host cell, giving insights into the detailed mechanism of the injectisome function. This may become feasible in the near future, considering the rapid development in the CET field in throughput and resolution (O'Reilly *et al.*, 2020; Zachs *et al.*, 2020).

In conclusion, this work presents the first structure of the entire *Y. enterocolitica* injectisome in host cell phagosomes, revealing structural differences in the sorting platform compared to other species. The absence of large structural differences between injectisomes in contact with host membranes and injectisomes not in contact to host membranes suggests that activation by host contact does not trigger large structural rearrangements in the injectisome. This is an important step towards understanding how the T3SS of *Y. enterocolitica* functions *in situ* in intracellular infection in host cells. Studying the injectisome intracellularly with CET was enabled by employing cryo-FIB to prepare thin lamellae of infected cells. This method may be used to study intracellular host–pathogen interactions and the different structural states of protein complexes in their native cellular context to bridge the gap between structural and cell biology.

Appendices and supplementary information

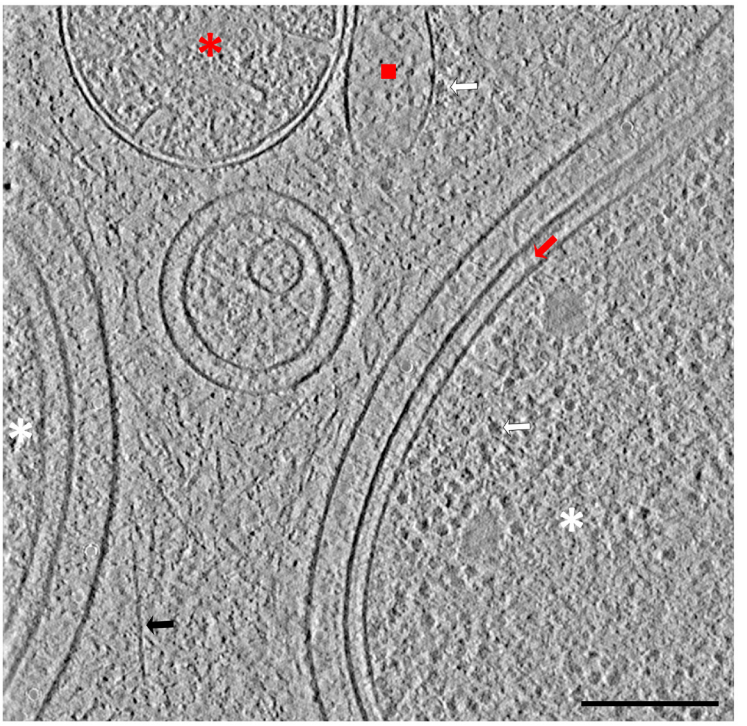

Supplementary Figure 1. Tomogram of intracellular *Y. enterocolitica* (white stars) inside the phagosomal membrane of the host. We observed a large number of ribosomes (white arrow) and no deformations of the bacterial membrane, which suggests that the bacteria are able to maintain homeostasis inside the host phagosomes. An injectisome can be observed in the bacterial membrane (red arrow). In the cytosol of the host cell, several organelles can be observed including a mitochondrion (red star) and rough endoplasmic reticulum (red square) covered in ribosomes (white arrow). Many actin filaments can be observed in the cytosol as well (black arrow). Scale bar: 200 nm.

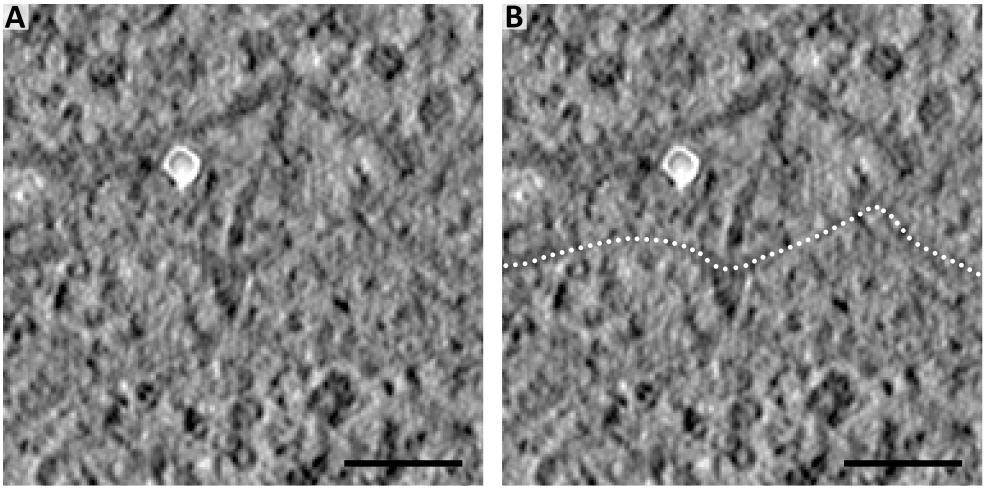

Supplementary Figure 2. (A) Enlarged area of the tomographic slice shown in Fig. 2D showing how the bacterial membrane is locally deformed near the basal body of the injectisome. Bacterial outer membrane indicated in white dashed line in panel B. Scalebar: 50 nm.

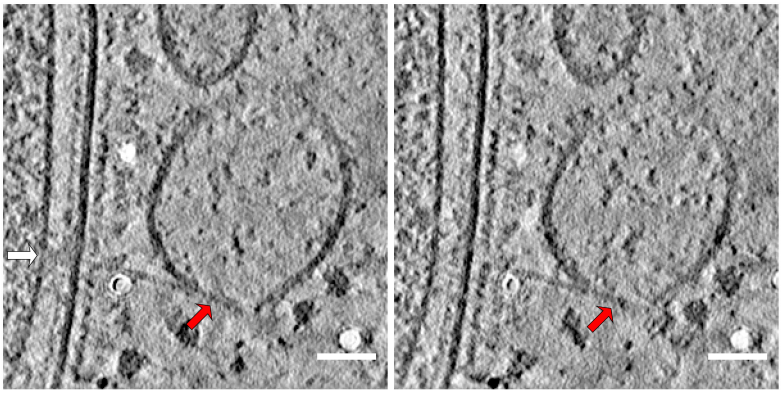

Supplementary Figure 3. Tomographic slices showing an injectisome (basal body indicated with white arrow) that contacts the membrane of a host vesicle or invagination of the phagosomal membrane with the needle at a very shallow angle (red arrow). Scalebar: 50 nm.

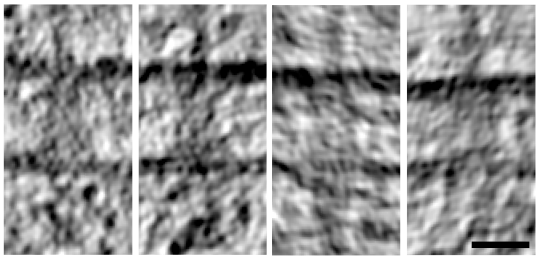

Supplementary Figure 4. Tomographic slices of individual injectisomes with variable basal body lengths. Scale bar: 20 nm and applies to all panels.

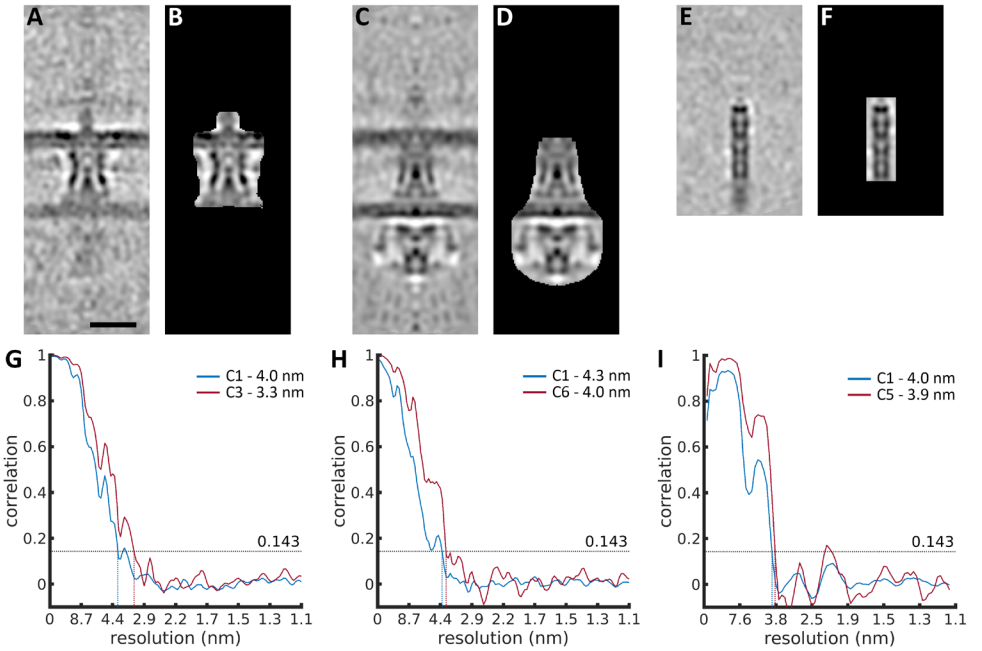

Supplementary Figure 5. Masks and resolution used during subtomogram averaging. Independent subtomogram averages of the basal body (A), sorting platform (C) and the needle tip (E) used to create Fig. 3A. Scale bar: 20 nm and applies to A-F. (B, D, F) Masks used to align the basal body, sorting platform and the needle tip, respectively. (G, H, I) Fourier shell correlation plots of the averages of the basal body, sorting platform and needle tip, respectively. Blue lines indicate the Fourier shell correlation without any symmetry applied and the red lines, the correlation with their respective rotational symmetries applied. The symmetry values were determined primarily based on published works (Mueller *et al.*, 2005; Broz *et al.*, 2007; Worrall *et al.*, 2016; Hu *et al.*, 2017). The final resolution based on the 0.143 criterion without applying symmetry for the basal body, sorting platform and needle tip was determined to be 4.0 nm, 4.3 nm and 4.0 nm, respectively, and with their respective symmetry to be 3.3 nm, 4.0 nm and 3.9 nm.

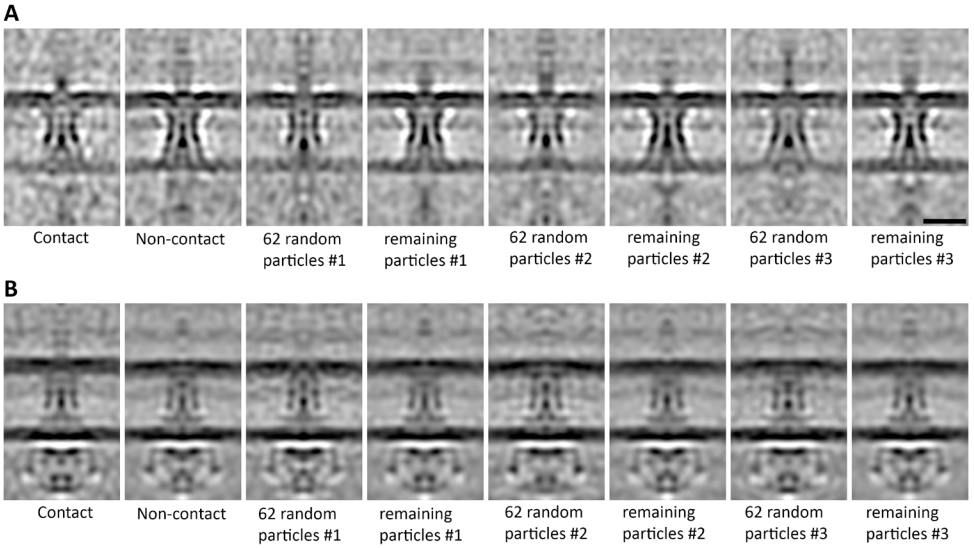

Supplementary Figure 6. Structural comparison of contact and non-contact injectisomes with subtomogram averaging. (A) Independent alignment of contact and non-contact injectisomes. As a control, three random sets of particles with the same number (62) as the host contact group (random particles #1-3) and three sets with the remaining particles were also independently aligned. Scale bar: 20 nm and applies to all images. (B) Averages created from the same groups as in A based on the particle orientations determined in the subtomogram averaging alignment with all the particles with a mask covering the sorting platform and lower part of the basal body.

Supplementary Movie 1. Movie of the tomogram displayed in Fig. 2A showing the 3-dimensional distribution of the bacterial adhesin YadA on the surface of *Y. enterocolitica* during intracellular infection. Scale bar: 200 nm.

Supplementary Movie 2. Movie of the tomogram shown in Fig. 2C. Injectisomes contacting the host membrane are annotated with white arrows. Scale bar: 100 nm.

Supplementary Movie 3. Movie of the combined subtomogram average of the sorting platform, basal body and needle shown in Fig. 3D. Black line indicates the slice shown on the right. Scale bar: 20 nm.

Accession numbers

The subtomogram averages of the sorting platform, basal body and the needle have been deposited in the Electron Microscopy Database with accession numbers: EMD-11905 (sorting platform), EMD-11906 (basal body) EMD-11907 (needle).

CRediT authorship contribution statement

Casper Berger: conceptualization, investigation, Writing - Original Draft. Raimond Ravelli: writing – review & editing. Carmen López-Iglesias: writing – review & editing. M. Kudryashev: writing – review & editing. A. Diepold: conceptualization, writing – review & editing. Peter Peters: conceptualization, writing – review & editing.

Acknowledgements

We thank the Microscopy CORE Lab members for their technical and logistics support and we thank Hang Nguyen, Navya Premaraj and Nynke van Polanen for critical reading of the manuscript. We also thank Ruud Schampers and Thomas Hoffman for their technical assistance with data acquisition with the Titan Krios at The Netherlands Centre for Electron Nanoscopy.

Funding

The UM acknowledge co-funding by the PPP Allowance made available by Health~Holland, Top Sector Life Sciences & Health, to stimulate public-private partnerships, under project number LHSM18067, as well as from the Netherlands Organisation for Scientific Research (NWO) in the framework of the National Roadmap NEMI project number 184.034.014. Misha Kudryashev is supported by the Sofja Kovalevskaja Award from the Alexander von Humbold Foundation.

References

Albert, S., Wietrzynski, W., Lee, C.-W., Schaffer, M., Beck, F., Schuller, J.M., Salomé, P.A., Plitzko, J.M., Baumeister, W., Engel, B.D., 2020. Direct visualization of degradation microcompartments at the ER membrane. Proc. Natl. Acad. Sci. 117, 1069–1080. https://doi.org/10.1073/pnas.1905641117

Autenrieth, I.B., Firsching, R., 1996. Penetration of M cells and destruction of Peyer's patches by *Yersinia enterocolitica*: an ultrastructural and histological study. J. Med. Microbiol. 44, 285–294. https://doi.org/10.1099/00222615-44-4-285

Bernal, I., Börnicke, J., Heidemann, J., Svergun, D., Horstmann, J.A., Erhardt, M., Tuukkanen, A., Uetrecht, C., Kolbe, M., 2019. Molecular Organization of Soluble Type III Secretion System Sorting Platform Complexes. J. Mol. Biol. 431, 3787–3803. https://doi.org/10.1016/j.jmb.2019.07.004

Bohn, E., Sonnabend, M., Klein, K., Autenrieth, I.B., 2019. Bacterial adhesion and host cell factors leading to effector protein injection by type III secretion system. Int. J. Med. Microbiol. 309, 344–350. https://doi.org/10.1016/j.ijmm.2019.05.008

Broz, P., Mueller, C.A., Müller, S.A., Philippsen, A., Sorg, I., Engel, A., Cornelis, G.R., 2007. Function and molecular architecture of the *Yersinia* injectisome tip complex. Mol. Microbiol. 65, 1311–1320. https://doi.org/10.1111/j.1365-2958.2007.05871.x

Butan, C., Lara-Tejero, M., Li, W., Liu, J., Galán, J.E., 2019. High-resolution view of the type III secretion export apparatus *in situ* reveals membrane remodeling and a secretion pathway. Proc. Natl. Acad. Sci. 116, 24786–24795. https://doi.org/10.1073/pnas.1916331116

Bykov, Y.S., Schaffer, M., Dodonova, S.O., Albert, S., Plitzko, J.M., Baumeister, W., Engel, B.D., Briggs, J.A., 2017. The structure of the COPI coat determined within the cell. Elife 6, e32493. https://doi.org/10.7554/eLife.32493

Bzymek, K.P., Hamaoka, B.Y., Ghosh, P., 2012. Two Translation Products of *Yersinia* yscQ Assemble To Form a Complex Essential to Type III Secretion. Biochemistry 51, 1669–1677. https://doi.org/10.1021/bi201792p

Castaño-Díez, D., Kudryashev, M., Stahlberg, H., 2017. Dynamo Catalogue: Geometrical tools and data management for particle picking in subtomogram averaging of cryo-electron tomograms. J. Struct. Biol. 197, 135–144. https://doi.org/10.1016/j.jsb.2016.06.005

Chen, S., Beeby, M., Murphy, G.E., Leadbetter, J.R., Hendrixson, D.R., Briegel, A., Li, Z., Shi, J., Tocheva, E.I., Müller, A., Dobro, M.J., Jensen, G.J., 2011. Structural diversity of bacterial flagellar motors. EMBO J. 30, 2972–2981. https://doi.org/10.1038/emboj.2011.186

Deng, W., Marshall, N.C., Rowland, J.L., McCoy, J.M., Worrall, L.J., Santos, A.S., Strynadka, N.C.J., Finlay, B.B., 2017. Assembly, structure, function and regulation of type III secretion systems. Nat. Rev. Microbiol. 15, 323–337. https://doi.org/10.1038/nrmicro.2017.20

Deuschle, E., Keller, B., Siegfried, A., Manncke, B., Spaeth, T., Köberle, M., Drechsler-Hake, D., Reber, J., Böttcher, R.T., Autenrieth, S.E., Autenrieth, I.B., Bohn, E., Schütz, M., 2016. Role of β1 integrins and bacterial adhesins for Yop injection into leukocytes in *Yersinia enterocolitica* systemic mouse infection. Int. J. Med. Microbiol. 306, 77–88. https://doi.org/10.1016/j.ijmm.2015.12.001

Devenish, J.A., Schiemann, D.A., 1981. HeLa cell infection by *Yersinia enterocolitica*: evidence for lack of intracellular multiplication and development of a new procedure for quantitative expression of infectivity. Infect. Immun. 32, 48–55. https://doi.org/10.1128/IAI.32.1.48-55.1981

Diepold, A., Amstutz, M., Abel, S., Sorg, I., Jenal, U., Cornelis, G.R., 2010. Deciphering the assembly of the *Yersinia* type III secretion injectisome. EMBO J. 29, 1928–1940. https://doi.org/10.1038/

emboj.2010.84
Diepold, A., Kudryashev, M., Delalez, N.J., Berry, R.M., Armitage, J.P., 2015. Composition, Formation, and Regulation of the Cytosolic C-ring, a Dynamic Component of the Type III Secretion Injectisome. PLOS Biol. 13, e1002039. https://doi.org/10.1371/journal.pbio.1002039
Diepold, A., Sezgin, E., Huseyin, M., Mortimer, T., Eggeling, C., Armitage, J.P., 2017. A dynamic and adaptive network of cytosolic interactions governs protein export by the T3SS injectisome. Nat. Commun. 8, 15940. https://doi.org/10.1038/ncomms15940
Diepold, A., Wagner, S., 2014. Assembly of the bacterial type III secretion machinery. FEMS Microbiol. Rev. 38, 802–822. https://doi.org/10.1111/1574-6976.12061
Du, J., Reeves, A.Z., Klein, J.A., Twedt, D.J., Knodler, L.A., Lesser, C.F., 2016. The type III secretion system apparatus determines the intracellular niche of bacterial pathogens. Proc. Natl. Acad. Sci. 113, 4794–4799. https://doi.org/10.1073/pnas.1520699113
Fernandez, J.-J., Laugks, U., Schaffer, M., Bäuerlein, F.J.B., Khoshouei, M., Baumeister, W., Lucic, V., 2016. Removing Contamination-Induced Reconstruction Artifacts from Cryo-electron Tomograms. Biophys. J. 110, 850–859. https://doi.org/10.1016/j.bpj.2015.10.043
Ghosal, D., Chang, Y., Jeong, K.C., Vogel, J.P., Jensen, G.J., 2017. *In situ* structure of the Legionella Dot/Icm type IV secretion system by electron cryotomography. EMBO Rep. 18, 726–732. https://doi.org/10.15252/embr.201643598
Hiasa, M., Abe, M., Nakano, A., Oda, A., Amou, H., Kido, S., Takeuchi, K., Kagawa, K., Yata, K., Hashimoto, T., Ozaki, S., Asaoka, K., Tanaka, E., Moriyama, K., Matsumoto, T., 2009. GM-CSF and IL-4 induce dendritic cell differentiation and disrupt osteoclastogenesis through M-CSF receptor shedding by up-regulation of TNF-α converting enzyme (TACE). Blood 114, 4517–4526. https://doi.org/10.1182/blood-2009-04-215020
Hoiczyk, E., 2000. Structure and sequence analysis of *Yersinia* YadA and Moraxella UspAs reveal a novel class of adhesins. EMBO J. 19, 5989–5999. https://doi.org/10.1093/emboj/19.22.5989
Hu, B., Lara-Tejero, M., Kong, Q., Galán, J.E., Liu, J., 2017. *In Situ* Molecular Architecture of the *Salmonella* Type III Secretion Machine. Cell 168, 1065–1074. https://doi.org/10.1016/j.cell.2017.02.022
Hu, B., Morado, D.R., Margolin, W., Rohde, J.R., Arizmendi, O., Picking, W.L., Picking, W.D., Liu, J., 2015. Visualization of the type III secretion sorting platform of *Shigella flexneri*. Proc. Natl. Acad. Sci. 112, 1047–1052. https://doi.org/10.1073/pnas.1411610112
Hu, J., Worrall, L.J., Hong, C., Vuckovic, M., Atkinson, C.E., Caveney, N., Yu, Z., Strynadka, N.C.J., 2018. Cryo-EM analysis of the T3S injectisome reveals the structure of the needle and open secretin. Nat. Commun. 9, 3840. https://doi.org/10.1038/s41467-018-06298-8
Hu, J., Worrall, L.J., Strynadka, N.C., 2020. Towards capture of dynamic assembly and action of the T3SS at near atomic resolution. Curr. Opin. Struct. Biol. 61, 71–78. https://doi.org/10.1016/j.sbi.2019.10.005
Jackson, M., 2000. Interactions between type III secretion apparatus components from *Yersinia pestis* detected using the yeast two-hybrid system. FEMS Microbiol. Lett. 186, 85–90. https://doi.org/10.1016/S0378-1097(00)00121-X
Johnson, S., Blocker, A., 2008. Characterization of soluble complexes of the *Shigella flexneri* type III secretion system ATPase. FEMS Microbiol. Lett. 286, 274–278. https://doi.org/10.1111/j.1574-6968.2008.01284.x
Journet, L., Agrain, C., Broz, P., Cornelis, G.R., 2003. The Needle Length of Bacterial Injectisomes Is Determined by a Molecular Ruler. Science 302, 1757–1760. https://doi.org/10.1126/science.1091422

Kawamoto, A., Morimoto, Y. V, Miyata, T., Minamino, T., Hughes, K.T., Kato, T., Namba, K., 2013. Common and distinct structural features of *Salmonella* injectisome and flagellar basal body. Sci. Rep. 3, 3369. https://doi.org/10.1038/srep03369

Keller, B., Mühlenkamp, M., Deuschle, E., Siegfried, A., Mössner, S., Schade, J., Griesinger, T., Katava, N., Braunsdorf, C., Fehrenbacher, B., Jiménez-Soto, L.F., Schaller, M., Haas, R., Genth, H., Retta, S.F., Meyer, H., Böttcher, R.T., Zent, R., Schütz, M., Autenrieth, I.B., Bohn, E., 2015. *Yersinia enterocolitica* exploits different pathways to accomplish adhesion and toxin injection into host cells. Cell. Microbiol. 17, 1179–1204. https://doi.org/10.1111/cmi.12429

Kimbrough, T.G., Miller, S.I., 2000. Contribution of *Salmonella* typhimurium type III secretion components to needle complex formation. Proc. Natl. Acad. Sci. 97, 11008–11013. https://doi.org/10.1073/pnas.200209497

Koiwai, K., Hartmann, M.D., Linke, D., Lupas, A.N., Hori, K., 2016. Structural Basis for Toughness and Flexibility in the C-terminal Passenger Domain of an Acinetobacter Trimeric Autotransporter Adhesin. J. Biol. Chem. 291, 3705–3724. https://doi.org/10.1074/jbc.M115.701698

Koretke, K.K., Szczesny, P., Gruber, M., Lupas, A.N., 2006. Model structure of the prototypical non-fimbrial adhesin YadA of *Yersinia enterocolitica*. J. Struct. Biol. 155, 154–161. https://doi.org/10.1016/j.jsb.2006.03.012

Kowal, J., Chami, M., Ringler, P., Müller, S.A., Kudryashev, M., Castaño-Díez, D., Amstutz, M., Cornelis, G.R., Stahlberg, H., Engel, A., 2013. Structure of the Dodecameric *Yersinia enterocolitica* Secretin YscC and Its Trypsin-Resistant Core. Structure 21, 2152–2161. https://doi.org/10.1016/j.str.2013.09.012

Kudryashev, M., Diepold, A., Amstutz, M., Armitage, J.P., Stahlberg, H., Cornelis, G.R., 2015. *Yersinia enterocolitica* type III secretion injectisomes form regularly spaced clusters, which incorporate new machines upon activation. Mol. Microbiol. 95, 875–884. https://doi.org/10.1111/mmi.12908

Kudryashev, M., Stenta, M., Schmelz, S., Amstutz, M., Wiesand, U., Castaño-Díez, D., Degiacomi, M.T., Münnich, S., Bleck, C.K., Kowal, J., Diepold, A., Heinz, D.W., Dal Peraro, M., Cornelis, G.R., Stahlberg, H., 2013. *In situ* structural analysis of the *Yersinia enterocolitica* injectisome. Elife 2, e00792. https://doi.org/10.7554/eLife.00792

Kuhlen, L., Abrusci, P., Johnson, S., Gault, J., Deme, J., Caesar, J., Dietsche, T., Mebrhatu, M.T., Ganief, T., Macek, B., Wagner, S., Robinson, C. V., Lea, S.M., 2018. Structure of the core of the type III secretion system export apparatus. Nat. Struct. Mol. Biol. 25, 583–590. https://doi.org/10.1038/s41594-018-0086-9

Lara-Tejero, M., Qin, Z., Hu, B., Butan, C., Liu, J., Galán, J.E., 2019. Role of SpaO in the assembly of the sorting platform of a *Salmonella* type III secretion system. PLOS Pathog. 15, e1007565. https://doi.org/10.1371/journal.ppat.1007565

Lunelli, M., Kamprad, A., Bürger, J., Mielke, T., Spahn, C.M.T., Kolbe, M., 2020. Cryo-EM structure of the *Shigella* type III needle complex. PLOS Pathog. 16, e1008263. https://doi.org/10.1371/journal.ppat.1008263

Makino, F., Shen, D., Kajimura, N., Kawamoto, A., Pissaridou, P., Oswin, H., Pain, M., Murillo, I., Namba, K., Blocker, A.J., 2016. The Architecture of the Cytoplasmic Region of Type III Secretion Systems. Sci. Rep. 6, 33341. https://doi.org/10.1038/srep33341

Marko, M., Hsieh, C., Schalek, R., Frank, J., Mannella, C., 2007. Focused-ion-beam thinning of frozen-hydrated biological specimens for cryo-electron microscopy. Nat. Methods 4, 215–217. https://doi.org/10.1038/nmeth1014

Marlovits, T.C., Kubori, T., Sukhan, A., Thomas, D.R., Galan, J.E., Unger, V.M., 2004. Structural Insights into the Assembly of the Type III Secretion Needle Complex. Science 306, 1040–1042.

https://doi.org/10.1126/science.1102610
Mastronarde, D.N., Held, S.R., 2017. Automated tilt series alignment and tomographic reconstruction in IMOD. J. Struct. Biol. 197, 102–113. https://doi.org/10.1016/j.jsb.2016.07.011
McDowell, M.A., Marcoux, J., McVicker, G., Johnson, S., Fong, Y.H., Stevens, R., Bowman, L.A.H., Degiacomi, M.T., Yan, J., Wise, A., Friede, M.E., Benesch, J.L.P., Deane, J.E., Tang, C.M., Robinson, C. V., Lea, S.M., 2016. Characterisation of *Shigella* Spa33 and Thermotoga FliM/N reveals a new model for C-ring assembly in T3SS. Mol. Microbiol. 99, 749–766. https://doi.org/10.1111/mmi.13267
Medeiros, J.M., Böck, D., Pilhofer, M., 2018. Imaging bacteria inside their host by cryo-focused ion beam milling and electron cryotomography. Curr. Opin. Microbiol. 43, 62–68. https://doi.org/10.1016/j.mib.2017.12.006
Mota, L.J., Mota, J., Journet, L., Sorg, I., Agrain, C., Cornelis, G.R., 2005. Bacterial Injectisomes: Needle Length Does Matter. Science 307, 1278–1278. https://doi.org/10.1126/science.1107679
Mueller, C.A., Broz, P., Muller, S.A., Ringler, P., Erne-Brand, F., Sorg, I., Kuhn, M., Engel, A., Cornelis, G.R., 2005. The V-Antigen of *Yersinia* Forms a Distinct Structure at the Tip of Injectisome Needles. Science 310, 674–676. https://doi.org/10.1126/science.1118476
Nans, A., Kudryashev, M., Saibil, H.R., Hayward, R.D., 2015. Structure of a bacterial type III secretion system in contact with a host membrane *in situ*. Nat. Commun. 6, 10114. https://doi.org/10.1038/ncomms10114
Nauth, T., Huschka, F., Schweizer, M., Bosse, J.B., Diepold, A., Failla, A.V., Steffen, A., Stradal, T.E.B., Wolters, M., Aepfelbacher, M., 2018. Visualization of translocons in *Yersinia* type III protein secretion machines during host cell infection. PLOS Pathog. 14, e1007527. https://doi.org/10.1371/journal.ppat.1007527
O'Reilly, F.J., Xue, L., Graziadei, A., Sinn, L., Lenz, S., Tegunov, D., Blötz, C., Singh, N., Hagen, W.J.H., Cramer, P., Stülke, J., Mahamid, J., Rappsilber, J., 2020. In-cell architecture of an actively transcribing-translating expressome. Science 369, 554–557. https://doi.org/10.1126/science.abb3758
Park, D., Lara-Tejero, M., Waxham, M.N., Li, W., Hu, B., Galán, J.E., Liu, J., 2018. Visualization of the type III secretion mediated *Salmonella*–host cell interface using cryo-electron tomography. Elife 7, 1–15. https://doi.org/10.7554/eLife.39514
Pujol, C., Bliska, J.B., 2005. Turning *Yersinia* pathogenesis outside in: subversion of macrophage function by intracellular yersiniae. Clin. Immunol. 114, 216–226. https://doi.org/10.1016/j.clim.2004.07.013
Radics, J., Königsmaier, L., Marlovits, T.C., 2014. Structure of a pathogenic type 3 secretion system in action. Nat. Struct. Mol. Biol. 21, 82–87. https://doi.org/10.1038/nsmb.2722
Ravelli, R.B.G., Nijpels, F.J.T., Henderikx, R.J.M., Weissenberger, G., Thewessem, S., Gijsbers, A., Beulen, B.W.A.M.M., López-Iglesias, C., Peters, P.J., 2020. Cryo-EM structures from sub-nl volumes using pin-printing and jet vitrification. Nat. Commun. 11, 2563. https://doi.org/10.1038/s41467-020-16392-5
Rossmann, F.M., Beeby, M., 2018. Insights into the evolution of bacterial flagellar motors from high-throughput *in situ* electron cryotomography and subtomogram averaging. Acta Crystallogr. Sect. D Struct. Biol. 74, 585–594. https://doi.org/10.1107/S2059798318007945
Rueden, C.T., Schindelin, J., Hiner, M.C., DeZonia, B.E., Walter, A.E., Arena, E.T., Eliceiri, K.W., 2017. ImageJ2: ImageJ for the next generation of scientific image data. BMC Bioinformatics 18, 529. https://doi.org/10.1186/s12859-017-1934-z
Russo, C.J., Passmore, L.A., 2014. Ultrastable gold substrates for electron cryomicroscopy. Science

346, 1377–1380. https://doi.org/10.1126/science.1259530

Sage, D., Donati, L., Soulez, F., Fortun, D., Schmit, G., Seitz, A., Guiet, R., Vonesch, C., Unser, M., 2017. DeconvolutionLab2: An open-source software for deconvolution microscopy. Methods 115, 28–41. https://doi.org/10.1016/j.ymeth.2016.12.015

Schaffer, M., Mahamid, J., Engel, B.D., Laugks, T., Baumeister, W., Plitzko, J.M., 2017. Optimized cryo-focused ion beam sample preparation aimed at *in situ* structural studies of membrane proteins. J. Struct. Biol. 197, 73–82. https://doi.org/10.1016/j.jsb.2016.07.010

Schindelin, J., Arganda-Carreras, I., Frise, E., Kaynig, V., Longair, M., Pietzsch, T., Preibisch, S., Rueden, C., Saalfeld, S., Schmid, B., Tinevez, J.-Y., White, D.J., Hartenstein, V., Eliceiri, K., Tomancak, P., Cardona, A., 2012. Fiji: an open-source platform for biological-image analysis. Nat. Methods 9, 676–682. https://doi.org/10.1038/nmeth.2019

Tabrizi, S.N., Robins-Browne, R.M., 1992. Influence of a 70 kilobase virulence plasmid on the ability of *Yersinia enterocolitica* to survive phagocytosis *in vitro*. Microb. Pathog. 13, 171–179. https://doi.org/10.1016/0882-4010(92)90018-J

Tegunov, D., Cramer, P., 2019. Real-time cryo-electron microscopy data preprocessing with Warp. Nat. Methods 16, 1146–1152. https://doi.org/10.1038/s41592-019-0580-y

Thomas, D.R., Francis, N.R., Xu, C., DeRosier, D.J., 2006. The Three-Dimensional Structure of the Flagellar Rotor from a Clockwise-Locked Mutant of *Salmonella enterica* Serovar Typhimurium. J. Bacteriol. 188, 7039–7048. https://doi.org/10.1128/JB.00552-06

van der Wel, N., Hava, D., Houben, D., Fluitsma, D., van Zon, M., Pierson, J., Brenner, M., Peters, P.J., 2007. *M. tuberculosis* and *M. leprae* Translocate from the Phagolysosome to the Cytosol in Myeloid Cells. Cell 129, 1287–1298. https://doi.org/10.1016/j.cell.2007.05.059

VanCleave, T.T., Pulsifer, A.R., Connor, M.G., Warawa, J.M., Lawrenz, M.B., 2017. Impact of Gentamicin Concentration and Exposure Time on Intracellular *Yersinia pestis*. Front. Cell. Infect. Microbiol. 7, 505. https://doi.org/10.3389/fcimb.2017.00505

VanEngelenburg, S.B., Palmer, A.E., 2008. Quantification of Real-Time *Salmonella* Effector Type III Secretion Kinetics Reveals Differential Secretion Rates for SopE2 and SptP. Chem. Biol. 15, 619–628. https://doi.org/10.1016/j.chembiol.2008.04.014

Wagner, S., Königsmaier, L., Lara-Tejero, M., Lefebre, M., Marlovits, T.C., Galán, J.E., 2010. Organization and coordinated assembly of the type III secretion export apparatus. Proc. Natl. Acad. Sci. 107, 17745–17750. https://doi.org/10.1073/pnas.1008053107

Wagner, S., Sorg, I., Degiacomi, M., Journet, L., Peraro, M.D., Cornelis, G.R., 2009. The helical content of the YscP molecular ruler determines the length of the *Yersinia* injectisome. Mol. Microbiol. 71, 692–701. https://doi.org/10.1111/j.1365-2958.2008.06556.x

Weiss, G.L., Kieninger, A.-K., Maldener, I., Forchhammer, K., Pilhofer, M., 2019. Structure and Function of a Bacterial Gap Junction Analog. Cell 178, 374-384.e15. https://doi.org/10.1016/j.cell.2019.05.055

Wimmi, S., Balinovic, A., Jeckel, H., Selinger, L., Lampaki, D., 2020. Dynamic relocalization of the cytosolic type III secretion system components prevents premature protein secretion at low external pH. bioRxiv 869214. https://doi.org/doi.org/10.1101/869214

Worrall, L.J., Hong, C., Vuckovic, M., Deng, W., Bergeron, J.R.C., Majewski, D.D., Huang, R.K., Spreter, T., Finlay, B.B., Yu, Z., Strynadka, N.C.J., 2016. Near-atomic-resolution cryo-EM analysis of the *Salmonella* T3S injectisome basal body. Nature. https://doi.org/10.1038/nature20576

Yu, X.J., Liu, M., Matthews, S., Holden, D.W., 2011. Tandem translation generates a chaperone for the *Salmonella* type III secretion system protein SsaQ. J. Biol. Chem. 286, 36098–36107. https://

doi.org/10.1074/jbc.M111.278663
Zachs, T., Schertel, A., Medeiros, J., Weiss, G.L., Hugener, J., Matos, J., Pilhofer, M., 2020. Fully automated, sequential focused ion beam milling for cryo-electron tomography. Elife 9, 1–14. https://doi.org/10.7554/eLife.52286
Zhang, Y., Lara-Tejero, M., Bewersdorf, J., Galán, J.E., 2017. Visualization and characterization of individual type III protein secretion machines in live bacteria. Proc. Natl. Acad. Sci. U. S. A. 114, 6098–6103. https://doi.org/10.1073/pnas.1705823114
Zheng, S.Q., Palovcak, E., Armache, J.-P., Verba, K.A., Cheng, Y., Agard, D.A., 2017. MotionCor2: anisotropic correction of beam-induced motion for improved cryo-electron microscopy. Nat. Methods 14, 331–332. https://doi.org/10.1038/nmeth.4193

Chapter 5

In situ and *in vitro* cryo-EM reveal structures of mycobacterial encapsulin assembly intermediates

Casper Berger*, Chris Lewis*, Y. Gao, Kèvin Knoops, Carmen López-Iglesias, Peter J. Peters, Raimond B. G. Ravelli

* Shared first author

Submitted

Chapter 6

General discussion

1. Establishing an *in situ* cryo-electron tomography workflow

In this PhD project we successfully established an *in situ* cryo-electron tomography workflow using FIB-lamella fabrication. This enabled the *in situ* structural analysis of the type III secretion system (**Chapter 4**) and the mycobacterial encapsulin (**Chapter 5**), and laid the foundation for future studies using these techniques at M4i Nanoscopy.

One of the difficulties of these techniques is that the workflow consists of many different steps, which each must be reliable to allow *in situ* structure determination. Consistent sample preparation was initially challenging, but was iteratively improved to the point where most grids were suitable for FIB-lamella fabrication. Pivotal in this process was the use of gold-foil EM grids (UltrAufoil), which proved much less fragile than the carbon film grids we used previously. Also FIB-lamella fabrication was an initial bottleneck. By identifying and resolving vacuum and stability issues in the FIB/SEM dualbeam instrument, followed by iteratively improving the FIB-lamellae fabrication process enabled consistent lamella fabrication of up to 10 lamella per day. Data processing, visualization, interpretation and subtomograms averaging were all successfully performed. These processing steps as performed in this PhD project still required substantial manual input. The throughput could be substantially increased by further streamlining and automating these steps (Himes and Zhang, 2018; Chen *et al.*, 2019; Wagner *et al.*, 2019; Xu *et al.*, 2019; Martinez-Sanchez *et al.*, 2020; Tegunov *et al.*, 2021). In **Chapter 2** we describe the most recent development in CET on FIB-lamellae, the unique capabilities offered by *in situ* tomography for structural biology and the future potential for these techniques.

2. Tilt-series alignment on FIB-lamellae

The accurate alignment of CET tilt-series recorded on FIB-lamellae is challenging due to the lack of fiducials and the low contrast, in particular at high tilt-angles. In **Chapter 3** we describe how endocytosis pathways of mammalian cells can be exploited to localize 10 nm BSA-gold fiducials into FIB lamellae, and show that alignment of tilt-series with BSA-gold is more accurate compared to fiducial-less patch-tracking. Accurate tilt-series alignment has been shown to contribute to the resolution obtained with subtomogram averaging (Fernandez *et al.*, 2018, 2019; Himes and Zhang, 2018; Chen *et al.*, 2019) and this method may therefore contribute to *in situ* structural biology using CET on FIB-lamellae.

Endocytosis of BSA-gold is simple to apply, as it only requires the addition of BSA-gold to the cells one hour before vitrification. The method was particularly effective for cells infected with *Yersinia enterocolitica*, where each of the over 150 collected tilt-series could be aligned with BSA-gold. We noticed that inhomogeneities in the platinum layer sputtered onto the finished lamella may also be used to align tilt-series (Fig. 1). The downsides of this method are that software for tracking gold fiducials typically assume spherical objects of homogenous

size and therefore don't work as well on the platinum densities and non-spherical objects may look different at different tilt angles resulting in less accurate centering of the fiducials. It may perhaps be possible to modify the platinum sputter coating conditions to result in platinum depositions that are more spherical and homogenous in size as a general method to reliably deposit fiducials on FIB-lamellae of any sample.

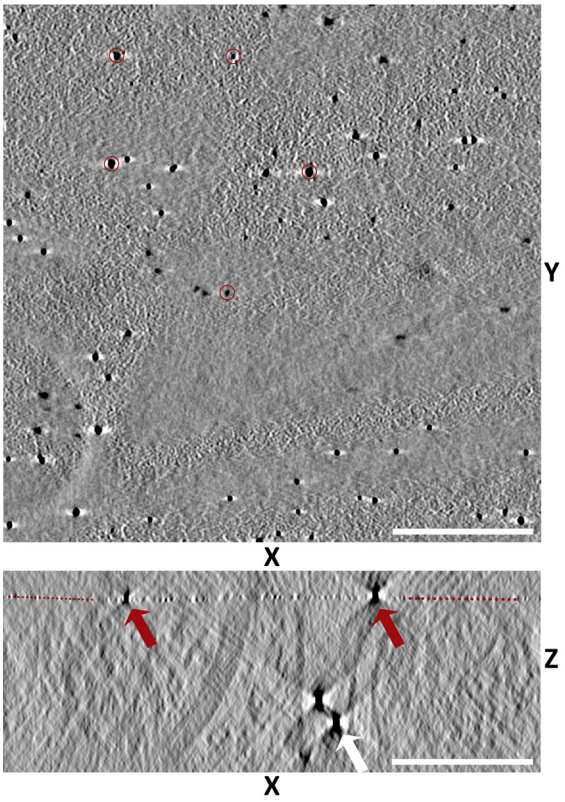

Figure 1. Top panel: Slice of cryo-electron tomogram of the platinum sputtered on a FIB-lamella. Electron-dense inhomogeneities with variable shapes are visible in the platinum layer as black dots (red circles). Bottom panel: slice of the same tomogram in the XZ direction. The platinum layer is visible as a line on the top of the lamella (red dashed line). Two platinum inhomogeneities can be observed in this slice (red arrows) as well as two 10-nm gold fiducials that were endocytosed by the cell (white arrow). Scale bar: 200 nm.

3. *In situ* structure of the type III secretion system

In **Chapter 4** we use the CET on FIB-lamellae workflow to determine the structure of the type III secretion system of *Yersinia enterocolitica* during intracellular infection. We observed that a minimal needle length is required to make host contact and find structural differences in the cytosolic sorting platform compared to other bacterial species. The findings in this work contribute towards understanding how the type III secretion system is able to perform its function in relation to the host cell.

The structure was determined using 202 subtomograms from 65 tomograms, for which over a 150 tilt-series on FIB lamellae were acquired. The number of particles proved to be a limitation in this study; more particles would have likely resulted in a higher resolution structure and may have allowed for classification to be performed to look for different structural states between contact and non-contact injectisomes with greater confidence. Developments in (automated) lamella fabrication, tilt-series acquisition and data processing may increase the speed of data acquisition (**Chapter 2**) and make studying structural heterogeneity of rare macromolecular complexes more feasible.

4. Searching for the mycobacterial type VII secretion system

To determine the structure of the mycobacterial type VII secretion system, we collected over 200 tilt-series of *Mycobacterium marinum* either with or without the host infection context. However, contrary to the type III secretion system of *Y. enterocolitica*, we were unable to visually identify distinct transmembrane complexes in mycobacteria that could be the type VII secretion system.

Differences in the structure of the type VII secretion system and bacterial envelope are likely factors to have contributed to this. For the TIIISS of *Y. enterocolitica*, injectosomes could be visually identified by the more electron-dense basal body compared to the bacterial envelope and the needle that protrudes into the phagosomal vacuoles of the host. Based on the structures of the isolated type VII secretion, the ESX-systems are 28 nm wide at the inner membrane, and have a height of 20 nm (Beckham *et al.*, 2017; Famelis *et al.*, 2019; Poweleit *et al.*, 2019; Bunduc *et al.*, 2021). No ESX components have been identified yet that span the bacterial outer membrane. We observed that both *M. marinum* and *M. smegmatis* have a substantially more electron-dense envelope compared to the gram-negative *Y. enterocolitica* (fig. 2). This is in line with the known high lipid content of the mycobacterial envelope, including the long-chain mycolic acids and low-permeability of the mycobacterial envelope for nutrients and antibiotics (Chiaradia *et al.*, 2017; Reed *et al.*, 2018). The high density of the mycobacterial envelope likely explains why we were unable to observe any clear transmembrane complexes in the mycobacterial envelope.

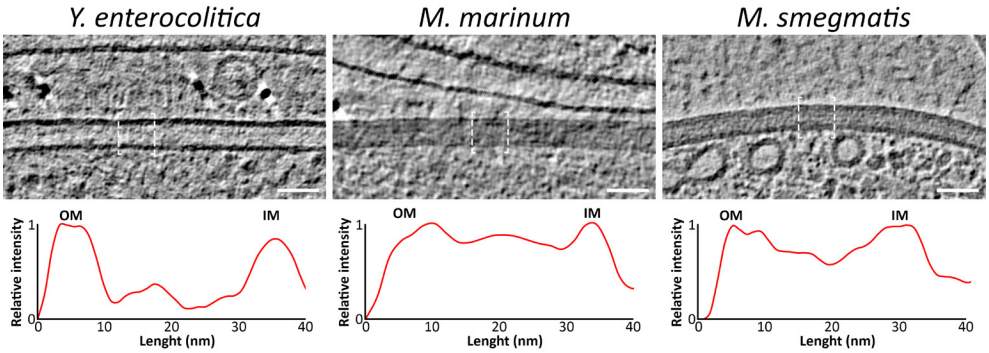

Figure 2. Top panels show representative tomographic slices of *Y. enterocolitica*, *M. marinum* and *M. smegmatis*. An injectisome is visible in the center of the slice of *Y. enterocolitica*. White dashed lines indicate membranes where line profiles were determined (bottom panels). Bottom panels show representative line profiles from the outer membrane (OM) to the inner membrane (IM), where the inverted relative pixel intensity is scaled from light (0) to dark (1). Scale bars: 50 nm.

Based on single-particle structures of isolated ESX-3 and -5, the cytosolic domain should extend ±14 nm into the cytosol (Beckham *et al.*, 2017; Famelis *et al.*, 2019; Poweleit *et al.*, 2019; Bunduc *et al.*, 2021), which may enable visual recognition of ESX complexes. However, the cytosolic sorting platform of the type III secretion system was generally difficult to discern in individual tomograms. The cytosolic sorting platform of the T3SS is described as a dynamic structure (Diepold *et al.*, 2017), and effective subtomograms averaging of this structure required specific masking of this region, suggesting flexibility, which may explain why it is difficult to visualize in tomograms. Likewise, EccC of the type VII secretion system, which extends the furthest into the cytosol, is highly flexible (Rosenberg *et al.*, 2015; Bunduc *et al.*, 2021). Like the cytosolic domains of the type III secretion system, the cytosolic domains of ESX may be difficult to discern in tomograms.

We also did not observe clear needle structures, which were readily visible for the T3SS system. Lou *et al.* observed polymerization of the ESX-1 substrate EspC *in vitro*, as well as linear depositions of immunogold specific for EspC on the outside of *M. tuberculosis*, which may suggest that EspC could form a hollow needle structure, similar to the type III secretion system (Lou *et al.*, 2017). Likewise, Gijsbers *et al.* Propose three different models for secretion of the ESX-1 substrate EspB based on its structural features; EspB forms a pore-like structure with a similar diameter to the cytosolic portion of ESX-5 which contains EspB monomers *in vitro*. One of the models proposes that EspB may form a needle-like structure between the outer membrane and the host phagosomal membrane (Gijsbers *et al.*, 2021). However, the absence of clear needle structures in the tomographic data may suggest that the type VII secretion system does not have a large needle like the type III secretion system.

It is unlikely that any of the different ESX systems are not expressed at the time point of cryo-fixation. ESX-5 is known to be essential for many mycobacteria, including *M. marinum* (Ates *et al.*, 2015). We observed a large number of bacteria that have translocated from the phagosome, and it is well established that ESX-1 is essential for this process (van der Wel *et al.*, 2007; Houben *et al.*, 2012; Simeone *et al.*, 2012). Therefore, ESX-1 must have at least been transiently expressed and assembled at the timepoints we used. Secretion systems may be present in low copy numbers, but considering that we recorded over 200 tilt-series, it's highly unlikely that no ESX systems were present in any of the reconstructed tomograms. The structural differences in the bacterial envelope between mycobacteria and gram-negative bacteria and the absence of clearly identifiable needle structures therefore likely explain why we were unable to visually identify ESX-complexes it in the data.

Since visual identification of the type VII secretion system is difficult, algorithms for finding unknown macromolecular complexes may be more successful (Xu *et al.*, 2019; Martinez-Sanchez *et al.*, 2020). However, the low contrast between ESX and the mycobacterial envelope likely also reduces the success of such algorithms. While incremental improvements in EM hardware (e.g. cold field immersion gun (Maki-Yonekura *et al.*, 2021), new generation energy filters and detectors (Nakane *et al.*, 2020), data acquisition strategies like dose symmetric tilt schemes (Hagen *et al.*, 2017; Turoňová *et al.*, 2020) or novel algorithms for improving the visual clarity of tomograms (Buchholz *et al.*, 2019; Tegunov and Cramer, 2019; Bepler *et al.*, 2020) may increase the contrast of acquired tomograms, a different strategy may be more successful to identify the type VII secretion system *in situ*.

Fluorescent labeling of ESX-1 using a fusion protein may in principle allow for the localization of ESX-1 within tomograms. Fluorescent labeling strategies using fluorescent fusions have been successful for different secretion systems, including the type III and type VI secretion system (Basler *et al.*, 2012; Gerc *et al.*, 2015; Diepold *et al.*, 2017). However, correlative light and electron microscopy (CLEM) with a high-localization precision currently remains challenging due to limited resolution (discussed in **Chapter 2**). Alternatively, an *in situ* label visible in cryo-tomograms such as an encapsulin fusion protein (Sigmund *et al.*, 2018, 2019) may enable identification of the type VII secretion system *in situ*. Promising candidates for (fluorescent) labeling of ESX-1 without impeding its biological functions could be the C-terminus of EccCb1 (Wirth *et al.*, 2012; van Winden *et al.*, 2016) or based on the structure of ESX-3 and -5, the C-terminus of EccD.

5. Molecular diversity at the nanometer scale

One of the strengths of *in situ* cryo-electron tomography is visualizing the entire cellular environment. Tomograms recorded with the aim of finding a specific macromolecular complex may contain other proteins and structures of biological interest (Dobro *et al.*, 2017). In the over 200 tomograms recorded of *M. marinum*, we found ±23 nm wide objects which we later identified as proteinaceous storage compartments termed encapsulins, which could be structurally analyzed by subtomogram averaging (**Chapter 5**). We identified partially assembled encapsulins, which could be analyzed in more structural detail using single particle analysis of isolated encapsulins. These findings contribute to understanding the assembly and disassembly of bacterial encapsulins.

A large number of other structures were also identified in these tomograms that may yield relevant novel scientific insights when systematically analyzed (Fig. 3-5). These include different bacterial membrane vesicles and invaginations (Fig. 3A-C), mycobacterial storage compartments (Fig. 3D-F) and the mycobacterial septum in different stages of development (Fig. 4). In the mammalian host cells, we identified protein storage compartments termed vault complexes (Fig. 5A) (Woodward *et al.*, 2015), nuclear pore complexes (Fig. 5B) (Allegretti *et al.*, 2020) and regular, almost crystalline lattices of a putative macromolecule (Fig. 5C).

The wide range of macromolecules and structures that may be structurally or morphologically analyzed in this type of *in situ* data creates both opportunities as well as challenges for scientists. A thorough biological understanding is required for these different macromolecules and structures to identify relevant scientific questions that may be answered with these data. Studying the biology, analyzing the data and reporting these findings can be very time-consuming. Collaboration and discussion with experts in the biology of these different cellular components can help identify relevant scientific questions and speed up this process. Effective sharing and annotating of large dataset may also help to use *in situ* tomography data to its full potential. Raw tilt-series data is often made publicly available via databases (e.g. EMPIAR), which has proven particularly useful for methods development, to allow analysis of the same dataset by different methods. Tools to publicly search, segment and annotate tomograms could in principle allow for the subcellular distribution and structural heterogeneity of macromolecules to be studies aggregated from different datasets, in particular when combined with reliable automation of segmentation and particle picking.

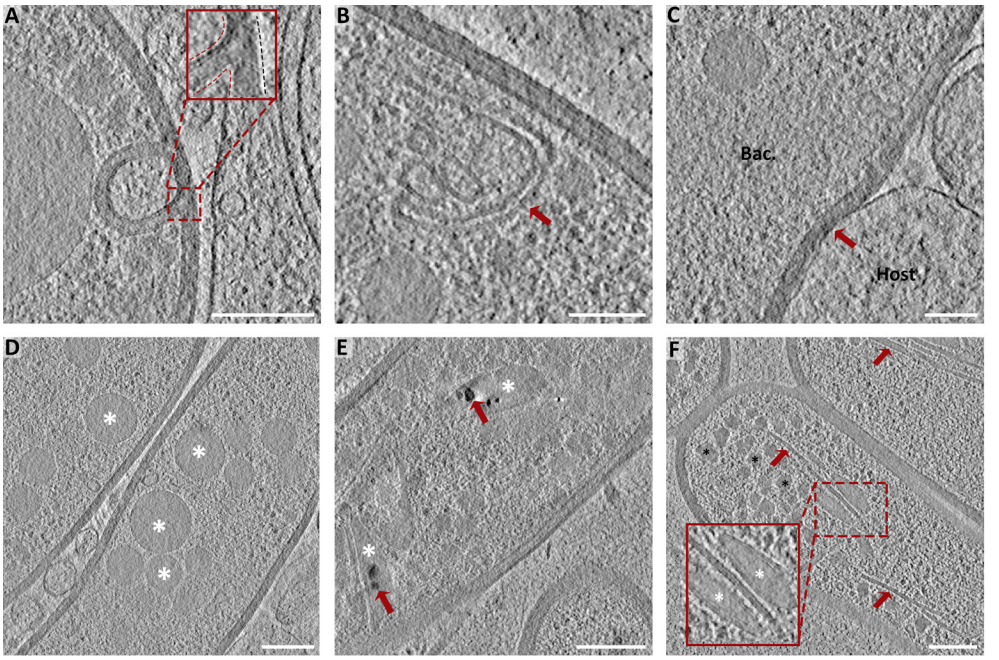

Figure 3. Overview of different structures observed in tomogram of FIB-lamellae of *M. marinum* during intracellular infection or without the infection context. (A) Invagination of the bacterial envelope into the bacterial cytosol. The inner membrane sharply curves inward to form the invagination (red dashed lines) whereas the outer membrane follows the overall curvature of the bacterium (black dashed lines). Scale bar: 200 nm. (B) Cytosolic membrane structures formed by a single bilayer. Scale bar: 200 nm (C) Close interaction of the bacterial envelope with a host membrane (red arrow). In most cases, bacterial and host membranes are not observed to be in direct contact. The bacterial envelope is locally deformed at the interaction site. Scale bar: 100 nm. (D) Bacterial storage compartments (white stars) that are typically spherical, with a homogenous content and thin electron-dense border between the storage compartment and the cytosol. Based on their strong morphological similarities to mammalian lipids droplets (spherical, homogenous electron-dense interior, electron-dense border from lipid monolayer), these compartments likely store lipids. Scale bar: 200 nm. (E) Storage compartments that are not spherical, but with the same homogenous electron-dense interior as the putative lipid storage compartment were observed as well (white stars). Some of these compartments contain electron-dense bodies (red arrows). These may possibly be formed by depositions of electron-dense minerals, similar to calcium deposits in mitochondria (Wolf *et al.*, 2017). Scale bar: 200 nm. (F) Elongated structures (red arrows) were frequently observed as well. These structures are characterized by two or up to several sharp electron-dense lines with a homogenous background. They are often found in close proximity and/or contact with non-spherical lipid storage compartments (white stars). While morphologically similar in appearance to bacterial microtubules (Pilhofer *et al.*, 2011), these structures are shaped like sheaths, rather than tubes. Numerous other storage compartments are visible as well (black stars). These storage compartments were frequently observed for bacteria without an infection context, and only rarely during intracellular infection. In contrast, the putative lipid storage compartment shown in panel D were primarily observed during intracellular infection, and more rarely without the infection context. Scale bar: 200 nm.

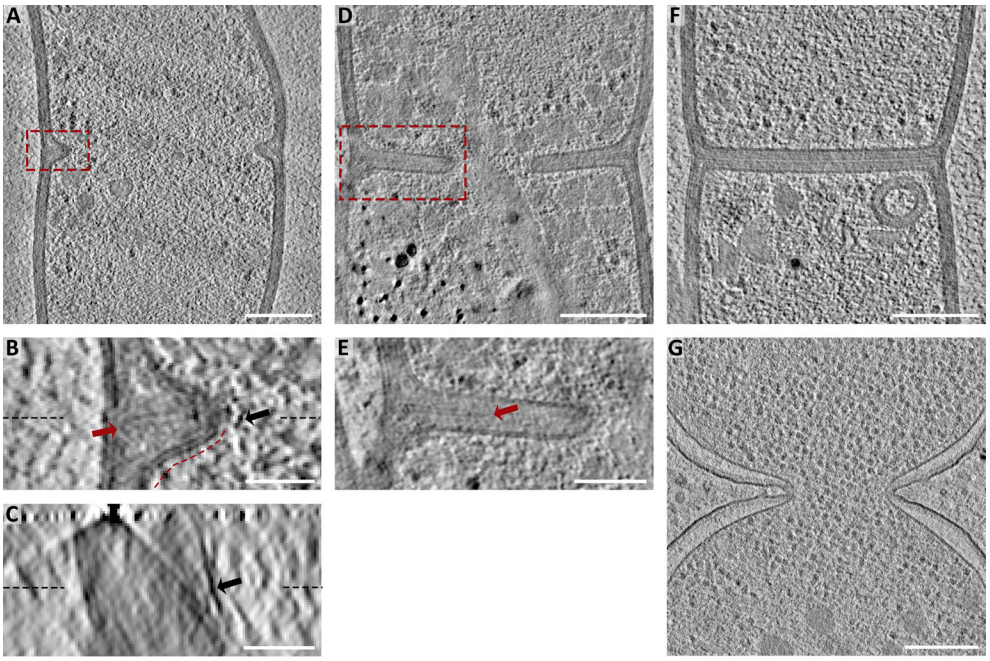

Figure 4. Tomographic slices of *M. marinum* in different stages of septum formation during cell division. (A-C) early stage of septum formation. The bacterium is only slightly more narrow where the septum is formed, as described previously (Eskandarian *et al.*, 2017; Odermatt *et al.*, 2020). In panel B (rectangle with red dashed lines in panel A), the early septum appears to be formed by an invagination of the inner membrane (red dashed line). The mid septal zone (Matias and Beveridge, 2007) is visible as well (red arrow), and extends from close to the inner membrane to the tip of the septum. Several electron-dense spots are visible near the top of the septum (black arrow), which form a filamentous structure when seen in an XZ slice of the same tomogram (panel C). These filaments are likely to be FtsZ filaments (Li *et al.*, 2007), which are known to be involved in (myco)bacterial cell division, where they form a Z ring (Baranowski *et al.*, 2019). Black dashed lines in panel B and C indicate the position where the XY and XZ perspectives in panel B and C intersect. (D, E) intermediate stage of septum formation. The mid septal zone is now only visible up to halfway in the forming septum, suggesting that its formation may be slower than the invagination of the inner membrane. Rectangle with red dashed lines in panel D indicates the area in panel E. (F) tomographic slice showing a completed septum. The invaginated inner membranes and mid septal zones from all sides of the bacterium appear to have fused. The bacterium is slightly narrower near the septum. (G) Tomographic slice of *Yersinia enterocolitica* during bacterial cell division. In gram-negative bacteria no septum is formed like in gram-positive bacteria, and instead the cell envelope is constricted to pinch off the daughter cell. Scale bars panel A, D, F and G: 200 nm. Scale bars panel B, C and E: 50 nm.

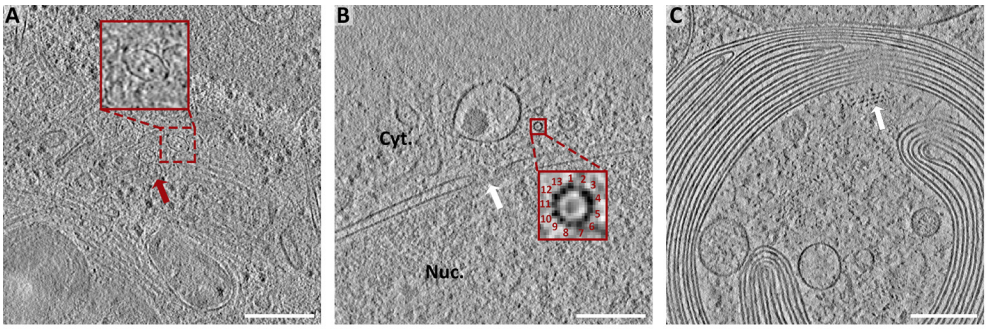

Figure 5. (A) Overview of host cell structures observed in tomograms of FIB-lamella. (A) tomographic slice containing several vault complexes of the host (red arrow and enlarged inset). (B) tomographic slice of the nuclear envelope containing a nuclear core complex (white arrow). A top view of a microtubule is visible as well, where the 13 tubulin dimers can be individually seen. (C) Tomographic slice of MHC class II compartment, where the complex morphology of membranes is clearly visible. An unidentified regular array of macromolecules is visible in the lumen (white arrow). Scale bars: 200 nm.

6. Future perspective

Over the years, CET on FIB-lamellae for biological samples has evolved from a proof of principle (Marko *et al.*, 2006, 2007) into a technique capable of characterizing protein structure within their native cellular environment (Asano *et al.*, 2015; Engel *et al.*, 2015; Mahamid *et al.*, 2016) and are now applied for *in situ* structural biology (Turk and Baumeister, 2020). Recently, advances in data acquisition, processing and subtomogram averaging have greatly increased the resolutions that can be achieved with tomography, resulting in several studies demonstrating sub-nanometer *in situ* structures (Sutton *et al.*, 2020; Tegunov *et al.*, 2021; Wang *et al.*, 2021).

Current limitations of cellular tomography are the limited resolution compared to structural techniques on isolated macromolecules, and the high costs in money and time. The challenge for the coming years is to make the workflows faster and more robust, to consistently reach near-atomic resolution on a wide range of macromolecular complexes. Less expensive instrumentation may make cellular tomography available to more scientist to help answer a diverse range of biological research questions. The nature of cellular tomography allows for a wide range of biological structures to be observed in a given dataset. Scientific collaboration with experts in their respective biological fields can help to use this data to its fullest potential. The unique capability to study the structural heterogeneity of macromolecules within its native cellular environment has the potential to transform our understanding of macromolecule structure in relation to cellular function; to bridge cell- and structural biology.

References

Allegretti, M., Zimmerli, C.E., Rantos, V., Wilfling, F., Ronchi, P., Fung, H.K.H., Lee, C.-W., Hagen, W., Turoňová, B., Karius, K., Börmel, M., Zhang, X., Müller, C.W., Schwab, Y., Mahamid, J., Pfander, B., Kosinski, J., Beck, M., 2020. In-cell architecture of the nuclear pore and snapshots of its turnover. Nature 586, 796–800. https://doi.org/10.1038/s41586-020-2670-5

Asano, S., Fukuda, Y., Beck, F., Aufderheide, A., Förster, F., Danev, R., Baumeister, W., 2015. A molecular census of 26S proteasomes in intact neurons. Science (80-.). 347, 439–442. https://doi.org/10.1126/science.1261197

Ates, L.S., Ummels, R., Commandeur, S., van der Weerd, R., Sparrius, M., Weerdenburg, E., Alber, M., Kalscheuer, R., Piersma, S.R., Abdallah, A.M., Abd El Ghany, M., Abdel-Haleem, A.M., Pain, A., Jiménez, C.R., Bitter, W., Houben, E.N.G., 2015. Essential Role of the ESX-5 Secretion System in Outer Membrane Permeability of Pathogenic Mycobacteria. PLOS Genet. 11, e1005190. https://doi.org/10.1371/journal.pgen.1005190

Baranowski, C., Rego, E.H., Rubin, E.J., 2019. The Dream of a Mycobacterium. Microbiol. Spectr. 7, 1–14. https://doi.org/10.1128/microbiolspec.GPP3-0008-2018

Basler, M., Pilhofer, M., Henderson, G.P., Jensen, G.J., Mekalanos, J.J., 2012. Type VI secretion requires a dynamic contractile phage tail-like structure. Nature 483, 182–186. https://doi.org/10.1038/nature10846

Beckham, K.S.H., Ciccarelli, L., Bunduc, C.M., Mertens, H.D.T., Ummels, R., Lugmayr, W., Mayr, J., Rettel, M., Savitski, M.M., Svergun, D.I., Bitter, W., Wilmanns, M., Marlovits, T.C., Parret, A.H.A., Houben, E.N.G., 2017. Structure of the mycobacterial ESX-5 type VII secretion system membrane complex by single-particle analysis. Nat. Microbiol. 2, 17047. https://doi.org/10.1038/nmicrobiol.2017.47

Bepler, T., Kelley, K., Noble, A.J., Berger, B., 2020. Topaz-Denoise: general deep denoising models for cryoEM and cryoET. Nat. Commun. 11, 5208. https://doi.org/10.1038/s41467-020-18952-1

Buchholz, T.-O., Krull, A., Shahidi, R., Pigino, G., Jékely, G., Jug, F., 2019. Content-aware image restoration for electron microscopy, in: Proceedings - International Symposium on Biomedical Imaging. pp. 277–289. https://doi.org/10.1016/bs.mcb.2019.05.001

Bunduc, C.M., Fahrenkamp, D., Wald, J., Ummels, R., Bitter, W., Houben, E.N.G., Marlovits, T.C., 2021. Structure and dynamics of a mycobacterial type VII secretion system. Nature 593, 445–448. https://doi.org/10.1038/s41586-021-03517-z

Chen, M., Bell, J.M., Shi, X., Sun, S.Y., Wang, Z., Ludtke, S.J., 2019. A complete data processing workflow for cryo-ET and subtomogram averaging. Nat. Methods 16, 1161–1168. https://doi.org/10.1038/s41592-019-0591-8

Chiaradia, L., Lefebvre, C., Parra, J., Marcoux, J., Burlet-Schiltz, O., Etienne, G., Tropis, M., Daffé, M., 2017. Dissecting the mycobacterial cell envelope and defining the composition of the native mycomembrane. Sci. Rep. 7, 12807. https://doi.org/10.1038/s41598-017-12718-4

Diepold, A., Sezgin, E., Huseyin, M., Mortimer, T., Eggeling, C., Armitage, J.P., 2017. A dynamic and adaptive network of cytosolic interactions governs protein export by the T3SS injectisome. Nat. Commun. 8, 15940. https://doi.org/10.1038/ncomms15940

Dobro, M.J., Oikonomou, C.M., Piper, A., Cohen, J., Guo, K., Jensen, T., Tadayon, J., Donermeyer, J., Park, Y., Solis, B.A., Kjær, A., Jewett, A.I., McDowall, A.W., Chen, S., Chang, Y.-W., Shi, J., Subramanian, P., Iancu, C. V., Li, Z., Briegel, A., Tocheva, E.I., Pilhofer, M., Jensen, G.J., 2017. Uncharacterized Bacterial Structures Revealed by Electron Cryotomography. J. Bacteriol. 199, 1–14. https://doi.org/10.1128/JB.00100-17

Engel, B.D., Schaffer, M., Albert, S., Asano, S., Plitzko, J.M., Baumeister, W., 2015. *In situ* structural analysis of Golgi intracisternal protein arrays. Proc. Natl. Acad. Sci. U. S. A. 112, 11264–9. https://doi.org/10.1073/pnas.1515337112

Eskandarian, H.A., Odermatt, P.D., Ven, J.X.Y., Hannebelle, M.T.M., Nievergelt, A.P., Dhar, N., McKinney, J.D., Fantner, G.E., 2017. Division site selection linked to inherited cell surface wave troughs in mycobacteria. Nat. Microbiol. 2, 17094. https://doi.org/10.1038/nmicrobiol.2017.94

Famelis, N., Rivera-Calzada, A., Degliesposti, G., Wingender, M., Mietrach, N., Skehel, J.M., Fernandez-Leiro, R., Böttcher, B., Schlosser, A., Llorca, O., Geibel, S., 2019. Architecture of the mycobacterial type VII secretion system. Nature 576, 321–325. https://doi.org/10.1038/s41586-019-1633-1

Fernandez, J.-J., Li, S., Agard, D.A., 2019. Consideration of sample motion in cryo-tomography based on alignment residual interpolation. J. Struct. Biol. 205, 1–6. https://doi.org/10.1016/j.jsb.2019.01.005

Fernandez, J.-J., Li, S., Bharat, T.A.M., Agard, D.A., 2018. Cryo-tomography tilt-series alignment with consideration of the beam-induced sample motion. J. Struct. Biol. 202, 200–209. https://doi.org/10.1016/j.jsb.2018.02.001

Gerc, A.J., Diepold, A., Trunk, K., Porter, M., Rickman, C., Armitage, J.P., Stanley-Wall, N.R., Coulthurst, S.J., 2015. Visualization of the Serratia Type VI Secretion System Reveals Unprovoked Attacks and Dynamic Assembly. Cell Rep. 12, 2131–2142. https://doi.org/10.1016/j.celrep.2015.08.053

Gijsbers, A., Vinciauskaite, V., Siroy, A., Gao, Y., Tria, G., Mathew, A., Sánchez-Puig, N., López-Iglesias, C., Peters, P.J., Ravelli, R.B.G., 2021. Priming mycobacterial ESX-secreted protein B to form a channel-like structure. Curr. Res. Struct. Biol. 3, 153–164. https://doi.org/10.1016/j.crstbi.2021.06.001

Hagen, W.J.H., Wan, W., Briggs, J.A.G., 2017. Implementation of a cryo-electron tomography tilt-scheme optimized for high resolution subtomogram averaging. J. Struct. Biol. 197, 191–198. https://doi.org/10.1016/j.jsb.2016.06.007

Himes, B.A., Zhang, P., 2018. emClarity: software for high-resolution cryo-electron tomography and subtomogram averaging. Nat. Methods 15, 955–961. https://doi.org/10.1038/s41592-018-0167-z

Houben, D., Demangel, C., van Ingen, J., Perez, J., Baldeón, L., Abdallah, A.M., Caleechurn, L., Bottai, D., van Zon, M., de Punder, K., van der Laan, T., Kant, A., Bossers-de Vries, R., Willemsen, P., Bitter, W., van Soolingen, D., Brosch, R., van der Wel, N., Peters, P.J., 2012. ESX-1-mediated translocation to the cytosol controls virulence of mycobacteria. Cell. Microbiol. 14, 1287–1298. https://doi.org/10.1111/j.1462-5822.2012.01799.x

Li, Z., Trimble, M.J., Brun, Y. V., Jensen, G.J., 2007. The structure of FtsZ filaments *in vivo* suggests a force-generating role in cell division. EMBO J. 26, 4694–4708. https://doi.org/10.1038/sj.emboj.7601895

Lou, Y., Rybniker, J., Sala, C., Cole, S.T., 2017. EspC forms a filamentous structure in the cell envelope of *Mycobacterium tuberculosis* and impacts ESX-1 secretion. Mol. Microbiol. 103, 26–38. https://doi.org/10.1111/mmi.13575

Mahamid, J., Pfeffer, S., Schaffer, M., Villa, E., Danev, R., Kuhn Cuellar, L., Forster, F., Hyman, A.A., Plitzko, J.M., Baumeister, W., 2016. Visualizing the molecular sociology at the HeLa cell nuclear periphery. Science (80-.). 351, 969–972. https://doi.org/10.1126/science.aad8857

Maki-Yonekura, S., Hamaguchi, T., Naitow, H., Takaba, K., Yonekura, K., 2021. Advances in cryo-EM and ED with a cold-field emission beam and energy filtration —Refinements of the CRYO ARM 300 system in RIKEN SPring-8 center—. Microscopy 70, 232–240. https://doi.org/10.1093/jmicro/dfaa052

Marko, M., Hsieh, C., Moberlychan, W., Mannella, C.A., Frank, J., 2006. Focused ion beam milling of vitreous water: prospects for an alternative to cryo-ultramicrotomy of frozen-hydrated biological samples. J. Microsc. 222, 42–47. https://doi.org/10.1111/j.1365-2818.2006.01567.x

Marko, M., Hsieh, C., Schalek, R., Frank, J., Mannella, C., 2007. Focused-ion-beam thinning of frozen-hydrated biological specimens for cryo-electron microscopy. Nat. Methods 4, 215–217. https://doi.org/10.1038/nmeth1014

Martinez-Sanchez, A., Kochovski, Z., Laugks, U., Meyer zum Alten Borgloh, J., Chakraborty, S., Pfeffer, S., Baumeister, W., Lučić, V., 2020. Template-free detection and classification of membrane-bound complexes in cryo-electron tomograms. Nat. Methods 17. https://doi.org/10.1038/s41592-019-0675-5

Matias, V.R.F., Beveridge, T.J., 2007. Cryo-electron microscopy of cell division in Staphylococcus aureus reveals a mid-zone between nascent cross walls. Mol. Microbiol. 64, 195–206. https://doi.org/10.1111/j.1365-2958.2007.05634.x

Nakane, T., Kotecha, A., Sente, A., McMullan, G., Masiulis, S., Brown, P.M.G.E., Grigoras, I.T., Malinauskaite, L., Malinauskas, T., Miehling, J., Uchański, T., Yu, L., Karia, D., Pechnikova, E. V, de Jong, E., Keizer, J., Bischoff, M., McCormack, J., Tiemeijer, P., Hardwick, S.W., Chirgadze, D.Y., Murshudov, G., Aricescu, A.R., Scheres, S.H.W., 2020. Single-particle cryo-EM at atomic resolution. Nature 587, 152–156. https://doi.org/10.1038/s41586-020-2829-0

Odermatt, P.D., Hannebelle, M.T.M., Eskandarian, H.A., Nievergelt, A.P., McKinney, J.D., Fantner, G.E., 2020. Overlapping and essential roles for molecular and mechanical mechanisms in mycobacterial cell division. Nat. Phys. 16, 57–62. https://doi.org/10.1038/s41567-019-0679-1

Pilhofer, M., Ladinsky, M.S., McDowall, A.W., Petroni, G., Jensen, G.J., 2011. Microtubules in Bacteria: Ancient Tubulins Build a Five-Protofilament Homolog of the Eukaryotic Cytoskeleton. PLoS Biol. 9, e1001213. https://doi.org/10.1371/journal.pbio.1001213

Poweleit, N., Czudnochowski, N., Nakagawa, R., Trinidad, D.D., Murphy, K.C., Sassetti, C.M., Rosenberg, O.S., 2019. The structure of the endogenous ESX-3 secretion system. Elife 8, 1–20. https://doi.org/10.7554/eLife.52983

Reed, M.B., Vincent, A.T., Tocheva, E.I., Veyrier, F.J., Nyongesa, S., Morneau, I., 2018. The Mycobacterial Cell Envelope: A Relict From the Past or the Result of Recent Evolution? Front. Microbiol. 9, 1–9. https://doi.org/10.3389/fmicb.2018.02341

Rosenberg, O.S., Dovala, D., Li, X., Connolly, L., Bendebury, A., Finer-Moore, J., Holton, J., Cheng, Y., Stroud, R.M., Cox, J.S., 2015. Substrates Control Multimerization and Activation of the Multi-Domain ATPase Motor of Type VII Secretion. Cell 161, 501–512. https://doi.org/10.1016/j.cell.2015.03.040

Sigmund, F., Massner, C., Erdmann, P., Stelzl, A., Rolbieski, H., Desai, M., Bricault, S., Wörner, T.P., Snijder, J., Geerlof, A., Fuchs, H., Hrabě de Angelis, M., Heck, A.J.R., Jasanoff, A., Ntziachristos, V., Plitzko, J., Westmeyer, G.G., 2018. Bacterial encapsulins as orthogonal compartments for mammalian cell engineering. Nat. Commun. 9, 1990. https://doi.org/10.1038/s41467-018-04227-3

Sigmund, F., Pettinger, S., Kube, M., Schneider, F., Schifferer, M., Schneider, S., Efremova, M. V., Pujol-Martí, J., Aichler, M., Walch, A., Misgeld, T., Dietz, H., Westmeyer, G.G., 2019. Iron-Sequestering Nanocompartments as Multiplexed Electron Microscopy Gene Reporters. ACS Nano 13, 8114–8123. https://doi.org/10.1021/acsnano.9b03140

Simeone, R., Bobard, A., Lippmann, J., Bitter, W., Majlessi, L., Brosch, R., Enninga, J., 2012. Phagosomal Rupture by *Mycobacterium tuberculosis* Results in Toxicity and Host Cell Death. PLoS Pathog. 8, e1002507. https://doi.org/10.1371/journal.ppat.1002507

Sutton, G., Sun, D., Fu, X., Kotecha, A., Hecksel, C.W., Clare, D.K., Zhang, P., Stuart, D.I., Boyce, M., 2020. Assembly intermediates of orthoreovirus captured in the cell. Nat. Commun. 11, 4445. https://doi.org/10.1038/s41467-020-18243-9

Tegunov, D., Cramer, P., 2019. Real-time cryo-electron microscopy data preprocessing with Warp. Nat. Methods 16, 1146–1152. https://doi.org/10.1038/s41592-019-0580-y

Tegunov, D., Xue, L., Dienemann, C., Cramer, P., Mahamid, J., 2021. Multi-particle cryo-EM refinement with M visualizes ribosome-antibiotic complex at 3.5 Å in cells. Nat. Methods 18, 186–193. https://doi.org/10.1038/s41592-020-01054-7

Turk, M., Baumeister, W., 2020. The promise and the challenges of cryo-electron tomography. FEBS Lett. 594, 3243–3261. https://doi.org/10.1002/1873-3468.13948

Turoňová, B., Hagen, W.J.H., Obr, M., Mosalaganti, S., Beugelink, J.W., Zimmerli, C.E., Kräusslich, H.-G., Beck, M., 2020. Benchmarking tomographic acquisition schemes for high-resolution structural biology. Nat. Commun. 11, 876. https://doi.org/10.1038/s41467-020-14535-2

van der Wel, N., Hava, D., Houben, D., Fluitsma, D., van Zon, M., Pierson, J., Brenner, M., Peters, P.J., 2007. *M. tuberculosis* and *M. leprae* Translocate from the Phagolysosome to the Cytosol in Myeloid Cells. Cell 129, 1287–1298. https://doi.org/10.1016/j.cell.2007.05.059

van Winden, V.J.C., Ummels, R., Piersma, S.R., Jiménez, C.R., Korotkov, K. V., Bitter, W., Houben, E.N.G., 2016. Mycosins Are Required for the Stabilization of the ESX-1 and ESX-5 Type VII Secretion Membrane Complexes. MBio 7, 1–11. https://doi.org/10.1128/mBio.01471-16

Wagner, T., Merino, F., Stabrin, M., Moriya, T., Antoni, C., Apelbaum, A., Hagel, P., Sitsel, O., Raisch, T., Prumbaum, D., Quentin, D., Roderer, D., Tacke, S., Siebolds, B., Schubert, E., Shaikh, T.R., Lill, P., Gatsogiannis, C., Raunser, S., 2019. SPHIRE-crYOLO is a fast and accurate fully automated particle picker for cryo-EM. Commun. Biol. 2, 218. https://doi.org/10.1038/s42003-019-0437-z

Wang, Z., Grange, M., Pospich, S., Wagner, T., Kho, A.L., Gautel, M., Raunser, S., 2021. Structure of the thin filament in native skeletal muscles reveals its interaction with nebulin and two distinct conformations of myosin. bioRxiv.

Wirth, S.E., Krywy, J. a., Aldridge, B.B., Fortune, S.M., Fernandez-Suarez, M., Gray, T. a., Derbyshire, K.M., 2012. Polar assembly and scaffolding proteins of the virulence-associated ESX-1 secretory apparatus in mycobacteria. Mol. Microbiol. 83, 654–664. https://doi.org/10.1111/j.1365-2958.2011.07958.x

Wolf, S.G., Mutsafi, Y., Dadosh, T., Ilani, T., Lansky, Z., Horowitz, B., Rubin, S., Elbaum, M., Fass, D., 2017. 3D visualization of mitochondrial solid-phase calcium stores in whole cells. Elife 6, 1–18. https://doi.org/10.7554/eLife.29929

Woodward, C.L., Mendonça, L.M., Jensen, G.J., 2015. Direct visualization of vaults within intact cells by electron cryo-tomography. Cell. Mol. Life Sci. 72, 3401–3409. https://doi.org/10.1007/s00018-015-1898-y

Xu, M., Singla, J., Tocheva, E.I., Chang, Y.-W., Stevens, R.C., Jensen, G.J., Alber, F., 2019. De Novo Structural Pattern Mining in Cellular Electron Cryotomograms. Structure 27, 679-691.e14. https://doi.org/10.1016/j.str.2019.01.005

Appendix

Impact

Summary (Dutch)

Acknowledgements

List of publications

About the author

Impact

The structure of proteins and other macromolecules has been studies for decades now at high resolution using techniques such as X-ray crystallography and nuclear magnetic resonance spectroscopy (NMR). This resulted into important insights into the relationship between structure and function. However, a limitation of these techniques is that protein structure is observed in isolation, rather than the complex environment of the cells, where it performs these functions in conjunction with other proteins. Understanding how protein structure affects functions is crucial to understand their role in the cell in health in disease. Processes in the human body, such as controlling cell division and the immune system may malfunction, resulting in pathologies such as cancer and auto-immune diseases. By better understanding these processes at a structural level, more avenues are created to cure or even prevent disease. Likewise, by understanding how the structure of proteins determines how infectious pathogens, such as Tuberculosis and COVID-19, spread and cause disease can create opportunities to design better vaccines and treatments. Proteins perform complex functions at a molecular level such as manipulating other small molecules, or act as molecular motors. In the long term, a thorough understanding of how protein structure controls the function of proteins may benefit the rational design of novel proteins for biotechnological applications.

Developments in cryo-electron microscopy combined with a relatively novel method to create ±200 nm thin slices of cells using a focused ion beam allow for a unique opportunity to study the variability of protein structure in relationship to its cellular environment. While these methods are still in an early stage, important novel scientific insights are already being obtained by its application. In this thesis project we applied and further developed these methods to study the structure of bacterial secretion systems during intracellular infection. We determined the structure of the bacterial type III secretion system of the pathogen *Yersinia enterocolitica* during intracellular infection in collaboration with scientist from other research groups, and shared these findings with the scientific community in a scientific journal. We combined observation of the structure of mycobacterial encapsulins in the cell with high-resolution structural data of isolated encapsulins to gain insight into the structural dynamics of mycobacterial encapsulin assembly and disassembly, for which a manuscript is in preparation.

We developed a method to distribute gold fiducials in cryo-FIB lamellae of cellular samples by using endocytosis. To disseminate this methodology among other scientist, the results were published in a scientific journal. For rapidly freezing cells on electron microscopy sample carriers, a novel technique that uses jets of liquid ethane to increase the cooling rate. M4i Nanoscopy and the company Cryosol (that originates from M4i Nanoscopy) are together developing a commercial instrument for jet-freezing mammalian cells. We also used our experience to write a literature review on the methodology and the scientific results obtained with them thus far, and the potential for the technique in the future, for which a manuscript for publication is in preparation. The skills and knowledge obtained on cellular cryo-electron tomography by all the scientists directly involved are invaluable for new research projects at the M4i Nanoscopy, and other research groups.

Summary (Dutch)

Titel: Cryo–elektronentomografie van FIB-lamellen voor het bepalen van de structuur van bacteriële secretiesystemen

Eiwitten en andere macromoleculen zijn essentieel voor het bestaan van leven. Door hun structurele eigenschappen kunnen ze een grote variatie aan cellulaire functies vervullen. De structuur van eiwitten wordt al decennialang onderzocht met behulp van technieken zoals röntgenkristallografie en kernspinresonantie. Dit heeft belangrijke inzichten verschaft over hoe eiwitten hun biologische functies kunnen uitoefenen. Een beperking van deze technieken is dat eiwitten eerst moeten worden geïsoleerd en opgezuiverd. Hierdoor verliezen deze de context van de cel of organisme waarin ze normaal functioneren en kunnen interacties met andere macromoleculen die van invloed zijn op de structuur en functie verloren gaan. Door de structuur van eiwitten in hun biologische context bepalen blijven deze behouden, wat tot nieuwe inzichten kan leiden in het verband tussen eiwitstructuur en de cellulaire functies. De structuur bepalen van macromoleculen in de cel is mogelijk geworden door ontwikkelingen in elektronenmicroscopie.

Door de ontwikkelingen van nauwkeurigere transmissie elektronenmicroscopen is het nu mogelijk om de structuur van eiwitten te bepalen met een resolutie van enkele tienden van een nanometer. Dit is mogelijk door honderden tot honderdduizenden kopieën van hetzelfde eiwit (of ander macromolecuul) iteratief uit te lijnen en te middelen. De monsters worden bekeken in de elektronenmicroscoop onder cryogene condities (>-150 °C) om deze te beschermen tegen het vacuüm. Door cryo-elektronenmicroscopie opnamen te maken van het monster onder verschillende hoeken kan een driedimensionaal tomografisch beeld worden gevormd, waardoor eiwitcomplexen ook in cellen, kleine organismen en weefsels kunnen worden waargenomen. Een beperking is echter dat dit alleen goed mogelijk is voor dunne monsters met een dikte tot ongeveer 300 nanometer, terwijl de meeste monsters dikker zijn. Met behulp van een relatief nieuwe techniek kan met een gefocusseerde ionen bundel (FIB) onder cryogene condities al het materiaal onder en boven een deel van het biologische materiaal worden verwijderd, waardoor er een ±200 nanometer dunne plak overblijft genaamd een lamel. Deze lamellen zijn geschikt om de structuur van eiwitten te bepalen in hun natuurlijke omgeving.

Het doel van dit promotietraject is om met behulp van cryo-elektronentomografie (CET) van FIB-lamellen de structuur te bepalen van bacteriële secretiesystem tijdens de infectie van gastheercellen. Secretiesystemen zijn grote eiwitcomplexen die virulentie factoren door de bacteriële membranen heen in een gastheer kunnen transporteren. Dit maakt deze complexen essentieel voor de infectiviteit van een groot aantal ziekteverwerkers. Inzichten in de structuur van deze complexen dragen bij aan de ontwikkeling van betere vaccins en antibacteriële middelen. Het secretiesysteem waar we in het bijzonder in zijn geïnteresseerd is het type VII secretiesysteem ESX-1, wat essentieel is voor de infectiviteit van de tuberculose bacterie.

Wereldwijd overlijden er jaarlijks 1,4 miljoen mensen aan de gevolgen van tuberculose.

Omdat CET van FIB-lamellen een relatief nieuwe techniek is hebben we eerst tijd geïnvesteerd om deze te optimaliseren voor onze microscopen en onderzoeksvragen. Op basis van deze ervaringen geven we een literatuuroverzicht van recent structureel biologisch onderzoek dat is uitgevoerd met deze technieken, welke technische ontwikkelingen dit mogelijk hebben gemaakt, en een vooruitblik op wat voor onderzoek in de komende jaren mogelijk kan worden met verdere technische verbeteringen (Hoofdstuk 2).

Om de EM opnamen die zijn gemaakt onder verschillende hoeken te reconstrueren tot een 3-dimensionaal volume is het noodzakelijk om deze nauwkeurig uit te lijnen. De meest nauwkeurige methode hiervoor maakt gebruikt van toegevoegde ankerpunten, die normaliter niet aanwezig zijn in cellen. Om cellulaire EM opnamen toch met deze ankerpunten uit te kunnen lijnen hebben we een methode ontwikkeld om goudbolletjes van 10 nanometer in cellen te krijgen met behulp van endocytose. Deze intracellulaire goudbolletjes kunnen gebruikt worden als ankerpunten, en we laten zien dat dit nauwkeuriger is voor cryo-tomografische data die is opgenomen van FIB-lamellen in vergelijking met de gebruikelijke methode zonder deze ankerpunten (Hoofdstuk 3). De resultaten zijn gepubliceerd in het wetenschappelijke vakblad de “Journal of Structural Biology”.

Om te valideren of de geïmplementeerde CET-workflow te gebruiken is om de structuur te bepalen van bacteriële secretiesystem tijdens intracellulaire infectie, hebben we deze eerst toegepast op het type III secretiesysteem (T3SS) van de ziekteverwekker *Yersinia enterocolitica* (Hoofdstuk 4). Hiervoor hebben we meer dan 150 reeksen van CET-data opgenomen op FIB-lamellen van immuun cellen geïnfecteerd met *Y. enterocolitica*. Met deze data konden we de structuur bepalen van het T3SS door 202 kopieën iteratief uit te lijnen en te middelen in een proces genaamd “subtomogram averaging”. Hierdoor konden we structurele informatie verkrijgen over de cytosolische componenten van het complex voor deze bacterie, die in eerdere studies niet zijn opgehelderd. Verder laten we zien dat de naald van het T3SS, welk wordt gebruikt om virulentie factoren door membranen van de gastheer heen te injecteren, een minimale lengte nodig heeft om in contact te komen met de deze membranen. Deze bevindingen dragen bij aan ons begrip hoe het T3SS haar functie kan uitoefenen in gastheercellen, en zijn gepubliceerd in het wetenschappelijke vakblad de “Journal of Structural Biology”.

Vervolgens hebben we ons gericht op het type VII secretiesysteem ESX-1 in mycobacteriën. We hebben meer dan 200 reeksen van CET-data opgenomen op FIB-lamellen van immuun cellen geïnfecteerd met *Mycobacterium marinum*, een model voor de tuberculose bacterie. De kwaliteit van de data was vergelijkbaar of beter dan de vorige dataset, maar desondanks was het niet mogelijk om ESX-1 visueel te identificeren in de tomogrammen. Mogelijke oorzaken hiervoor worden besproken in de algemene discussie (Hoofdstuk 6).

Een van de andere voordelen van eiwitcomplexen bestuderen in cellen, weefsels of kleine organismen is dat naast het eiwitcomplex waarin primair naar wordt gezocht ook andere complexen aanwezig zijn. Een overzicht van de macromoleculaire complexen en membraan structuren die we hebben waargenomen in deze dataset wordt gegeven in Hoofdstuk 6. Eén van complexen die we hebben gevonden is zijn bacteriële opslag compartimenten genaamd encapsulines. Met “subtomogram averaging” kon de structuur van het encapsuline complex bepaald worden met een resolutie van 3 nm in de bacteriën (Hoofdstuk 5). Daarnaast zagen wij een grote structurele diversiteit in de individuele complexen, waaronder encapsulines geladen met verschillende componenten, encapsulines in verschillende stadia van assemblage en flexibele structuren op de buitenkant van de encapsulines. Om encapsulines met een hogere resolutie te bestuderen hebben we encapsulines van *M. tuberculosis* geëxpresseerd in de bacterie *Escherichia coli* en geïsoleerd, en de structuur bepaald met cryo-elektronen microscopie en een “single particle” analyse. Hiermee kon de structuur worden bepaald van volledig geassembleerde encapsulines, en drie structuren van encapsulines in verschillende stadia van opbouw en/of afbraak. Deze bevindingen geven inzicht in de op- en afbouw van encapsulines in de cel.

Tesamen draagt dit promotieonderzoek bij aan biologische inzichten in het T3SS, encapsulines, en de technische ontwikkeling van CET in cellen. Door ontwikkelingen die momenteel plaatsvinden waardoor er sneller monsters kunnen worden geprepareerd, data kan worden opgenomen en worden verwerkt is het aannemelijk dat in de komende jaren steeds van steeds meer macromoleculen structuren kunnen worden bepaald in de context van cellen of weefsels.

Acknowledgements

From struggling with ill-behaved microscopes to obtaining in situ structures, this PhD has been quite the journey. It gave me the opportunity to be a (small) part of the rapid developments in cellular cryo-electron tomography in the last years, and prepared me to keep being a part of it, for which I am grateful. This thesis would not have been possible without the help and support from many people, for which I would like to express my gratitude.

Firstly, I would like to thank **Carmen**, **Raimond** and **Peter** for the opportunity to get involved in cryo-electron microscopy, guiding and mentoring me through this process and preparing me for the next step in an academic career.

I thank **Hang** for her efforts to make my manuscripts more readable and organised and **Anita** for her help with administrative matters, in particular in the final stages. I thank my students **Erik** and **Matthias** that I had the pleasure to supervise. I hope they learned as much from it as I did.

I thank **Andreas** and **Mischa** for working together on the structure of the type III secretion system. I hope we may run into each other in the future. I thank the members of the **assessment committee**, Prof. dr. C.P.M.Reutelingsperger, dr. M. Bárcena, Prof. dr. L. Moroni and Prof. dr. C. Sachse, for taking the time to read and evaluate my thesis.

I thank my paranymphs **Paul** and **Navya** and my third (honorary) paranymph **Abril** for their help with organising the thesis defence and reception, but more importantly for being overall great colleagues. Finally, I would like to thank all the other great colleagues at **M4i Nanoscopy** and **M4i CORE lab** that I had the pleasure to work with over the years for working and publishing together, scientific discussions, technical support, critical feedback but also fun besides work: **Chris**, **Yue**, **Ye**, **Kèvin**, **Nick**, **Hans**, **Helma**, **Willine**, **Marie-Hélène**, **Rodrigo**, **Audrey**, **Nino**, **Kristof**, **Axel**, **Delei**, **Giancarlo**, **Hirotoshi**, **Ralph, Frank**, **René**, **Giulia** and everyone else.

I thank **my family** for their continuous support and interest in my projects: **Edith**, **Laurens**, **Stijn**, **Roeland**, **Babette**, **Franne**, **Noor** and **Philip**. Most importantly, I would like to thank **Nynke**, my greatest discovery during my time in Maastricht. Thank you for being with me, making my life better in every aspect. I am sure everything will get easier, once our baby is born ;).

List of publications

Berger, C., Ravelli, R.B.G., López-Iglesias, C., Peters, P.J., 2021. **Endocytosed nanogold fiducials for improved *in-situ* cryo–electron tomography tilt-series alignment.** J. Struct. Biol. 213, 107698. https://doi.org/10.1016/j.jsb.2021.107698

Berger, C., Ravelli, R.B.G., López-Iglesias, C., Kudryashev, M., Diepold, A., Peters, P.J., 2021. **Structure of the *Yersinia* injectisome in intracellular host cell phagosomes revealed by cryo FIB electron tomography.** J. Struct. Biol. 213, 107701. https://doi.org/10.1016/j.jsb.2021.107701

Berger, C., Premaraj N., Ravelli, R.B.G., Knoops, K., López-Iglesias, C., Peters, P.J., **Cryo–electron tomography on FIB lamellae transforms structural cell biology** (*submitted*)

Berger, C.*, Lewis, C.*, Gao, Y., Knoops, K., López-Iglesias, C., Peters, P.J., Ravelli, R.B.G. ***In situ* and *in vitro* cryo-EM reveal structures of mycobacterial encapsulin assembly intermediates** (*submitted*)

Berger, C.*, Dumoux, M.*, Glen, T.*, Yee, N.B.-y., Mitchels, J.M., Patáková, Z., Naismith, J.H., Grange, M., 2022. **Plasma FIB milling for the determination of structures.** bioRxiv. https://doi.org/doi.org/10.1101/2022.08.01.502333 (*under review*)

Perdigão, L.M.A., **Berger, C.**, Yee, N.B.-y., Darrow, M.C., Basham, M. **RedLionfish – Fast Richardson-Lucy Deconvolution package for Efficient PSF Suppression in Volumetric Data** (*manuscript in preparation*)

*shared first author

About the author

Casper Berger was born on February 8th, 1987 in Utrecht, The Netherlands and graduated high school at the Werkplaats Kindergemeenschap in Bilthoven in 2005. In 2011 he obtained his bachelor degree in biomedical sciences at the University of Utrecht with his dissertation titled “Exosome biogenesis and its role in cardiac injury”. In 2014 he obtained his master degree in Infection and Immunity at the University of Utrecht with research projects titled “Tetraspanins-GFP fusion proteins as markers for the detection of individual extracellular vesicles with high-resolution flow cytometry and fluorescence microscopy” and “Recognition of the flagellar cap protein FliD by the innate immune system and chicken IgY antibodies”.

In 2015, Casper started his PhD at the Nanoscopy group of the MultiModal Molecular Imaging (M4i) institute of the University of Maastricht under the supervision of Prof. Peter J. Peters, Prof. Raimond B. G. Ravelli and dr. Carmen López-Iglesias. The research at this position, as described in this thesis, focused on using cryo-electron tomography to structurally study bacterial secretion system during intracellular infection of mammalian cells. In 2021 he moved to Oxfordshire, England to join the structural biology group of the newly founded Rosalind Franklin Institute as a postdoctoral researcher in cellular cryo-electron tomography.